UDK 66:54(05) CODEN HMIDA 8 ISSN 0367–598X

5

Hemijska industrija

Vol. 75

Časopis Saveza hemijskih inženjera Srbije

Chemical Industry

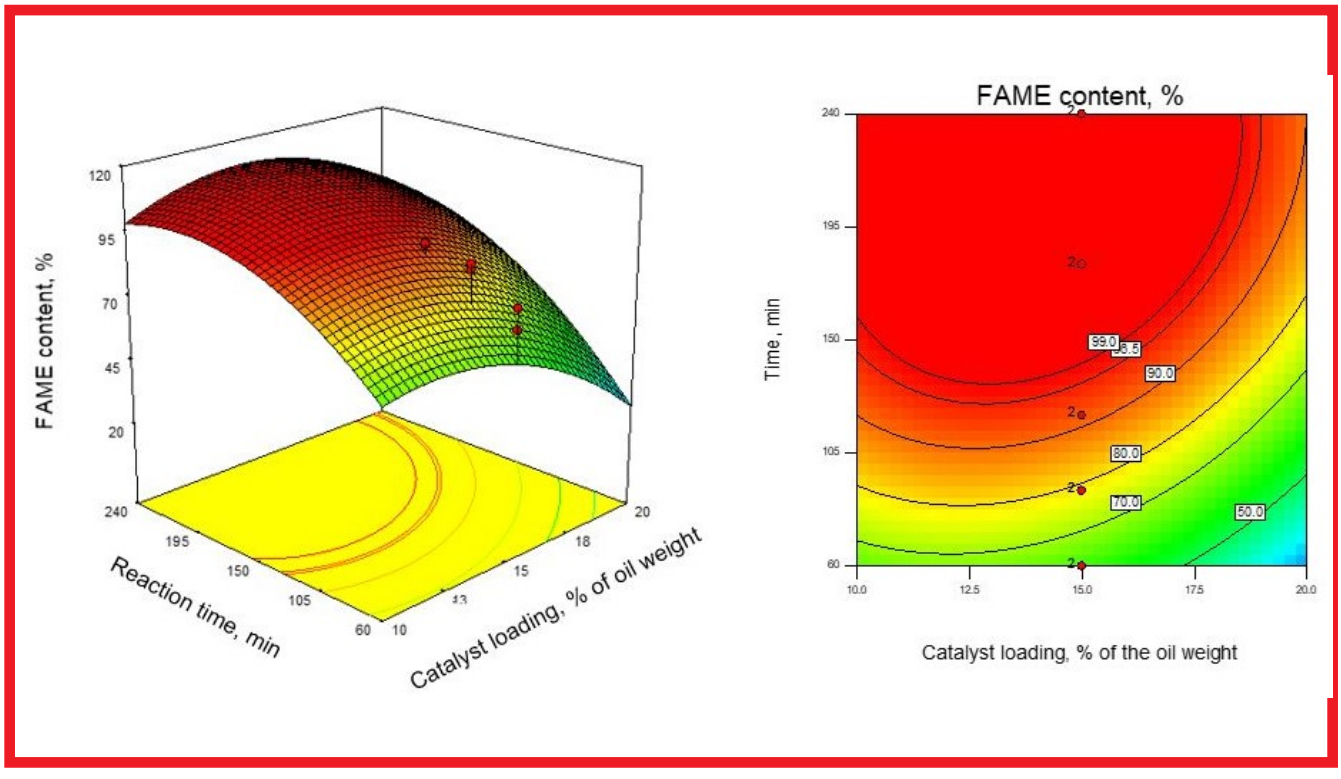

BEOGRAD, SEPTEMBER-OCTOBER 2021. HMIDA 8, 75 (5) 257-327 (2021)

Aktivnosti Saveza hemijskih inženjera Srbije pomažu:

**MINISTARSTVO PROSVETE,
NAUKE I TEHNOLOŠKOG RAZVOJA
REPUBLIKE SRBIJE**

Tehnološko-metalurški fakultet
Univerziteta u Beogradu, Beograd

Institut za tehnologiju nuklearnih i
drugih mineralnih sirovina, Beograd

Hemijski fakutet Univerziteta u
Beogradu, Beograd

Prirodno-matematički fakultet
Univerziteta u Novom Sadu, Novi Sad

Institut za opštu i fizičku hemiju,
Beograd

Tehnološki fakultet
Univerziteta u Novom Sadu, Novi Sad

NU Institut za hemiju, tehnologiju i metalurgiju
Univerziteta u Beogradu, Beograd

Institut IMS, Beograd

Tehnološki fakultet
Univerziteta u Nišu, Leskovac

Fakultet tehničkih nauka,
Kosovska Mitrovica

Chemical Industry
Химическая промышленность

Hemijska industrija

Časopis Saveza hemijskih inženjera Srbije
Journal of the Association of Chemical Engineers of Serbia
Журнал Союза химических инженеров Сербии

VOL. 75 **Beograd, septembar-oktobar 2021.** **Broj 5**

Izdavač
Savez hemijskih inženjera Srbije
Beograd, Kneza Miloša 9/I

Glavni urednik
Bojana Obradović

Zamenica glavnog i odgovornog urednika
Emila Živković

Pomoćnik glavnog i odgovornog urednika
Ivana Drvenica

Urednici
Enis Džunuzović, Ivana Banković-Ilić, Maja Obradović, Dušan Mijin, Marija Nikolić, Tatjana Volkov-Husović, Đorđe Veljović,

Članovi uredništva
Nikolaj Ostrovski, Milorad Cakić, Željko Čupić, Miodrag Lazić, Slobodan Petrović, Milovan Purenović, Aleksandar Spasić, Dragoslav Stoiljković, Radmila Šećerov-Sokolović, Slobodan Šerbanović, Nikola Nikačević, Svetomir Milojević

Članovi uredništva iz inostranstva
Dragomir Bukur (SAD), Jiri Hanika (Češka Republika), Valerij Meshalkin (Rusija), Ljubiša Radović (SAD), Constantinos Vayenas (Grčka)

Likovno-grafičko rešenje naslovne strane
Milan Jovanović

Redakcija
11000 Beograd, Kneza Miloša 9/I
Tel/fax: 011/3240-018
E-pošta: shi@ache.org.rs
www.ache.org.rs

Izlazi dvomesečno, rukopisi se ne vraćaju

Za izdavača: Ivana T. Drvenica

Sekretar redakcije: Slavica Desnica

Izdavanje časopisa pomaže
Republika Srbija, Ministarstvo prosvete, nauke i tehnološkog razvoja

Uplata pretplate i oglasnog prostora vrši se na tekući račun Saveza hemijskih inženjera Srbije, Beograd, broj 205-2172-71, Komercijalna banka a.d., Beograd

Menadžer časopisa i Kompjuterska priprema
Aleksandar Dekanski

Štampa
Razvojno-istraživački centar grafičkog inženjerstva, Tehnološko-metalurški fakultet, Univerzitet u Beogradu, Karnegijeva 4, 11000 Beograd

Indeksiranje
Radovi koji se publikuju u časopisu *Hemijska Industrija* ideksiraju se preko *Thompson Reuters Scietific®* servisa *Science Citation Index - Expanded™* i *Journal Citation Report (JCR)*

SADRŽAJ/CONTENTS

Modeling the biodiesel production using the wheat straw ash as a catalyst

Ana Veličković[1], Jelena Avramović[1], Milan Kostić[2], Jugoslav B. Krstić[3], Olivera Stamenković[2] i Vlada B. Veljković[2,4,]

[1]*University in Priština - Kosovska Mitrovica, Faculty of Technical Sciences, Knjaza Miloša 7, 38220, Serbia*
[2]*Faculty of Technology, University of Niš, Bulevar oslobođenja, 16000 Leskovac, Serbia*
[3]*University of Belgrade – Institute of Chemistry, Technology and Metallurgy, Belgrade, Serbia*
[4]*The Serbian Academy of Sciences and Arts, Knez Mihailova 35, 11000 Belgrade, Serbia*

Abstract

Wheat straw ash (WSA) was investigated as a new catalyst in biodiesel production from sunflower oil. The catalyst was characterized by temperature-programmed decomposition, X-ray powder diffraction, Hg porosimetry, N_2 physisorption, and scanning electron microscopy - energy dispersive X-ray spectroscopy methods. The methanolysis reaction was tested in the temperature range of 55–65 °C, the catalyst loading range 10–20 % of the oil weight, and the methanol-to-oil molar ratio range 18 : 1–24 : 1. The reaction conditions of the sunflower oil methanolysis over WSA were optimized by using the response surface methodology in combination with the historical experimental design. The optimum process conditions ensuring the highest fatty acid methyl esters (FAME) content of 98.6 % were the reaction temperature of 60.3 °C, the catalyst loading of 11.6 % (based on the oil weight), the methanol-to-oil molar ratio of 18.3 :1, and the reaction time of 124 min. The values of the statistical criteria, such as coefficients of determination (R^2 = 0.811, R^2_{pred} = 0.789, R^2_{adj} = 0.761) and the mean relative percent deviation (MRPD) value of 10.6 % (66 data) implied the acceptability and precision of the developed model. The FAME content after 4 h of reaction under the optimal conditions decreased to 37, 12, and 3 %, after the first, second, and third reuse, respectively.

keywords: agricultural residues; fatty acid methyl esters; catalyst characterization; model; optimization.

Available on-line at the Journal web address: http://www.ache.org.rs/HI/

ORIGINAL SCIENTIFIC PAPER

UDC: 665.75:658.52:005.585:631.831

Hem. Ind. **75 (5)** 257-276 (2021)

1. INTRODUCTION

Given the growing global need for energy and the scarcity of fossil fuel reserves, as well as the severe climate change, the question is imposed of future energy sources that will be able to meet the need of the economy and society. Therefore, the emphasis must be put on renewable and sustainable energy sources, such as biomass, solar, wind, and geothermal energy. Biomass including waste agricultural residues is significant as a source for energy production by combustion or for biofuel production *via* various chemical, biological, or thermochemical routes. Recently, it has been estimated that about 3–14 % of the total energy supply in the world could be generated from agricultural residues [1].

Biodiesel, a biomass-based fuel, is commonly produced by chemical conversion of vegetable oils, and widely used as an adequate replacement for diesel fuel. The advantages of biodiesel, compared to petroleum-based diesel, are renewability, sustainability, and reduced emission of CO_2, SO_2, and hydrocarbons [2].

Heterogeneous catalysts (metal oxides, mixed oxides, supported alkali metals, zeolites, hydrotalcites, etc.) have been investigated as more favorable options than homogeneous ones for they are less corrosive, more environmentally friendly, easily separable, and potentially reusable [2-4]. To enhance the overall sustainability of the biodiesel

Corresponding author: Vlada B. Veljković, Faculty of Technology, University of Niš, Serbia
E-mail: veljkovicvb@yahoo.com
Paper received: 26 May 2021; Paper accepted: 17 October 2021; Paper published: 1 November 2021.
https://doi.org/10.2298/HEMIND210526028V

CC BY NC ND

production process and to reduce the production costs, the attention of researchers has been recently directed towards low-cost ashes as heterogeneous catalysts. These materials are derived by combusting high volume resources, such as agricultural biomass including plant residues from the crop, fruit, and viticulture production [5]. The advantages of waste biomass are wide availability, low price, sustainability, and renewability. Besides providing a highly active catalyst for biodiesel production, this approach is both cost-effective and eco-friendly.

In recent years, many researchers have combusted different biomass materials, specific for each climate region, to get ashes, which have been successfully employed as efficient catalysts in biodiesel production. A review of the ash-based catalysts used in biodiesel production is given in Table 1.

Table 1. A review of agricultural waste-based ashes catalysts used in biodiesel production

Source of catalyst	Active species	Oil source	Methanol/oil molar ratio	Catalyst loading, %	*t* / °C	Ester yield (content), % / min	Statistical method[d]	Ref.
Musa paradisiacal peels	K	*Azadirachta indica*	16.74:1	0.65	65	99.2/57	3^5 CCD	[6]
Musa paradisiacal peels	K	*Thevetia peruviana*	6.85:1	3	60	95/90	Box–Behnken + ANN	[7]
Banana peels	-	Palm kernel	14.63:1	4	65	99.5/65	3^5 CCD	[8]
	K	*Bauhinia monandra*	6.86:1	2.75	65	98.5/69	2^3CCD	[9]
Musa balbisiana Colla peel	K	Waste cooking (WCO)	6:1	2	60	100/180	-	[10]
Tucuma peels (Astrocaryum aculeatum Meyer*)*	K	Soybean oil	15:1	1	80	97.3/240	-	[22]
Musa acuminata Colla 'Red' banana peduncle	K, Si, Ca, Mg	*Ceiba pentandra* (CPO)	11.5:1	2.68	65	98.73/106	CCD	[11]
Banana (*Musa spp.* 'Pisang Awak') peduncle	K	*Ceiba pentandra* (CPO)	9.2:1	1.978	60	98.69/60	CCD	[12]
Musa balbisiana stem	K, Na	*Thevetia peruviana*	10:1	20	32	96/180	-	[13]
Musa balbisiana stem	K	*Jatropha curcas*	9:1	5	275	98/60	-	[14]
Musa balbisiana underground stem	-	*Mesua ferrea*	9:1	5	275	95/60	-	[15]
Cocoa pod husk	K	*Azadirachta indica*	16.74:1	0.65	65	99/57	CCD	[16]
Cocoa pod husk	-	Palm kernel	14.63:1	4	65	99.3/65	3^5 CCD	[8]
Coconut husk	K	Jatropha	12:1	7	45	(99.86)/45	-	[17]
Rice husk	Li, Na, K*	Used cooking	9:1	3	65	(98.2)/60	-	[18]
Walnut shell	K, Ca	Sunflower	12:1	5	60	(>98)/10	-	[19]
Palm kernel shell biochar	Ca	Sunflower	9:1	3	65	(99)/240	3^3 FFD	[20]
Mangifera indica peel	K	Soybean oil	6:1	6	28	98/360	-	[21]
Birch bark	-	Palm	12:1	3	60	(88.06)/180	-	[23]
Moringa leaves ash	-	Soybean oil	6:1	6	65	86.7/120	-	[24]
Pineapple (Ananás comosus) leaves ash	K, Ca	Soybean oil	40:1	4	60	>98/30	-	[25]
Brassica nigra plant	K	Soybean	12:1	7	65	98.79/25	-	[26]
					32	98.87/75	-	
		Jatropha			65	98.26/30	-	
		Thevetia peruvianal			65	97.78/25	-	
Corn cobs	-	Corn germs	9.4:1	19.8	60	(98.1)/31	3^3 FFD	[27]
Arecanut husk ash[a]	-	WCO	3:1-15:1	1-5	65	96.5/120 99.98/150	-	[28]
Citrus sinensis peel[b]	-	WCO	6:1	6	65	98/180	-	[29]
Wheat bran (ash with CaO)[c]	-	WCO	33:1	11.66	54.6	93.6/114.21	3^5 CCD	[30]
Wheat straw	K, Si	Sunflower	18.3:1	11.6	60.3	(98.6)/124	Historical data design	This work

**Supported on rice husk; [a]Ash modified with $LiNO_3$; [b]Ash coated Fe_3O_4. nanoparticles; [c]Ash modified with CaO from water scale from a distillation unit; [d]ANN – artificial neural network, CCD – central composite design, FFD – full factorial design.*

For instance, ashes of peels from different types of bananas, were used as a catalyst for the transformation of *Azadirachta indica* [6], *Thevetia peruviana* [7], palm kernel [8], *Bauhinia monandra* [9], and waste cooking [10] oils to biodiesel. A high yield of methyl esters (> 95 %) was also obtained using ashes from other parts of banana, such as

peduncles [11,12] and stems [13-15]. Moreover, methanolysis of various oils was successfully carried out in the presence of husk ashes obtained from different biomass wastes, such as cocoa pod [8,16], coconut [17], and rice [18], walnut kernel [19] and palm kernel [20] shells, mango [21], and tucuma [22] peels ashes. Furthermore, ashes from bark [23], leaves [24,25], whole plants [26], and cobs [27] were used to catalyze biodiesel production. Some ashes were improved before the use as catalysts. Areca nut husk ash was impregnated with $LiNO_3$ to improve its alkalinity [28] while sweet orange peel ash was coated onto Fe_3O_4 nanoparticles to enhance its dispersion and stability and to enable its recovery from the reaction mixture by an external magnet [29].

Wheat straw has great potentials for many uses, such as the increase of soil fertility or the production of matting, livestock food, ethanol fuel, and heat, with the possibility of causing conflict among the potential users. Fortunately, there is enough wheat straw to be divided to fulfill all the demands, instead of being burned at fields. The yield of wheat straw during harvest is approximately 4-6 t ha^{-1} [31], depending on cutting height [32]. From a field producing 1 t of grain, 1 t of wheat straw can be harvested [33]. The annual collectible potential of wheat straw in Serbia for energy generation, calculated according to a conservative utilization rate of 30 %, is about 750,000 t [33].

In Serbia, wheat straw is the most used waste biomass for energy production by direct combustion, with average energy and ash contents of 14.4 MJ kg^{-1} and 5 %, respectively [33]. The open question related to this wheat straw utilization is what to do with the produced ash. From both the environmental and economic point of view, it should be safely treated and preferably reused in suitable production processes. The successful utilization of wheat straw ash (WSA) has been proven as a low-cost raw material in self-compacting pastes [34], a pozzolanic material in cement-based composites [35-39] and silicate glass-ceramics [40], a silica source [41,42], a filler in an alkali-activated geopolymer [43], a catalyst in char hydrogasification [44], and an adsorbent for hazardous substances removal [45-47].

This paper reports on the use of WSA as a catalyst in the production of biodiesel from sunflower oil. For a better understanding of its catalytic activity, WSA was first characterized using various techniques. Then, the reaction conditions of the sunflower oil methanolysis over WSA, like the reaction temperature, methanol-to-oil molar ratio, catalyst loading, and reaction time, were optimized using the response surface methodology (RSM) in combination with a historical experimental design. So far, there is a report of using wheat bran ashes modified with CaO obtained from water scale from a distillation unit as a catalyst [30], but according to the best knowledge of the authors, WSA has not been applied yet as a catalyst in biodiesel production. Considering the availability of wheat straw, the use of WSA as a heterogeneous catalyst could be economical.

2. MATERIALS AND METHODS

2. 1. Materials

Waste wheat straw was collected from a local farm. Edible sunflower oil (Dijamant, Zrenjanin, Serbia) was purchased in a local shopping store. The density and viscosity of the oil at 20 °C are 918.4 kg m^{-3} and 77.1 mPa·s, respectively. The acid, saponification, and iodine values of the oil, determined according to the AOCS official methods, were 0.29 mg KOH/g, 190 mg KOH/g, and 139 g I_2/100 g, respectively [48]. The oil consisted of the following fatty acids: palmitic acid (7.3 %), stearic acid (4 %), oleic acid (26 %), and linoleic acid (62.2 %) [49].

Certified methanol of 99.5 % purity was from Zorka Pharma (Šabac, Serbia). Methanol, 2-propanol, and *n*-hexane, all HPLC grade, were obtained from LAB-SCAN (Dublin, Ireland).

2. 2. Catalyst preparation

Wheat straw was completely combusted in a shallow metal tray at open air. Cold ash, called fresh WSA (fWSA) was collected, crushed using a porcelain mortar and pestle, sieved through a 1 mm sieve, and placed in a glass bottle, which was then stored in a desiccator. The WSA stored for 40 days, called the aged WSA (aWSA), did not show any activity in the methanolysis reaction of sunflower oil even after thermal activation at 150 °C. The fWSA catalyst was separated from the reaction mixture after completing the reaction by decanting, washed twice with 20 ml of methanol and then with 20 ml of *n*-hexane, dried in an oven at 120 °C for 15 min, and then cooled down in a desiccator. The separated

CC BY NC ND

catalyst eventually used in the subsequent reactions is called spent WSA (sWSA after the first use; sWSA1, sWSA2, and sWSA3 after the first, second, and third reuse, respectively).

2. 3. Catalyst characterization

The X-ray powder diffraction measurements were performed by a Rigaku Smartlab diffractometer (Rigaku, Japan) equipped with a D/teX Ultra 250 strip detector using $CuK_{\alpha1,2}$ (U = 40 kV and I = 30 mA) with low-background single-crystal silicon sample holders. The measurement was conducted in the 2θ = 10-70° domain, step-length of 0.01° and the rate of 5° / min.

Characterization of the fWSA, aWSA, sWSA, and sWSA3 samples by temperature-programmed decomposition (TPDe) was performed in the temperature range 50-800 °C with 60 min dwell time at the maximum temperature and the helium flow (20 cm^3 min^{-1}), using a TPDRO 1100 device (Thermo Scientific, Italy). In addition to the thermal conductivity detector (TCD), the device was also equipped with a ThermoStar GSD320 mass detector (Pfeiffer Vacuum, Germany). Prior to the measurement, each sample was dried in an oven at 110 °C for 24 h, transferred to a quartz tubular reactor at 40 °C, where it was held in the helium stream (20 cm^3 min^{-1}) for 60 min to eliminate possible adsorbed H_2O. Thereafter, CO_2 was adsorbed on the sample from a gas mixture of 16.2 % CO_2/He at the temperature of 40 °C and a flow rate of 20 cm^3 min^{-1} for 60 min. Finally, after cleaning the system and reactor lines of residual CO_2 with pure helium (20 cm^3 min^{-1} for 60 min), the sample was heated in a helium stream as described.

To determine morphology characteristics and chemical composition of fWSA, aWSA, sWSA, and sWSA3, they were analyzed by a scanning electron microscope (SEM) JEOL JSM-6610LV (Jeol, Japan) equipped with a secondary electron (SE) detector and energy-dispersive spectrometer (EDS) (Oxford Instruments, UK). Before the measurement, the samples were prepared by deposition of thin gold vapor layer on the catalyst surface employing the cool sputter coater LEICA SCD005 (Leica Microsystems, Germany).

Textural properties of fWSA and aWSA samples were determined by N_2 physisorption at -196 °C and mercury porosimetry. The adsorption-desorption isotherms were obtained by N_2 physisorption measurements at -196 °C by using a Sorptomatic 1990 device (Thermo Finnigan, Italy). The sample preparation procedure included drying in an oven for 4 h, transfer of the samples into a measuring burette and drying in a vacuum in regime 4 h at 110 °C and 18 h at 250 °C. The specific surface areas (SSA_{BET}) of the samples were calculated from the linear part of the adsorption isotherm by applying the Brunauer-Emmett-Teller (BET) equation [50]. The Dubinin-Radushkevich method [51] was used to determine the micropore volume (V_{mic}) while the mesopore volume (V_{mes}) was estimated by the Barrett, Joyner, and Halenda (BJH) method [52] from the desorption branch using the Lecloux standard isotherm [53].

Before the mercury porosimetry measurement, a sample was dried in an oven at 110 °C for 24 h, cooled in a desiccator and then placed in a sample holder and vacuumed for 2 h at room temperature. The bulk density was determined by a Macropore Unit 120 (Fisons Instruments, Italy), and after that, in the pressure range of 0.1-200 MPa Hg, the mercury porosimetry was conducted in a high-pressure unit PASCAL 440 (Thermo Fisher, Italy). In a high-pressure unit, for each sample, two consecutive intrusion-extrusion measurements (Run 1 and Run 2) were performed to determine the contribution of the interparticle and intraparticle space (*i.e.*, voids and pores, respectively) of the material porosity. A SOLID Software System PC interface was used for automatic data acquisition and all textural parameter calculations.

2. 4. Methanolysis reaction

The batch methanolysis reaction was carried out in a three-neck round-bottomed flask (250 cm^3) equipped with an upright reflux condenser and a magnetic stirrer. The reaction flask was placed in a water bath and kept at the desired temperature. Measured amounts of the fWSA catalyst and methanol were added to the reaction flask and maintained at the desired temperature for 15 min. The predetermined quantity of sunflower oil was heated at the same desired temperature and then poured into the reaction flask. As soon as the sunflower oil was added, agitation (900 rpm) and time measuring started. During the reaction, samples (1 cm^3) of the reaction mixture were withdrawn (at specified time intervals), poured into Eppendorf tubes, and immediately placed in ice-cold water to terminate the reaction. The

samples were then centrifuged (3500 rpm for 15 min). The fatty acid methyl esters (FAME)-oil layer was separated, dissolved in a solution of a mixture of 2-propanol and *n*-hexane (5/4 v/v) in a ratio 1/200, filtered through a Millipore filter (0.45 μm), and analyzed by the High Performance Liquid Chromatography (HPLC) method described elsewhere [54]**.** The methanolysis reaction was tested at the temperatures of 55, 60, and 65 °C, the catalyst loading of 10, 15 and 20 % of the oil weight and the methanol-to-oil molar ratio 18:1, 21:1, and 24:1. Kostić *et al.* [20] observed that an increase of the reaction temperatures from 45 to 65 °C accelerated the reaction significantly and shortened its duration from 7 h to 4 h. In a preliminary experiment conducted at 60 °C, using the catalyst amount of 10 % (based on the oil weight) and the methanol-to-oil molar ratio of 18:1, the reaction was completed after about 4 h. Therefore, the temperature of 55 °C was selected as the lower limit. The temperature of 65 °C was taken as the maximally possible upper value as the boiling point of methanol is 64.7 °C. In addition, the preliminary experiments showed that a larger quantity of methanol was required to distribute very voluminous WSA uniformly in the reaction mixture. Consequently, higher methanol-to-oil molar ratios were employed.

Leaching of catalytically active species was examined using the same procedure carried out under the optimal reaction conditions. The appropriate amounts of methanol and fWSA were stirred magnetically for 124 min under the optimized reaction conditions following the above-described procedure. After being separated from the catalyst, methanol was used in the reaction with sunflower oil without the presence of the catalyst, as described above. The preliminary thin layer chromatography (TLC) analysis of the centrifuged samples of the reaction mixture showed that FAME was not formed, indicating no leaching of the active species.

2. 5. Statistical modeling and optimization

FAME content was correlated with four process factors, namely the reaction temperature, ***A*** (55, 60, and 65 °C), the catalyst loading, ***B*** (10, 15, and 20 % of the oil weight), the methanol-to-oil molar ratio, ***C*** (18 : 1, 21 : 1, and 24 : 1), and the reaction times, ***D*** (60, 120, 180, and 240 min), combining the RSM and a historical data design (total 70 runs). The experimental matrix of the historical data design is presented in Table S-1 (Supplementary Material). The data were normally distributed, and outlier value was not present (Fig. S-1, Supplementary Material). The experiments were conducted in random order. The following quadratic equation was used:

$$Y = b_0 + b_1A + b_2B + b_3C + b_4D + b_{12}AB + b_{13}AC + b_{14}AD + b_{23}BC + b_{24}BD + b_{34}CD + b_{11}A^2 + b_{22}B^2 + b_{33}C^2 + b_{44}D^2 \quad (1)$$

where Y is the FAME content, ***A***, ***B***, ***C*** and ***D*** are process factors, b_0 is the constant regression coefficient, b_i are linear regression coefficients (i = 1, 2, 3, 4), b_{ij} are two-factor interaction regression coefficients (i = 1, 2, 3; j = i +1), and b_{ii} are quadratic regression coefficients (i = 1, 2, 3, 4). The parameters of the quadratic equation were calculated by the non-linear regression method using the Design Expert software (StatEase, USA). Statistical significance of the process factors and their interactions was estimated with a confidence level of 95 % by the analysis of variance (ANOVA). The developed model was statistically assessed by the coefficient of determination, R^2, the predicted coefficient of determination,-R^2_{pred}, the adjusted coefficient of determination, R^2_{adj}, the F_{model}- and p-values, the adequate precision *Adeq. Prec.,* the coefficient of variation, *C.V.*, the mean relative percent deviation *MRPD*, and the lack of fit F_{LOF}. The developed model was then modified by eliminating statistically insignificant terms. Several optimization points, which provided the maximum actual FAME content for a set of reaction conditions, were also determined by the Design Expert software.

3. RESULTS AND DISCUSSION

3. 1. Catalyst characterization

3. 1. 1. Elemental composition of the fWSA catalyst

The average elementary composition of the fWSA sample, based on three EDS spectra for three different positions is presented in Table 2. Although the content of Si, C, and O represents amounts 86 and 90 % of the total detected elements, differences in the contents of Si and C, determined at individual sites, indicate some inhomogeneity of the fWSA sample, most likely due to differences in the presence of some form of silicate phase.

CC BY NC ND

Table 2. Elemental composition of the fWSA catalyst

Spectrum	Content, wt.%								
	C	O	Na	Mg	Si	Cl	K	Ca	Total
1	50.0	23.3	BDL	1.3	12.6	1.4	9.0	2.4	100
2	51.2	21.0	BDL	1.4	17.4	1.2	6.3	1.6	100
3	23.1	42.4	BDL	0.5	24.5	1.4	7.7	0.5	100
Average ± STD	41.4±15.9	28.9±11.8	BDL	1.1±0.5	18.2±6.0	1.3±0.1	7.7±1.4	1.5±0.9	100

*BDL – below detection limit

Dodson [42] pointed out that the physico-chemical properties and elemental composition of WSA depended on the initial elements in wheat straw, which further depend on the wheat straw variety, growing conditions, and biomass species. Similar dependence of the walnut shells elemental composition on geographical region and cultivation conditions was reported by Vassilev [55]. In another study [22] it was found that various potassium (KCl, K_2CO_3), and calcium ($CaMgSiO_4$, $Ca_3(PO_4)_2$) compounds were responsible for the catalytic activity of tucuma peel ash.

3. 1. 2. XRD characterization of the WSA catalysts

X-Ray Diffraction (XRD) patterns of the fWSA, aWSA, sWSA, and sWSA3 (after the third reuse) samples are shown in Figure 1.

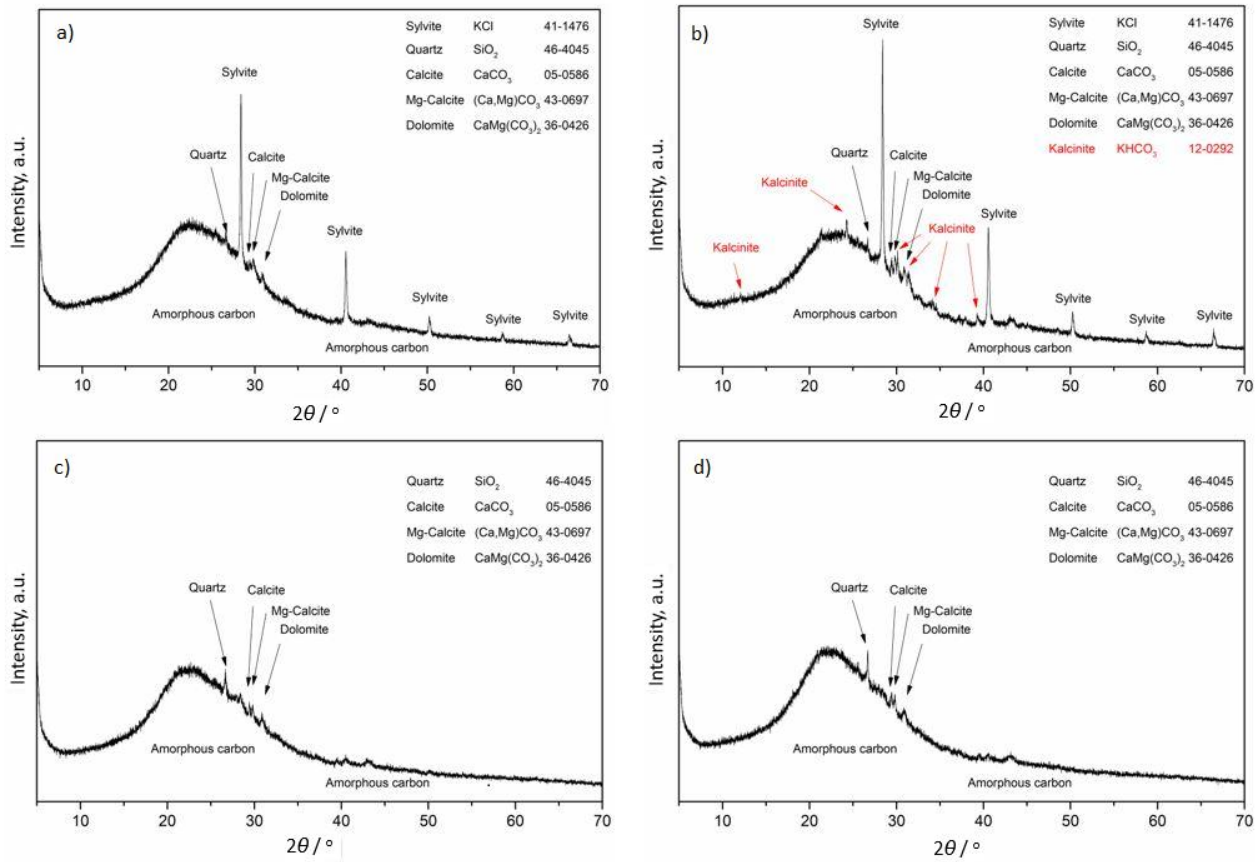

Figure 1. XRD patterns of (a) fWSA (b) aWSA, (c) sWSA (after the first use), and (d) sWSA3 (after the third reuse)

The broad peak (hump) at 23° 2θ is characteristic for any residue of incomplete combustion of biological materials, *i.e.*, biochar, indicating its dominantly amorphous carbon structure [56]. Still, the color of fWSA and aWSA samples was black, suggesting that a significant part of the obtained materials was carbon.

The XRD pattern of the fWSA sample confirms the presence of five phases:

1) quartz (SiO_2) with a characteristic peak at 2θ = 26.64° (PDF#46-1045);

2) calcite ($CaCO_3$) with a characteristic peak at 2θ = 29.41° (PDF#05-0586),

3) dolomite $CaMg(CO_3)_2$ with a characteristic peak at 2θ = 30.94° (PDF#36-0426),

4) Mg-calcite $(Ca,Mg)CO_3$ with a characteristic peak at 2θ = 29.71° (PDF#43-0697), and

5) sylvite (KCl) with characteristic peaks at 2θ = 28.35, 40.51, 50.17, 58.64, and 66.38° (PDF#41-1476).

This mineralogical composition is not unusual for biochars. Moreover, calcite, Mg, Ca-carbonate ($Ca_xMg_{(1-x)}CO_3$), and quartz were the most common crystalline phases identified in biochars [56,57]. In the literature, the presence of quartz in biochar is always associated with contamination of the raw materials from the soil (even after thorough washing) while the presence of the carbonate phases, in addition to the mentioned explanation, is related to the presence of carbonates in the original biomass, and even formation by the entrapment of CO_2, evolving from the thermal decomposition of organic carbon, in the alkaline charred material [56].

Except for sylvite (KCl), the diffractograms of the sWSA and sWSA3 samples (Fig. 1c, d) show the presence of reflections corresponding to the same phases identified in the fWSA sample. In fact, even the strongest reflection of sylvite at 28.4° 2θ is hardly noticeable on the diffraction sample of the sWSA sample and is almost non-existent for the sWSA3 sample (Fig. 1d). Therefore, the observed differences in activity between the fWSA, sWSA, and sWSA3 samples are directly related to the sylvite phase (*i.e.*, K^+ ions) content in the materials.

An uncommon result was obtained for the aWSA sample. A new phase of $KHCO_3$ appeared in the diffractogram (peaks at 12.05, 31.22, 34.06, 39.20°, with the dominant peak at 2θ = 24.23°), which was not detected for the fWSA sample. As $KHCO_3$ is barely soluble in methanol [58], it forms a protective layer on the surface of KCl particles, so that almost all KCl or K^+ ions are inaccessible (blocked) for the reaction.

It is worth noting that the applied process of burning wheat straw did not create the conditions for obtaining CaO by decomposing calcite, Mg-rich calcite, and/or Ca-rich dolomite in the fWSA sample. This suggests that the achieved combustion temperature was not sufficiently high to decompose the carbonate phases, forming CaO and CO_2. Even, at a sufficiently high temperature to decompose the carbonates, CO_2 was formed, changing the atmosphere, which shifted the reaction to the carbonate formation; in other words, the carbonate decomposition was prevented.

3. 1. 3. TPDe of fWSA and aWSA samples

TPDe profiles after CO_2 adsorption by the fWSA and aWSA samples, shown in Figure 2, confirm incomplete carbonization of wheat straw in the applied combustion procedure, as suggested by the results of XRD measurements. Thermal conductivity detector (TCD) signals of both materials did not reach the baseline value in the entire temperature range, even at the highest temperature of 800 °C.

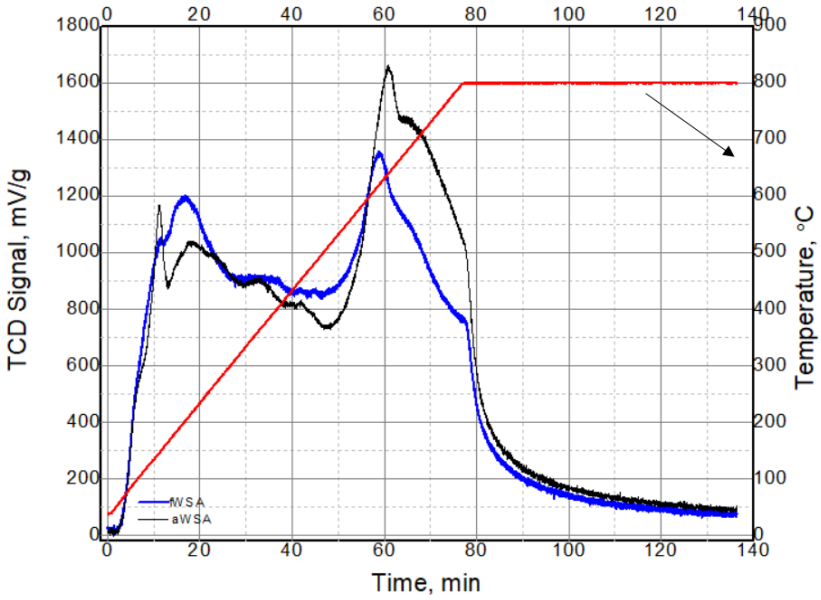

Figure 2. TCD signals of aWSA and fWSA samples

However, difference in the areas below the curves for the freshly carbonized sample (fWSA) and the sample left for 40 days (aWSA) is evident, in favor of the aWSA. The finding is somewhat strange as it is expected that the CO_2 adsorption capacity will be either the same for both materials or larger in the case of a freshly prepared catalyst (fWSA sample). The experimental setup can be ruled out as the cause of the observed difference because the profile of a sample aged for 150 days (aWSA-150) is practically identical to the profile of the 40-day-old sample (aWSA), as can be seen in Figure S-2 (Supplementary Material).

The unexpected results shown in Figure 2 could be most likely related to the composition of the gas phase during temperature-programmed heating of the samples. If the sample decomposed during heating, other gaseous components (*e.g.*, CO, H_2O, and even a fraction of organic molecules) could be found in the carrier gas stream (helium), beside the desorbed CO_2. As the TC detector was not selective, the obtained profile would represent a function of the content and thermal conductivity of all gases formed during the TPD measurement. Better insight can be obtained by analyzing the output mixture of gases using mass spectroscopy (MS). The experimental setup was performed in such a way that the sampling for MS measurements takes place at the position before the trap (Mg-perchlorate) that removes H_2O and the obtained results are shown in Figure 3.

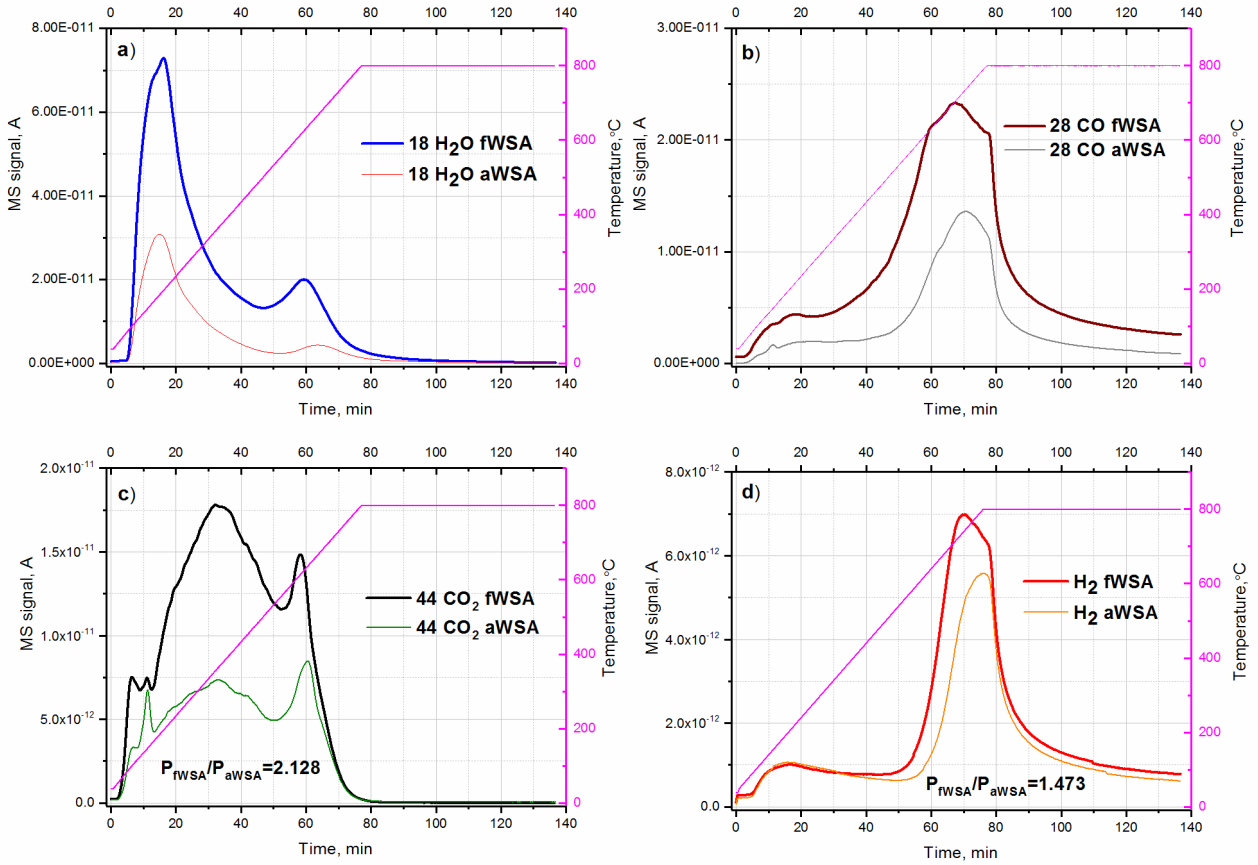

Figure 3. MS signals of H_2O (a), CO (b), CO_2 (c), and H_2 (d) for fWSA and aWSA samples

All selected MS signals (H_2, H_2O, CO, and CO_2) were more intensive for the fWSA sample than for the aWSA sample (Fig. 3), which was not in accordance with the results of TCD in the temperature range of 500-800 °C (Fig. 2). H_2O, CO, and CO_2 have thermal conductivities remarkably lower than the carrier gas. So, the presence of these gases in the carrier gas would reduce the thermal conductivity of the gas mixture, which was detected as an increase in the TCD signal. Since Mg-perchlorate is set as an H_2O trap before the TCD measurement line, the contribution of H_2O in the registered TCD signal is not present. However, in that case, the TCD signal of the fWSA sample would have been higher than the TCD signal of the aWSA sample in the whole applied temperature range (including the range of 500-800 °C). This leads to the conclusion that there must be some other components present in the gas, which decreased the TCD signal of the

fWSA sample. The only remaining gas was H_2. The hydrogen signal registered by the MS detector for the fWSA sample was about 47 % higher (Fig. 3d) than that for the aWSA sample. As the thermal conductivity of hydrogen is higher than the thermal conductivity of the carrier gas which passes through the reference branch of the TC detector, the presence of H_2 in the gas mixture leaving the reactor and passing through the measuring branch of the TC detector causes a decrease in the registered signal. Overall, the hydrogen contribution (signal decrease) exceeds the contribution of CO and CO_2 (signal increase), so the registered TCD signal of the fWSA sample is weaker than that registered for the aWSA sample.

It is worth mentioning that the area below the MS-CO_2 profile for the fWSA sample is more than twice higher than that of the aWSA sample (Fig. 3c). Except for the aging time, the two samples were treated equally, so the different amounts of CO_2 released by sample decomposition could be hardly expected. As the masses of the two samples used for the analysis were almost the same (the difference of less than 2 %), it was clear that the difference in the MS-CO_2 signals was due to different amounts of CO_2 desorbed from the fWSA and aWSA samples. As the desorbed amount of CO_2 is unambiguously connected to the alkalinity of the catalyst surface, the activity of the freshly prepared catalyst has to be higher than that of the aged catalyst.

3. 1. 4. Textural properties of the fWSA and aWSA catalysts

Textural parameters of the fWSA and aWSA samples obtained by low-temperature N_2 physisorption at 77 K and Hg porosimetry measurements are given in Table 3.

Table 3. Textural parameters of the fWSA and aWSA samples obtained by Hg porosimetry and low-temperature N_2 physisorption at 77 K

Method		Hg porosimetry[a]					N_2 physisorption at 77 K[b]		
Sample		$V_{tot\text{-}Hg}$ / $cm^3\,g^{-1}$	ρ_{app} / $g\ cm^{-3}$	ρ_{bulk} / $g\ cm^{-3}$	SSA_{Hg} / $m^2\,g^{-1}$	Porosity, %	V_{mes} / $cm^3\,g^{-1}$	V_{mic} / $cm^3\,g^{-1}$	SSA_{BET} / $m^2\,g^{-1}$
fWSA	Run 1	1.114	0.89	0.45	11.5	49.8	0.041	0.039	98.5
	Run 2	0.095	0.89	0.82	3.1	7.8			
aWSA	Run 1	1.420	1.11	0.43	12.9	61.1	0.029	0.038	90.7
	Run 2	0.066	1.11	1.03	2.9	6.8			

[a]$V_{tot\text{-}Hg}$ – the total cumulative volume, ρ_{app} – the apparent density, ρ_{bulk} – the bulk density, SSA_{Hg} – the total specific surface area; [b]V_{mes} – mesopores volume, V_{mic} – the micropore volume, SSA_{BET} – the specific surface area.

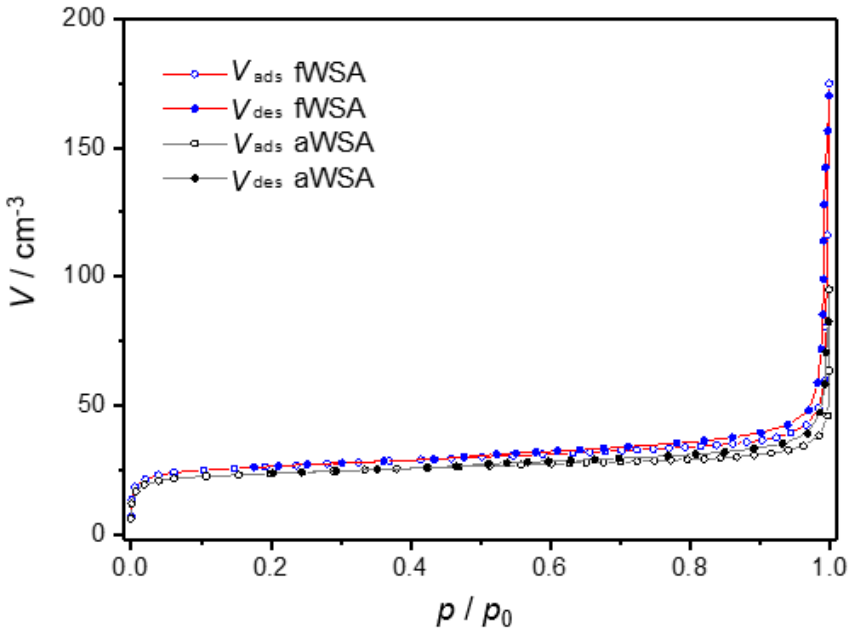

Fig. 4 N_2 adsorption-desorption isotherms of the fWSA and aWSA catalysts

The N_2 adsorption-desorption isotherms of the materials (Fig. 4) are similar and belong to the type II, which is associated with nonporous and macroporous materials. For both materials, the microporous volume is similar (0.040 $cm^3\ g^{-1}$) while the mesoporous volume (V_{mes}) values of the fWSA are for 40 % higher than those of the aWSA, but both values are small. Additionally, the obtained values of the total specific surface area, $SSA_{BET,}$ are considerable and slightly higher for the fWSA compared to that for aWSA (98.5 $m^2\ g^{-1}$ *vs*. 90.7 $m^2\ g^{-1}$).

Further information on the textual properties of both materials can be obtained by analyzing the results of Hg porosimetry measurements (Table 3. and Fig. 5). Due to the small volume of intruded Hg and the clearer presentation of the results, the extrusion-intrusion curves of the Run 2 for the fWSA and aWSA samples are omitted from Fig. 5.

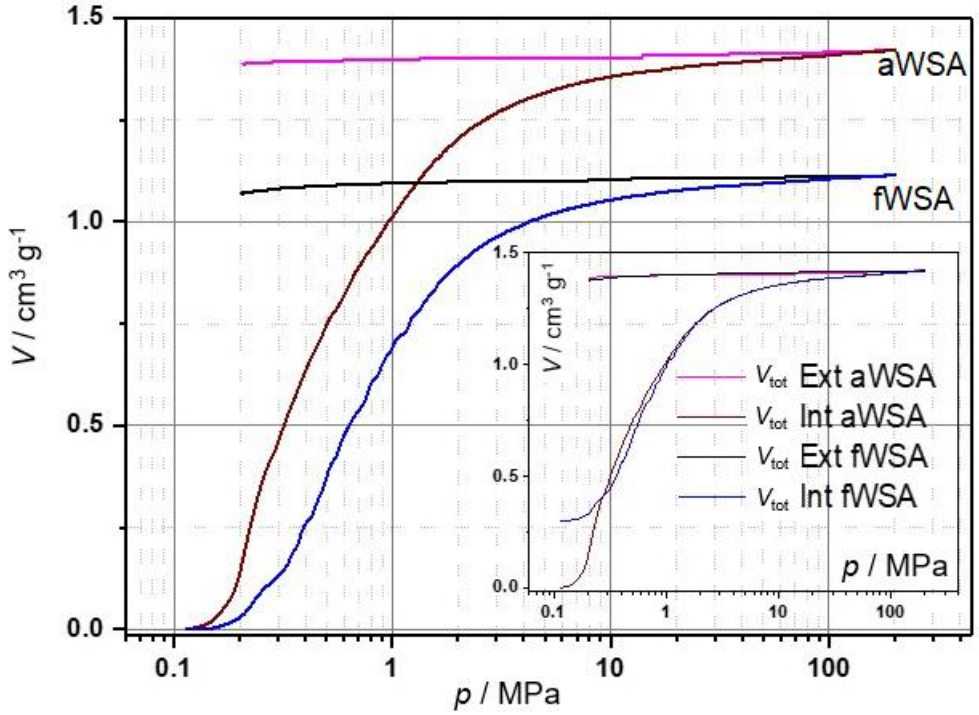

Figure 5. Intrusion/extrusion curves of Hg obtained in Run 1 for the fWSA and aWSA samples; insert: the shifted intrusion/extrusion curves of Run 1 of the fWSA sample

For both materials, the total cumulative volume ($V_{tot\text{-}Hg}$) in Run 1 is quite high, significantly above 1 $cm^3\ g^{-1}$. The $V_{tot\text{-}Hg}$ value of the aWSA sample is higher than that of the fWSA sample, pointing out to different initial interparticle fillings of these materials. In other words, the fWSA sample settles better in the dilatometer than the aWSA sample. The difference in $V_{tot\text{-}Hg}$ can be detected at the intrusion pressures lower than 270 kPa, which corresponds to the pore diameter (D_p) domain from 14 to 5.5 µm. For the intrusion pressures higher than 1 MPa (D_p < 1.5 µm), difference in the $V_{tot\text{-}Hg}$ and Hg intrusion location was not observed (insert in Fig. 5). Additionally, the Run 1 extrusion curves (Fig. 5) for both samples were nearly horizontal, indicating that almost the whole mercury-filled space for both samples were the interparticle space since Hg was not released during the pressure decrease.

It is worth noting that the SSA_{BET} values obtained from the N_2 physisorption measurements are considerably higher than SSA_{Hg} values obtained by the Hg porosimetry measurements (independent of the measurement cycle). Obviously, the most significant part of the specific surface area of the carbonized material originates from the outer surface of the material particles and/or the pore type (micropores and mesopores less than 7.5 nm) inaccessible to the Hg porosimetry measurement.

The huge reduction in the $V_{tot\text{-}Hg}$ value for Run 2, compared to the $V_{tot\text{-}Hg}$ value for Run 1 for both samples clearly show that during the Hg intrusion process of Run 1 compacting of the powder occurred, which is the main reason for differences in porosity obtain for the Runs 1 and 2 (Table 3). Finally, extremely low porosity obtained for the fWSA (7.8 %) and aWSA (6.8 %) samples from $V_{tot\text{-}Hg}$ Run 2, classify these materials as nonporous (for the measured pore diameter range).

Figure 6 shows micrographs of fWSA and sWSA3 samples at different magnifications. At the lowest magnification, there is a clear difference between particle dimensions of the fWSA and WSA3 samples. The particle dimensions of fWSA are larger compared to sWSA3, which can be attributed to the comminution of sWSA3 particles during the catalytic tests caused by mechanical stirring and collision of the catalyst particles. The difference between these two micrographs demonstrates shredding intensity. An even better representation of the difference in the catalyst particle dimensions between fWSA and sWSA3 is seen at the higher magnification (Fig. 6, middle row, magnifications 250×).

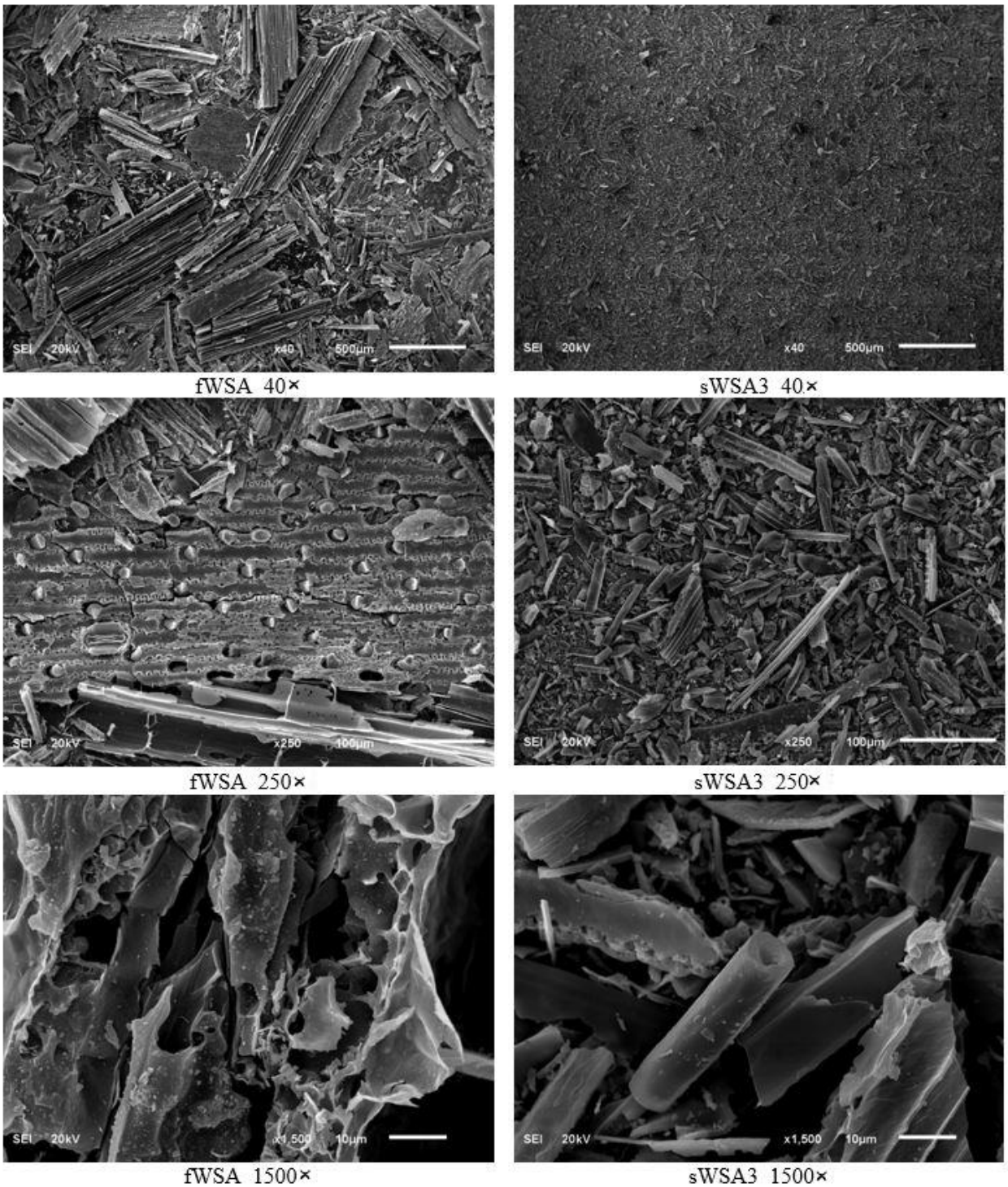

Fig. 6 Micrographs of fWSA (left column) and sWSA3 (right column) samples at different magnifications (scale bars: the top row = 500 μm; the middle row = 100 μm; the bottom row = 10 μm)

CC BY NC ND

3. 2. Catalytic testing of the fWSA catalyst

Figure 7 demonstrates the catalytic activity of the fWSA catalyst in methanolysis of sunflower oil by showing sigmoid variations of FAMEs and triacylglycerols (TAGs) contents with time. At the reaction temperature of 55 °C, the catalyst loading of 15 %, and the methanol-to-oil molar ratio of 18:1, the FAME content increases on account of a decrease in the TAG content with the progress of the reaction while low contents of intermediates, monoacylglycerols (MAGs) and diacylglycerols (DAGs), slightly increase with time, reaching the maxima (about 0.1 % MAGs and 1.0 % DAGs) and then remain nearly constant or decrease slightly until the reaction is completed. These variations are typical for methanolysis reactions of vegetable oils.

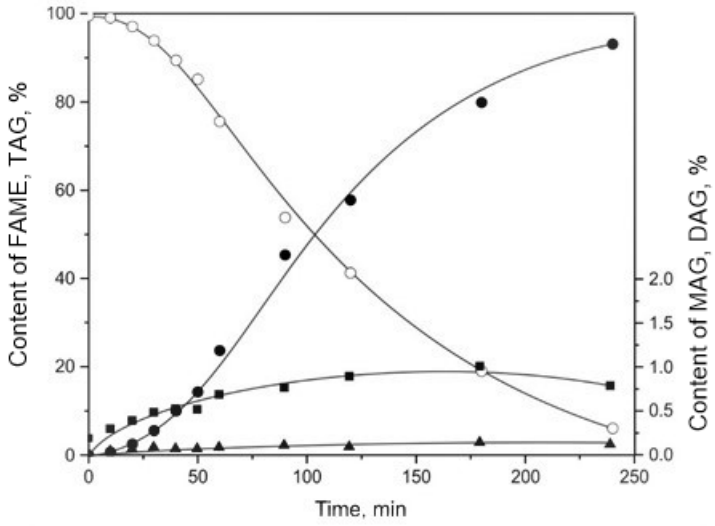

Figure 7. Variation of the reaction mixture composition with the progress of sunflower oil methanolysis catalyzed by fWSA (the reaction temperature of 55 °C, the catalyst loading of 15% of the oil weight, and the methanol-to-oil molar ratio of 18:1; FAMEcontent - ●, MAG content - ▲, DAG content - ■, and TAG content - ○)

A CaO–based palm kernel ash showed similar catalytic activity as the fWSA catalyst, giving the yield of 99 % in 240 min [20]. The catalytic activity of most agro-waste-based ashes presented in Table 1 is based on K-species, showing similarly high yields but in shorter reaction times, which indicates higher activity than that of the fWSA catalyst.

Physicochemical properties of the biodiesel obtained from sunflower oil using methanol and the fWSA catalyst under the optimal reaction conditions (the reaction temperature of 60.3 °C, the catalyst loading of 11.6 % of the oil weight, the methanol-to-oil molar ratio of 18.3:1, and the reaction time of 124 min) are compared in Table 4 with the limit values prescribed by the EN 14214 biodiesel quality standard. The contents of FAMEs (98.6 %) and MAGs (0.2 %) in the obtained biodiesel product were within the standard limits (>96.5 and <0.7 %, respectively) while the contents of DAGs (0.8 %) and TAGs (0.3 %) were higher than the specified limits (<0.2 %), requiring further purification of the obtained biodiesel. Depending on the concentration of unreacted TAG and DAG in biodiesel, its viscosity can increase, causing a reduction in the combustion efficiency, clogging of the fuel filter, and deposition on engine parts such as pistons, valves, and injector nozzles [59].

Table 4. Physiochemical properties of the biodiesel obtained over the fWSA catalyst

Property	FAME	EN 14214
Density (15 °C), kg m^{-3}	866.9	860-900
Kinematic viscosity (40 °C), m^2 s^{-1}	3.69×10^{-6}	$(3.5\text{-}5.0)\times10^{-6}$
Acid value, mg KOH g^{-1}	0.1	0.50 max
Iodine value, g I_2 $(100\ g)^{-1}$	110	120 max
Water content, mg kg^{-1}	490	500 max
FAME content, %	98.6	96.5 min
MAG content, %	0.2	0.7 max
DAG content, %	0.8	0.2 max
TAG content, %	0.3	0.2 max

Decrease in the catalytic activity with the repeated use of the spent catalyst is shown in Figure 8. The WSA-based catalyst loses the catalytic activity in each subsequent use under the optimal reaction conditions determined by the statistical optimization, which is undesirable. After the first and second reuse, the FAME content after the reaction time of 4 h decreased to 37 and 12 %, respectively, while it was only 3 % after the third reuse. The decrease in the FAME content with the catalyst reuse could be due to the incomplete separation of the fWSA catalyst from the reaction mixture, partial deactivation of the catalyst during the reaction and separation or covering the surface of the catalyst by the reaction products that reduces the number of active sites.

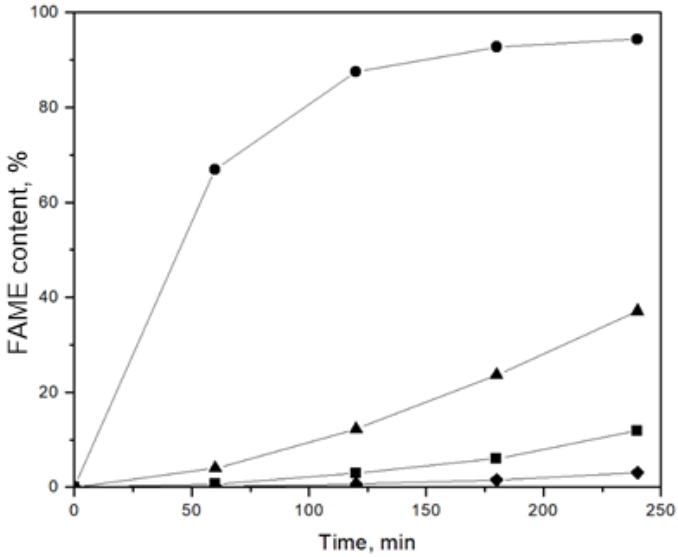

Figure 8. FAME content as a function of reaction time in the repeated use of the WSA catalyst: fWSA - ●; sWSA1 (first reuse) - ▲; sWSA2 (second reuse) - ■; and sWAS3 (third reuse) - ♦ (optimal reaction conditions: the reaction temperature of 60.3 °C, the catalyst loading of 11.6 % of the oil weight, and the methanol-to-oil molar ratio of 18.3:1)

3. 3. Analysis of the methanolysis reaction

Generally, transesterification of TAG is affected by four main operating conditions: reaction temperature, methanol-to-oil molar ratio, catalyst loading, and reaction time, as can be seen in Figure 9.

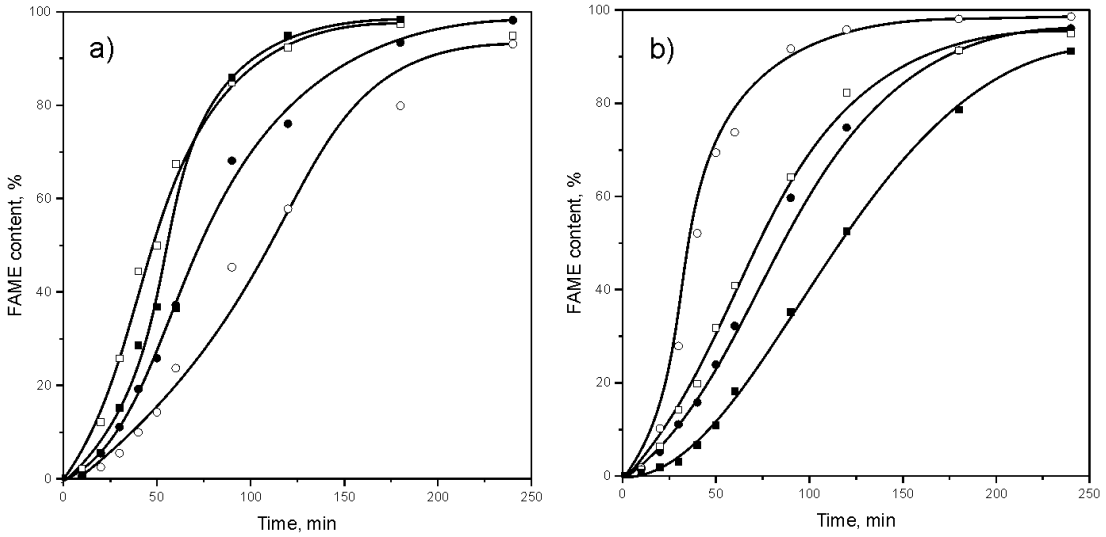

Figure 9. FAME content as a function of the reaction time at different reaction conditions. a) Influence of the reaction temperature and methanol-to-oil molar ratio on FAME synthesis at the catalyst loading of 15 % (reaction temperature 55 °C: methanol-to-oil molar ratio: 18:1 – ○, 24:1 – ● and reaction temperature 65 °C: methanol-to-oil molar ratio: 18:1 – □, 24:1 – ■; b) Influence of the catalyst loading and methanol-to-oil molar ratio on FAME synthesis at the reaction temperature of 60 °C (methanol-to-oil molar ratio: 18:1: catalyst loading: 10 % – ○, 20 %– ● and methanol-to-oil molar ratio: 24:1: catalyst loading: 10 % – □, 20 % – ■)

CC BY NC ND

Figure 9a shows the FAME content at the catalyst loading of 15 %, two different reaction temperatures (55 and 65 °C) and two methanol-to-oil molar ratios (18 : 1 and 24 : 1). At the lower methanol-to-oil molar ratio (18 : 1), the reaction rate increased with the temperature rise. The importance of the reaction temperature came out from the increase in the reaction rate constant at higher temperatures, which accelerated the FAME synthesis. However, the reaction temperature showed negligible influence on the FAME synthesis at the higher methanol-to-oil molar ratio (24 : 1), thus implying that its influence in the applied range (55-65 °C) was repressed by the increased methanol-to-oil molar ratio.

The FAME content variations with time at a constant reaction temperature (60 °C) at different catalyst loadings (10 and 20 %) and methanol-to-oil molar ratios (18 : 1 and 24 : 1) are compared in Figure 9b. As can be seen, the reaction rate decreased with increasing the catalyst loading for both methanol-to-oil molar ratio. The reaction rate at 10 % of catalyst loading was higher for the lower methanol-to-oil molar ratio while the slowest reaction was observed at the catalyst loading of 20 % and the methanol-to-oil molar ratio of 24:1. This could be explained by aggravated mixing and poor contact of the liquid phase with the active sites of the catalyst.

3. 4. Statistical modeling and optimization

Acceptability of the statistical models was firstly tested by the sequential sum of squares, lack of fit, and model summary statistic tests that aimed at selecting the model having the highest order, insignificant lack-of-fit and maximized the R^2_{adj} and R^2_{pred} values, respectively. According to these tests, the aliased cubic model was disregarded while the quadratic model was suggested as it had the highest order and the highest R^2, R^2_{adj}, and R^2_{pred} values among the other models (Tables S-2 and S-3, Supplementary Material) despite its significant lack-of-fit (Table S-4, Supplementary Material). Hence, the quadratic model was further evaluated by the ANOVA (Table 5) that confirmed its significance by its high *F*-value (20.99) and its low *p*-value (< 0.0001). The quadratic equations in terms of coded and actual process factors are given in the Supplementary material, Eqs. (S-1) and (S-2)**.** The ANOVA showed that at a confidence level of 95 % only the catalyst loading (*B*), the reaction time (*D*), and their interaction (*B*x*D*), as well as the squared reaction temperature, catalyst loading, and reaction time (A^2, B^2, and D^2) were significant model terms (Table 5).

Table 5. ANOVA results for the quadratic model

Source	Sum of squares	Degree of freedom	Mean square	*F*-value	*p*-value
Model	38212.0	14	2729.4	20.99	**< 0.0001**
A	111.5	1	111.5	0.86	0.358
B	5198.9	1	5198.9	39.99	**< 0.0001**
C	229.2	1	229.2	1.76	0.190
D	21110.2	1	21110.2	162.37	**< 0.0001**
*A*x*B*	98.1	1	98.1	0.75	0.389
*A*x*C*	486.1	1	486.1	3.74	0.058
*A*x*D*	189.3	1	189.3	1.46	0.233
*B*x*C*	1.7	1	1.7	0.01	0.908
*B*x*D*	1101.7	1	1101.7	8.47	**0.005**
*C*x*D*	227.2	1	227.2	1.75	0.192
A^2	2733.2	1	2733.2	21.02	**< 0.0001**
B^2	4258.9	1	4258.9	32.76	**< 0.0001**
C^2	108.2	1	108.2	0.83	0.366
D^2	2813.4	1	2813.4	21.64	**< 0.0001**
Residual	7150.8	55	130.0		
Lack of Fit	7115.4	50	142.3	20.10	**0.002**
Pure Error	35.4	5	7.1		
Corrected Total	45362.7	69			

Having the highest *F*-value of 162.37, the reaction time was the most important variable affecting the FAME content, followed by catalyst loading, which agreed with the optimization results of the methanolysis of corn germ oil using corn cobs ash as a catalyst [27]**.** On the other hand, Kostić *et al.* [20] showed for methanolysis of sunflower oil over palm kernel shell biochar that the reaction temperature and the methanol-to-oil molar ratio were statistically significant for the FAME content while the effect of catalyst loading was statistically insignificant. The observed effect of the reaction time was expected because of the increase in the FAME content with the reaction progress. However, unlike in the present work, the increase in the reaction time over a certain limit diminished the yield of produced methyl esters [9,11,12]**.**

Interaction of the catalyst loading and the reaction time had a positive effect on the FAME content, which increased with the increase in both parameters. At the higher amounts of the catalyst the number of active sites on the catalyst surface, where the reaction occurs, is increased, thereby increasing the FAME content. This trend was observed up to about 15 % of the catalyst amount, after which the FAME content decreased, probably due to the increased viscosity of the reaction mixture and therefore aggravated mixing at higher amounts of the catalyst. Similar positive effect of the catalyst loading on the *Ceiba pentandra* oil methyl esters formation was observed in literature [9,11,12], while Betiku *et al*. [16] observed a decrease in the neem seed oil methyl esters yield with the increase in the catalyst loading and the reaction time over certain values. In the studied range of operating conditions, Betiku and Ajala [7] observed a continuous increase in the yellow oleander oil methyl esters yield with the increase in the reaction time and catalyst loading, indicating significant interactions between the two variables. Also, a high palm kernel oil methyl ester yield was reported at a prolonged reaction time independently of the catalyst amount [8].

The final hierarchical quadratic equations in terms of statistically significant actual and coded process factors, which include the insignificant reaction temperature (*A*), are as follows:

- Coded factors:

$$Y = 101.60 + 2.10A - 11.60B + 24.21D + 7.31B \cdot D - 12.55A^2 - 15.80\,B^2 - 15.86\,D^2 \quad (2)$$

- Actual factors:

$$Y = 1886.06 + 60.66A - 14.20B + 0.613D + 0.016 \cdot D - 0.502A^2 - 0{,}632\,B^2 - 0.002\,D^2 \quad (3)$$

The goodness of fit and adequacy of the developed hierarchical quadratic model was statistically assessed based on several criteria. The R^2-value of 0.811 larger than the acceptable limit of 0.80 [60] pointed out a fairly good fit of the hierarchical quadratic model that explained 81.1 % of the total variation in the FAME content, confirming the relevance to the hierarchical quadratic model for biodiesel production. The R^2_{pred}- and R^2_{adj}-values (0.789 and 0.761, respectively) differed less than the acceptable limit of 0.2 [61], confirming the good fit of the developed hierarchical quadratic model. In addition, this model had a high F_{model}-value (37.9), higher than its critical value ($F_{(0.05,\ 69,\ 70)}$ = 1.39), and a very low *p*-value (< 0.0001), implying its statistical significance of this quadratic model within the 95 % confidence level (Table 6). Furthermore, the *Adeq.Prec.*-value (24.6), which measured the signal/noise ratio for the tested system, was higher than 4, which was desirable [62], implying an adequate signal for the hierarchical quadratic model. Meanwhile, the coefficient of variation was 16 %, revealing the good precision of this model [63]. Finally, the *MRPD*-value of $\pm$14.6 (70 data) also implied the acceptability of this hierarchical quadratic model, which can be also seen in Figure S1c (Supplementary Material). Relative deviations between the predicted and actual FAME content-values in the range of 40-120 % (4 data) were observed at FAME contents lower than about 25 %; by excluding these runs from the analysis, the *MRPD*-value was reduced to $\pm$10.6 % (66 data).

The ANOVA (Table 6) showed, however, an undesirable significant lack-of-fit for this model (p = 0.001 < 0.050). The significant lack-of-fit meant that the variation of the replicates about their mean values was lower than the variation of the experimental points about their predicted values. A high precision of measuring the FAME content, indicated by the mean relative error between the replicates (runs 13/14, 27/28, 41/42, 55/56, and 69/70, Table S-1- Supplementary Material) of only ±1.3 %, caused a small pure error because of small deviations between the replicates [64] and hence, the significant lack of fit. This is confirmed in Figure 10, which clearly showed that the replicate experimental points are mostly above the response surface. Therefore, the significant lack of fit might refer to the existence of this systematic variation that could not be described by the hierarchical quadratic model. Since the other statistical criteria assessed

CC BY NC ND

this model as a good one, its significant lack of fit, attributed to the small variance of replicated measurements, does not invalidate the model, which could be safely used for modeling and optimization the FAME content in terms of the selected process variables.

Table 6. ANOVA results for the hierarchical quadratic model including only the significant terms

Source	Sum of squares	df	Mean square	*F*-value	*p*-value
Model	36770.1	7	5252.9	37.9	< 0.0001
A	176.8	1	176.8	1.3	0.263[a]
B	5198.9	1	5198.9	37.5	< 0.0001
D	21110.2	1	21110.2	152.3	< 0.0001
BxD	1101.7	1	1101.7	7.9	0.006
A^2	2625.0	1	2625.0	18.9	< 0.0001
B^2	4158.0	1	4158.0	30.0	< 0.0001
D^2	2813.4	1	2813.4	20.3	< 0.0001
Residual	8592.7	62	138.6		
Lack of Fit	8557.3	57	150.1	21.2	0.001
Pure Error	35.4	5	7.1		
Corrected Total	45362.8	69			

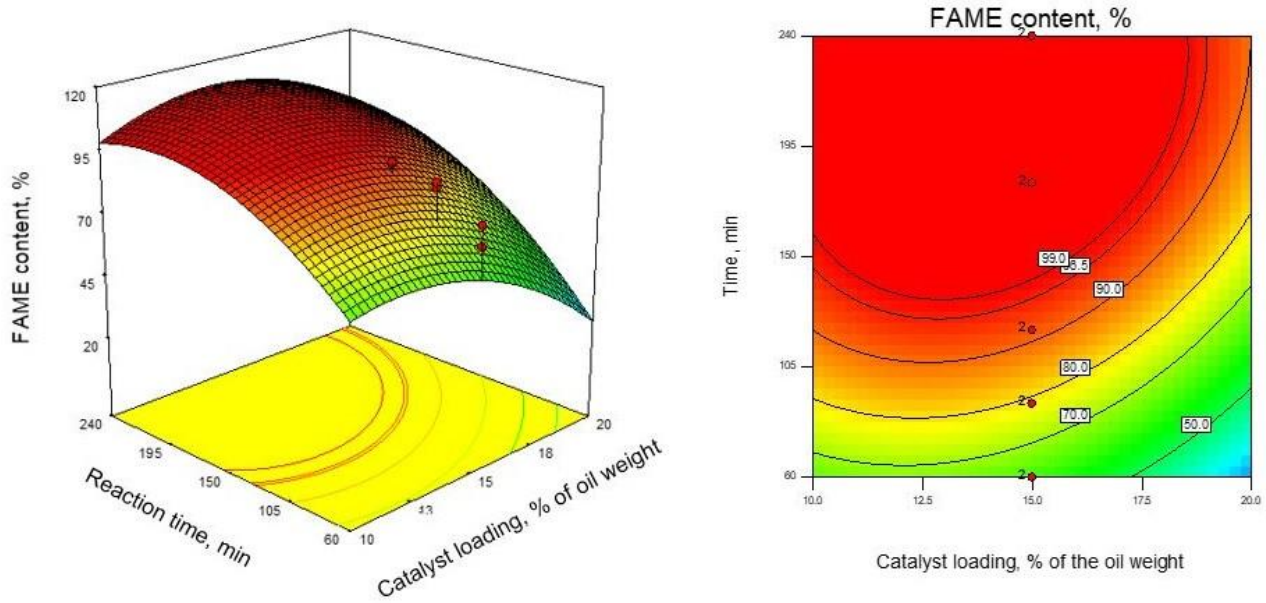

Figure 10. The response surface (a) and contour (b) plots for the FAME content as a function of catalyst loading and reaction time according to the hierarchical quadratic model (reaction temperature: 60 °C and methanol-to-oil molar ratio: 21:1)

Figure 10 shows the response surface and contour plots for the FAME content as a function of the catalyst loading and the reaction time according to the hierarchical quadratic model while keeping the reaction temperature and methanol-to-oil molar ratio constant at their medium levels (60 °C and 21:1, respectively). The FAME content increases with the progress of the reaction independently of the catalyst loading while it increases with increasing the catalyst loading until reaching a maximum at about 15 % of the oil weight and then decreases, as can be seen in Figure 10a.

The contour plot in Figure 10b shows a weak interaction between the catalyst loading and the reaction time. Besides that, it is obvious that the FAME content higher than the limit value of 96.5 % can be reached in wide ranges of the catalyst loading and reaction time, *i.e.*, for their various combinations. Also, the used software suggested several combinations of the process variables providing the targeted actual maximum FAME content of 98.6 %, as can be seen in Table S-5 (Supplementary Material). Taking the minimum methanol-to-oil molar ratio ensuring the desired FAME content as an additional criterion, the following process conditions were found to be optimum: the reaction temperature of 60.3 °C, the

catalyst loading of 11.6 % (based on the oil weight), the methanol-to-oil molar ratio of 18.3 : 1, and the reaction time of 124 min.

4. CONCLUSION

Wheat straw as waste biomass is frequently used for energy production by direct combustion, producing ash as a by-product. The fWSA catalyst, obtained by the combustion of wheat straw at open air, consists of five phases: quartz, calcite, dolomite, Mg-calcite, and sylvite. A new phase of $KHCO_3$ (hardly soluble in methanol) was detected in the aWSA sample, thus explaining its low activity. Increase in the methanolysis reaction rate with increasing the reaction temperature was observed only at the lowest methanol-to-oil molar ratio (18 : 1). The reaction rate increased with the increase in the methanol-to-oil molar ratio from 18 : 1 to 24 : 1 at the lowest catalyst loading (10 %), opposite to the highest catalyst loading of 20 %, as the result of aggravated mixing and therefore a poor contact of the liquid phase with the active sites of the catalyst. The optimum reaction conditions were found to be the reaction temperature of 60.3 °C, the catalyst loading of 11.6 % (based on the oil weight), the methanol-to-oil molar ratio of 18.3, and the reaction time of 124 min and provided the 98.6 % FAME. The fWSA catalyst showed a similarly high FAME yield as most agro-waste-based ashes having K-based active species but in longer reaction times, indicating its lower activity compared to these catalysts. Further research should focus on increasing the stability of the catalyst activity and on reducing the volume of the catalyst by compression (briquettes or pellets) or incorporation into various carriers which would facilitate the catalyst reuse.

Acknowledgements: This work has been funded by the Republic of Serbia - Ministry of Education, Science and Technological Development of Serbia, Programs for Financing Scientific Research Work, No. 451-03-9/2021-14/200133 (Project assigned to the Faculty of Technology, Leskovac, University of Niš, Research group III 45001), No. 451-03-9/2021-14/200026 (Project assigned to the University of Belgrade - Institute of Chemistry, Technology and Metallurgy – The National Institute, Belgrade), and No. 451-03-9/2021-14/200155 (Project assigned to the Faculty of Technical Sciences, Kosovska Mitrovica, University of Priština), as well as by the Serbian Academy of Sciences and Arts (Project F-78).

REFERENCES

[1] Global Bioenergy Statistics 2019, World Bioenergy Association, 2019. https://worldbioenergy.org/uploads/191129%20WBA%20GBS%202019_HQ.pdf, Assessed 25.2.2021

[2] Shan R, Lua L, Shi Y, Yuan H, Shi J. Catalysts from renewable resources for biodiesel production. *Energy Convers Manage* 2018; 178: 277-289. https://doi.org/10.1016/j.enconman.2018.10.032

[3] Baskar G., I. Aberna Ebenezer Selvakumari, R. Aiswarya, Biodiesel production from castor oil using heterogeneous Ni doped ZnO nanocatalyst, *Bioresour Technol.* 2018; 250: 793-798. https://doi.org/10.1016/j.biortech.2017.12.010

[4] Veličković AV, Avramović JM, Stamenković OS, Veljković VB. Kinetics of the sunflower oil ethanolysis using CaO as catalyst. *Chem Ind Chem Eng Q.* 2016; 22: 409-418. https://doi.org/10.2298/CICEQ160106003V

[5] Nakomčić-Smaragdakis B, Čepić Z, Dragutinović N. Wheat straw combustion process and its impact on air pollution. *Cont Agric Eng.* 2014; 40: 50-62. UDK: 662.767.2:536.46

[6] Etim AO, Betiku E, Ajala SO, Olaniyi PJ, Ojumu TV. Potential of ripe plantain fruit peels as an ecofriendly catalyst for biodiesel synthesis: Optimization by artificial neural network integrated with genetic algorithm. *Sustainability*. 2018; 10: 1-15. https://doi.org/10.3390/su10030707

[7] Betiku E, Ajala SO. Modeling and optimization of *Thevetia peruviana* (yellow oleander) oil biodiesel synthesis via *Musa paradisiacal* (plantain) peels as heterogeneous base catalyst: A case of artificial neural network vs. response surface methodology. *Ind Crops Prod.* 2014; 53: 314-322. https://doi.org/10.1016/j.indcrop.2013.12.046

[8] Odude VO, Adesina AJ, Oyetunde OO., O.O. Adeyemi, N.B. Ishola, A.O. Etim, E. Betiku, Application of agricultural waste-based catalysts to trans esterification of esterified palm kernel oil into biodiesel: A case of banana fruit peel versus cocoa pod husk. *Waste Biomass Valor.* 2017; 10: 877-888. https://doi.org/10.1007/s12649-017-0152-2

[9] Betiku E, Akintunde AM, Ojumu TV. Banana peels as a biobase catalyst for fatty acid methyl esters production using napoleon's plume (*Bauhinia monandra*) seed oil: A process parameters optimization study. *Energy* 2016; 103: 797-806. https://doi.org/10.1016/j.energy.2016.02.138

[10] Gohain M, Devi A, Deka D. *Musa balbisiana* Colla peel as highly effective renewable heterogeneous base catalyst for biodiesel production. *Ind Crops Prod.* 2017; 109: 8-18. https://doi.org/10.1016/j.indcrop.2017.08.006

[11] Balaji M, Niju S. A novel biobased heterogeneous catalyst derived from *Musa acuminate* peduncle for biodiesel production – Process optimization using central composite design. *Energy Convers Manage*. 2019; 189: 118-131. https://doi.org/10.1016/j.enconman.2019.03.085

CC BY NC ND

[12] Balaji M, Niju S. Banana peduncle - A green and renewable heterogeneous base catalyst for biodiesel production from *Ceiba pentandra* oil. Renewable *Energy* 2020; 146: 2255-2269. https://doi.org/10.1016/j.renene.2019.08.062

[13] Deka DC, Basumatary S. High quality biodiesel from yellow oleander (*Thevetia peruviana*) seed oil. *Biomass Bioenergy* 2011; 35: 1797-1803. https://doi.org/10.1016/j.biombioe.2011.01.007

[14] Sarma AK, Kumar P, Aslam M, Chouhan APS. Preparation and characterization of *Musa balbisiana* Colla underground stem nano-material for biodiesel production under elevated conditions. *Catal Lett.* 2014; 144: 1344-1353. https://doi.org/10.1007/s10562-014-1206-8

[15] Aslam M, Saxena P, Sarma AK. Green technology for biodiesel production from *Mesua ferrea* L. seed oil. *Energy Environ. Res.* 2014; 4 (2): 11-21. https://doi.org/10.5539/eer.v4n2p11

[16] Betiku E, Etim AO, Pereao O, Ojumu TV. Two-step conversion of neem (*Azadirachta indica*) seed oil into fatty methyl esters using a heterogeneous biomass-based catalyst: An example of cocoa pod husk. *Energy Fuels* 2017; 31: 6182-6193. https://doi.org/10.1021/acs.energyfuels.7b00604

[17] Vadery V, Narayanan BN, Ramakrishnan RM, Cherikkallinmel SK, Sugunan S, Narayanan DP, Sasidharan S. Room temperature production of jatropha biodiesel over coconut husk ash. *Energy* 2014; 70: 588-594. https://doi.org/10.1016/j.energy.2014.04.045

[18] Hindryawati N, Maniam GP, Karim MR, Chong KF. Transesterification of used cooking oil over alkali metal (Li, Na, K) supported rice husk silica as potential solid base catalyst. *Eng. Sci .Technol. Int. J*. 2014; 17: 95-103. https://doi.org/10.1016/j.jestch.2014.04.002

[19] Miladinović MR, Zdujić MV, Veljović ĐN, Krstić JB, Banković-Ilić IB, Veljković VB, Stamenković OS. Valorization of walnut shell ash as a catalyst for biodiesel production. *Renewable Energy* 2020; 147: 1033-1043. https://doi.org/10.1016/j.renene.2019.09.056

[20] Kostić MD, Bazargan A, Stamenković OS, Veljković VB, McKay G. Optimization and kinetics of sunflower oil methanolysis catalyzed by calcium oxide-based catalyst derived from palm kernel shell biochar. *Fuel* 2016; 163: 304-313. https://doi.org/10.1016/j.fuel.2015.09.042

[21] Laskar IB, Gupta R, Chatterjee S, Vanlalveni C, Rokhum L. Taming waste: Waste Mangifera indica peel as a sustainable catalyst for biodiesel production at room temperature. *Renewable Energy* 2020; 161: 207-220. https://doi.org/10.1016/j.renene.2020.07.061

[22] Mendonça IM, Paes OARL, Maia PJS, Souza MP, Almeida RA, Silva CC, Duvoisin S Jr., de Freitas FA. New heterogeneous catalyst for biodiesel production from waste tucuma peels (*Astrocaryum aculeatum* Meyer): Parameters optimization study. *Renewable Energy* 2019; 130: 103-110. https://doi.org/10.1016/j.renene.2018.06.059

[23] Uprety B.K, Chaiwong W, Ewelike C, Rakshit SK. Biodiesel production using heterogeneous catalysts including wood ash and the importance of enhancing byproduct glycerol purity. *Energy Convers. Manage.* 2016; 115: 191-199. https://doi.org/10.1016/j.enconman.2016.02.032

[24] Aleman-Ramirez JL, Moreira J, Torres-Arellano S, Longoria A, Okoye PU, Sebastian PJ. Preparation of a heterogeneous catalyst from moringa leaves as a sustainable precursor for biodiesel production. *Fuel* 2021; 284: 118983. https://doi.org/10.1016/j.fuel.2020.118983

[25] Barros S de S, Pessoa Junior WAG, Sá ISC, Takeno ML, Nobre FX, Pinheiro W, Manzato L, Iglauer S, de Freitas FA. Pineapple (*Ananás comosus*) leaves ash as a solid base catalyst for biodiesel synthesis. *Bioresour Technol.* 2020; 312: 123569. https://doi.org/10.1016/j.biortech.2020.123569

[26] Nath B, Das B, Kalita P, Basumatary S. Waste to value addition: Utilization of waste *Brassica nigra* plant derived novel green heterogeneous base catalyst for effective synthesis of biodiesel. *J Cleaner Prod.* 2019; 239: 118112. https://doi.org/10.1016/j.jclepro.2019.118112

[27] Kostić MD, Tasić MB, Đalović IG, Biberdžić MO, Mitrović PM, Stamenković OS, Veljković VB. Optimization of biodiesel production from corn oil by methanolysis catalyzed by corn cob ash. *Recycl. Sustainable Dev.* 2018; 11: 53-62. https://doi.org/10.5937/ror1801053K

[28] Vinu V, Binitha NN. Lithium silicate based catalysts prepared using arecanut husk ash for biodiesel production from used cooking oil. *Mater Today: Proc.* 2020; 25: 241-245. https://doi.org/10.1016/j.matpr.2020.01.210

[29] Changmai B, Rano R, Vanlalveni C, Rokhum L. A novel *Citrus sinensis* peel ash coated magnetic nanoparticles as an easily recoverable solid catalyst for biodiesel production. *Fuel* 2021; 286: 119447. https://doi.org/10.1016/j.fuel.2020.119447

[30] Gouran A, Aghel B, Nasirmanesh F. Biodiesel production from waste cooking oil using wheat bran ash as a sustainable biomass. *Fuel* 2021; 295: 120542. https://doi.org/10.1016/j.fuel.2021.120542

[31] Jaćimović G, Malešević M, Bogdanović D, Marinković B, Crnobarac J, Latković D, Aćin V. Wheat yield depending on long-term harvest residue incorporation. *Letopis naučnih radova* 2009; 33: 85-92. UDK: 633.11:631.82.

[32] Kim SH, Gregory JM. Straw to grain ratio equation for combine simulation. *J Biosyst Eng.* 2015; 40: 314-319. http://dx.doi.org/10.5307/JBE.2015.40.4.314

[33] Wieser H, Milijić V. Dostupnost poljoprivredne biomase u Srbiji, Deutsche Gesellschaft für Internationale Zusammenarbeit (GIZ) GmbH. Availability of agro-biomass in Serbia. 2017. http://www.bioenergy-serbia.rs/images/documents/studies/20171028_Agrobiomass_Study.pdf, Assessed January 4, 2020.

[34] Khushnood RA, Rizwan SA, Memon SA, Tulliani J-M, Ferro GA. Experimental investigation on use of wheat straw ash and bentonite in self-compacting cementitious system. *Adv. Mater. Sci. Eng.* 2014; 2014: 832508. http://dx.doi.org/10.1155/2014/832508

[35] Ahmad MR, Sharif MB, Ali HA, Hussain M, Chen B. Experimental investigation of pozzolanic concrete containing wheat straw ash. *Can. J. Civ. Eng.* 2019; 46: 941-951. https://doi.org/10.1139/cjce-2017-0419.

[36] Amin MN, Murtaza T, Shahzada K, Khan K, Adil M. Pozzolanic potential and mechanical performance of wheat straw ash incorporated sustainable concrete. *Sustainability* 2019; 11: 519. https://doi.org/10.3390/su11020519.

[37] Jankovský O, Pavlíková M, Sedmidubský D, Bouša D, Lojka M, Pokorný J, Záleská M, Pavlí Z. Study on pozzolana activity of wheat straw ash as potential admixture for blended cements. *Ceram.-Silik.* 2017; 61: 327-339. http://dx.doi.org/10.13168/cs.2017.0032

[38] Memon SA, Wahid I, Khan MK, Tanoli MA, Bimaganbetova M. Environmentally friendly utilization of wheat straw ash in cement-based composites. *Sustainability* 2018; 10: 1322. https://doi.org/10.3390/su10051322

[39] Qudoos A, Kim HG, Atta-ur-Rehman, Jeon IK, Ryou J-S. Influence of the particle size of wheat straw ash on the microstructure of the interfacial transition zone. *Powder Technol.* 2019; 352: 453-461. https://doi.org/10.1016/j.powtec.2019.05.005

[40] Sharma G, Singh K. Agro-waste ash and mineral oxides derived glass-ceramics and their interconnect study with Crofer 22 APU for SOFC application. *Ceram. Int.* 2019; 45: 20501-20508. https://doi.org/10.1016/j.ceramint.2019.07.029

[41] Bartůněk V, Sedmidubský D, Bouša D, Jankovský O. Production of pure amorphous silica from wheat straw ash. *Green Mater*. 2018; 6: 1-5. https://doi.org/10.1680/jgrma.17.00035

[42] Dodson J. Wheat straw ash and its use as a silica source. 2011; Ph. D. Thesis, Univ. York, UK, 2011.

[43] Pokorný J, Pavlíková M, Jankovský O, Łagód G, Pavlík Z. Properties of wheat straw ash geopolymer for construction use. In: Proceedings of 19th International Multidisciplinary Scientific GeoConference SGEM 2019. Sofia, Bulgary, 2019, pp. 239-246. https://doi.org/10.5593/sgem2019/6.2/S26.031

[44] Wang X, Yao K, Huang X, Chen X, Yu G, Liu H, Wang F, Fan M. Effect of CaO and biomass ash on catalytic hydrogasification behavior of coal char. *Fuel* 2019; 249: 103-111. https://doi.org/10.1016/j.fuel.2019.03.025

[45] Ali MMM, Ahmed MJ. Adsorption behavior of doxycycline antibiotic on NaY zeolite from wheat (*Triticum aestivum*) straws ash. *J. Taiwan Inst. Chem. Eng.* 2017; 81: 218-224. https://doi.org/10.1016/j.jtice.2017.10.026.

[46] Kumar A, Mandal A, Singh N. Rice and wheat straw ashes: Characterization and modeling of pretilachlor sorption kinetics and adsorption isotherm. *J. Environ. Sci. Health B* 2019; 54: 303-312. https://doi.org/10.1080/03601234.2018.1561059

[47] Trivedi NS, Kharkar RA, Mandavgane SA. Use of wheat straw combustion residues for removal of chlorinated herbicide (2,4-dichlorophenoxyacetic acid). *Waste Biomass Valor.* 2019; 10: 1323-1331. https://doi.org/10.1007/s12649-017-0134-4

[48] Đokić-Stojanović DR, Todorović ZB, Troter DZ, Stamenković OS, Veselinović LjM, Zdujić MV, Manojlović DD, Veljković VB. Triethanolamine as an efficient cosolvent for biodiesel production by CaO-catalyzed sunflower oil ethanolysis: An optimization study. *Hem. Ind.* 2019; 73: 351-362.https://doi.org/10.2298/HEMIND190822033D

[49] Stanković M, Krstić J, Gabrovska M, Radonjić V, Nikolova D, Lončarević D, Jovanović D. Supported nickel-based catalysts for partial hydrogenation of edible oils. In: *New Advances in Hydrogenation Processes - Fundamentals and Applications*. IntechOpen; 2017: https://dx.doi.org/doi.org/10.5772/66967, https://www.intechopen.com/chapters/53666

[50] Rouquerol F, Rouquerol J, Sing K. *Adsorption by Powders and Porous Solids, Principles, Methodology and Applications*. London, Academic Press; 1999.

[51] Dubinin MM. *Progress in Surface and Membrane Science.* New York, Academic Press; 1975.

[52] Barrett EP, Joyner LG, Halenda PP. The determination of pore volume and area distributions in porous substances. I. Computations from nitrogen isotherms. *J. Am. Chem. Soc.* 1951; 73: 373-380.

[53] Lecloux A, Pirard JP. The importance of standard isotherms in the analysis of adsorption isotherms for determining the porous texture of solids. *J Colloid Interface. Sci*. 1979; 70: 265-281.

[54] Veličković AV, Stamenković OS, Todorović ZB, Veljković VB. Application of the full factorial design to optimization of base-catalyzed sunflower oil ethanolysis. *Fuel* 2013; 104: 433-442. https://doi.org/10.1016/j.fuel.2012.08.015

[55] Vassilev SV, Vassileva CG, Song YC, Li WY, Feng J. Ash contents and ash forming elements of biomass and their significance for solid biofuel combustion. *Fuel* 2017; 208: 377-409. https://doi.org/10.1016/j.fuel.2017.07.036

[56] Singh B, Camps-Arbestain M, Lehmann J. Biochar: *A guide to analytical methods. Australia*, Clayton, Vic.: CSIRO Publishing; 2017.

[57] Clemente JS, Beauchemin S, Thibault Y, MacKinnon T, Smith D. Differentiating inorganics in biochars produced at commercial scale using principal component analysis. *ACS Omega 3* 2018, 6: 6931-6944. https://doi. org /10.1021/acsomega.8b00523

[58] Platonov AY, Evdokimov AN, Kurzin AV, Maiyorova HD. Solubility of Potassium Carbonate and Potassium Hydrocarbonate in Methanol. *J. Chem. Eng. Data.* 2002; 47: 1175-1176. https://doi/10.1021/je020012v

[59] Lôbo IP, Ferreira SLC, da Cruz RS. Biodiesel: quality parameters and analytical methods. *Quim. Nova* 2009; 32: 1596-1608. https://doi.org/10.1590/S0100-40422009000600044

[60] Lundstedt T, Seifert E, Abramo L, Thelin B, Nyström Å, Pettersen J, Bergman R. Experimental design and optimization. *Chemom. Intell. Lab. Syst.* 1998; 42: 3-40. https://doi.org/10.1016/S0169-7439(98)00065-3

[61] Anderson MJ. *Statistics Made Easy_ Blog.The DOE FAQ Alert.* 10 (6). http://www.statease.com/news/faqalert10-06.html (2020). Accessed January 8, 2020.
[62] Anderson MJ, Whitcomb PJ. RSM simplified: *Optimizing processes using response surface methods for design of experiments*. 2nd ed., New York, Productivity Press; 2005.
[63] Vaz MAB, Pacheco PS, Seidel E Jr, Ansuj AP. Classification of the coefficient of variation to variables in beef cattle experiments. *Cienc. Rural.* 2017; 47: 1-4. http://dx.doi.org/10.1590/0103-8478cr20160946
[64] Saldaña-Roblesa A, Guerra-Sánchez R, Maldonado-Rubio MI, Peralta-Hernández JM. Optimization of the operating parameters using RSM for the Fenton oxidation process and adsorption on vegetal carbon of MO solutions. *J. Ind. Eng. Chem.* 2014; 20: 848-857. https://doi.org/10.1016/j.jiec.2013.06.015

SAŽETAK

Pepeo pšenične slame kao katalizator u proizvodnji biodizela

Ana Veličković[1], Jelena Avramović[1], Milan Kostić[2], Jugoslav B. Krstić[3], Olivera Stamenković[2] i Vlada B. Veljković[2,4]

[1]*Univerzitet u Prištini sa privremenim sedištem u Kosovskoj Mitrovici, Fakultet tehničkih nauka, Knjaza Miloša 7, 38220, Srbija*
[2]*Tehnološki fakultet, Univerzitet u Nišu, Bulevar oslobođenja, 16000 Leskovac, Srbija*
[3]*Institut za hemiju, tehnologiju i metalurgiju, Univerzitet u Beogradu, 11000 Beograd, Srbija*
[4]*Srpska Akademija nauka i umetnosti, Knez Mihailova 35, 11000 Beograd, Srbija*

(Naučni rad)

Pepeo pšenične slame (PPS) je korišćen kao katalizator u proizvodnji biodizela iz suncokretovog ulja. Karakterizacija katalizatora je izvršena primenom metoda temperaturski programiranom razgradnjom (temperature-programmed decomposition, TPDe), rentgenskom difrakcijom (X-ray diffraction, XRD), Hg porozimetrijom, N_2 fizisorpcijom i skenirajućom elektronskom mikrosopijom sa energo-disperzivnom spektrometrijom (scanning electron microscopy and energy dispersive X-ray spectroscopy, SEM-EDS). Reakcija metanolize istraživana je pri sledećim reakcionim uslovima: temperaturni opseg 55-65 °C; količina katalizatora 10-20 % (računato na masu ulja) i opseg molskog odnosa methanol : ulje 18 : 1 – 24 : 1. Optimizacija reakcionih uslova izvršena je metodologijom površine odziva u kombinaciji sa istorijskim eksperimentalnim planom. Maksimalni prinos metil estara masnih kiselina (MEMK) od 98,6 % postignut je pri sledećim optimalnim reakcionim uslovima: temperatura 60,3 °C, količina katalizatora 11,6 % (računato na masu ulja), molski odnos methanol : ulje 18,3 : 1 i vreme trajanja reakcije 124 min. Vrednosti koeficijenata determinacije (R^2 = 0,811, R^2_{pred} = 0,789, R^2_{adj} = 0,761) i srednjeg relativnog odstupanja (±10,6 %, 66 podataka) ukazali su na prihvatljivost i pouzdanost razvijenog modela. Sadržaj MEMK nakon 4 h reakcije pri optimalnim uslovima smanjen je na 37, 12 i 3 % nakon prve, druge i treće upotrebe katalizatora, redom.

Ključne reči: agro-otpad; metil estri masnih kiselina; karakterizacija katalizatora; modelovanje; optimizacija

Prediction of rubber vulcanization using an artificial neural network

Jelena D. Lubura, Predrag Kojić, Jelena Pavličević, Bojana Ikonić, Radovan Omorjan and Oskar Bera

University of Novi Sad, Faculty of Technology Novi Sad, Bulevar cara Lazara 1, 21000 Novi Sad, Serbia

Abstract

Determination of rubber rheological properties is indispensable in order to conduct efficient vulcanization process in rubber industry. The main goal of this study was development of an advanced artificial neural network (ANN) for quick and accurate vulcanization data prediction of commercially available rubber gum for tire production. The ANN was developed by using the platform for large-scale machine learning TensorFlow with the Sequential Keras-Dense layer model, in a Python framework. The ANN was trained and validated on previously determined experimental data of torque on time at five different temperatures, in the range from 140 to 180 °C, with a step of 10 °C. The activation functions, ReLU, Sigmoid and Softplus, were used to minimize error, where the ANN model with Softplus showed the most accurate predictions. Numbers of neurons and layers were varied, where the ANN with two layers and 20 neurons in each layer showed the most valid results. The proposed ANN was trained at temperatures of 140, 160 and 180 °C and used to predict the torque dependence on time for two test temperatures (150 and 170 °C). The obtained solutions were confirmed as accurate predictions, showing the mean absolute percentage error (MAPE) and mean squared error (MSE) values were less than 1.99 % and 0.032 $dN^2\,m^2$, respectively.

keywords: rubber curing; machine learning; rubber rheological properties.

Available on-line at the Journal web address: http://www.ache.org.rs/HI/

TECHNICAL PAPER

UDC: 675.92.028.3-036.4: 004.032.26

Hem. Ind. **75 (5)** 277-283 (2021)

1. INTRODUCTION

Natural rubber (NR) is an elastomeric polymer, widely used in preparation of rubber products. Vulcanization process of rubber has a crucial influence on the final product quality [1]. Prediction of rubber vulcanization data is particularly complicated due to the induction and reversion phenomena, which are presented in Figure 1. [2].

In general, the crosslink density of rubber compounds starts increasing slowly during the induction period, after which the main vulcanization reaction takes place with a significant increase of the crosslink density. Furthermore, the rubber blend at high temperatures (above 140 °C) can reach the torque maximum and start to decrease, causing weaker mechanical properties at longer curing times [3]. Studies dedicated to prediction of products of rubber vulcanization, mostly, neglected the reversion phenomenon, whereas the induction period and the main vulcanization kinetics were analysed separately [4–8]. In order to avoid complicated cross-linking kinetics, rubber rheological data can be successfully predicted using artificial neural networks (ANN). Neural networks are composed of basic units, termed neurons or nodes, arranged in layers. A neuron collects information provided by other neurons to which it is connected by weighted connections, where synaptic weights multiply the input information. Each neuron transforms its input into output response, where the transformation includes two steps. The first step is neuron activation, where it is computed as the weighted sum of its inputs, and the second step, where the activation is transformed to response by using a transfer function. If input is denoted as x_i and weight as w_i, then the activation computation is the sum of $w_i x_i$, and the output is obtained by applying a transfer function f [9]. Functions, which domains are defined by real numbers, can be used as transfer functions, where the most common are linear, logarithmic sigmoid and hyperbolic tangent functions

Corresponding author: Jelena D. Lubura, University of Novi Sad, Faculty of Technology Novi Sad, Bulevar cara Lazara 1, 21000 Novi Sad, Serbia
E-mail: jelenalubura@uns.ac.rs
Paper received: 11 May 2021; Paper accepted: 11 October 2021; Paper published: 30 October 2021.
https://doi.org/10.2298/HEMIND210511026L

CC BY NC ND

[10]. Nevertheless, by now there are limited ANN studies on rubber vulcanization and mostly, are aimed at tire design and tire curing equipment. In one study the ability of an ANN to evaluate variability of rheometric properties of rubber compounds from their formulations was investigated [11] and in another the optimum curing times of different rubber compounds were predicted [12].

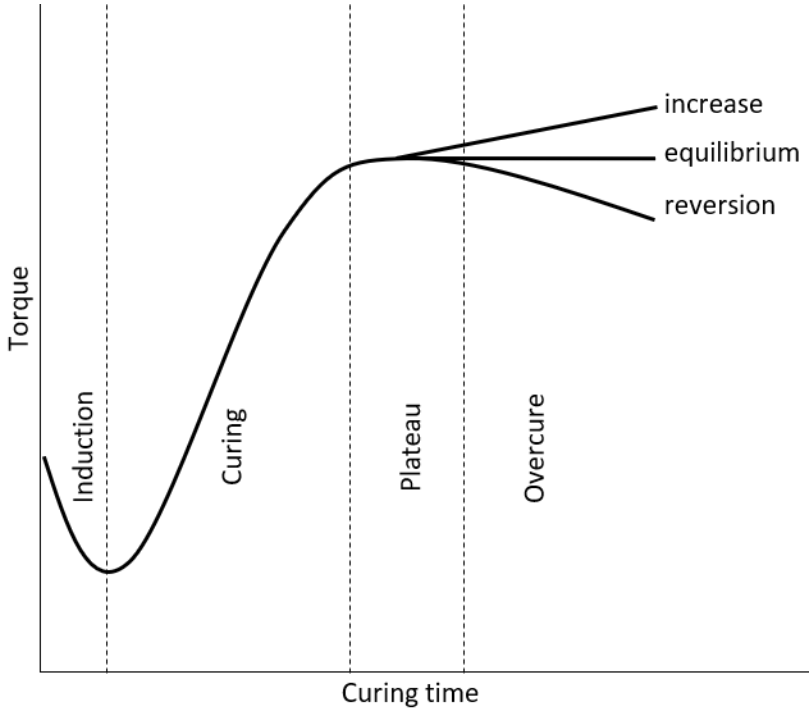

Figure 1. A typical vulcanization curve obtained from a rheometer

In this work, the focus was on ANN model development, able to predict the vulcanization data (torque versus time) for different temperatures. The significant contribution of this study is the built ANN model based on Python software that uses open-source license. Therefore, the rubber community (academic and industrial) can freely apply the introduced ANN code to predict vulcanization torque at different temperatures. The experimental rheometer data obtained previously [13] were used for training the ANN model. Furthermore, the number of neurons in the ANN architecture with one and two layers was varied to minimize the prediction error of the vulcanization torque. Additionally, three activation functions, ReLU, Sigmoid and Softplus, were examined to improve the ANN accuracy.

2. ARTIFICIAL NEURAL NETWORK DEVELOPMENT

Developing a predictive ANN model can be demanding due to nonlinear rubber vulcanization nature. The appropriate ANN architecture is the most challenging part in building the model and can be expected that ANN model with sufficient number of hidden layers may provide the adequate results, with the caution of overfitting [15]. Hidden layers consist of neurons, trained by a properly selected learning algorithm to acquire desired weight and activation function, which are considered as the key elements for the model. Regularly, three steps are followed in developing the ANN models: gathering large amounts of experimental vulcanization data, building and training the model, and model validation with testing [16].

The general ANN model, used in this study, consisted of input, hidden and output layers, as it is shown in Figure 2. [17,18]. The ANN has two neurons in the input layer (time and temperature), selected to predict the torque as a single neuron in the output layer.

The ANN model is built by using the Sequential Keras-Dense layer model of the TensorFlow [19]. Dense layer is commonly and frequently used, and it is a deeply connected neural network layer, in which the following operation is conducted [20]:

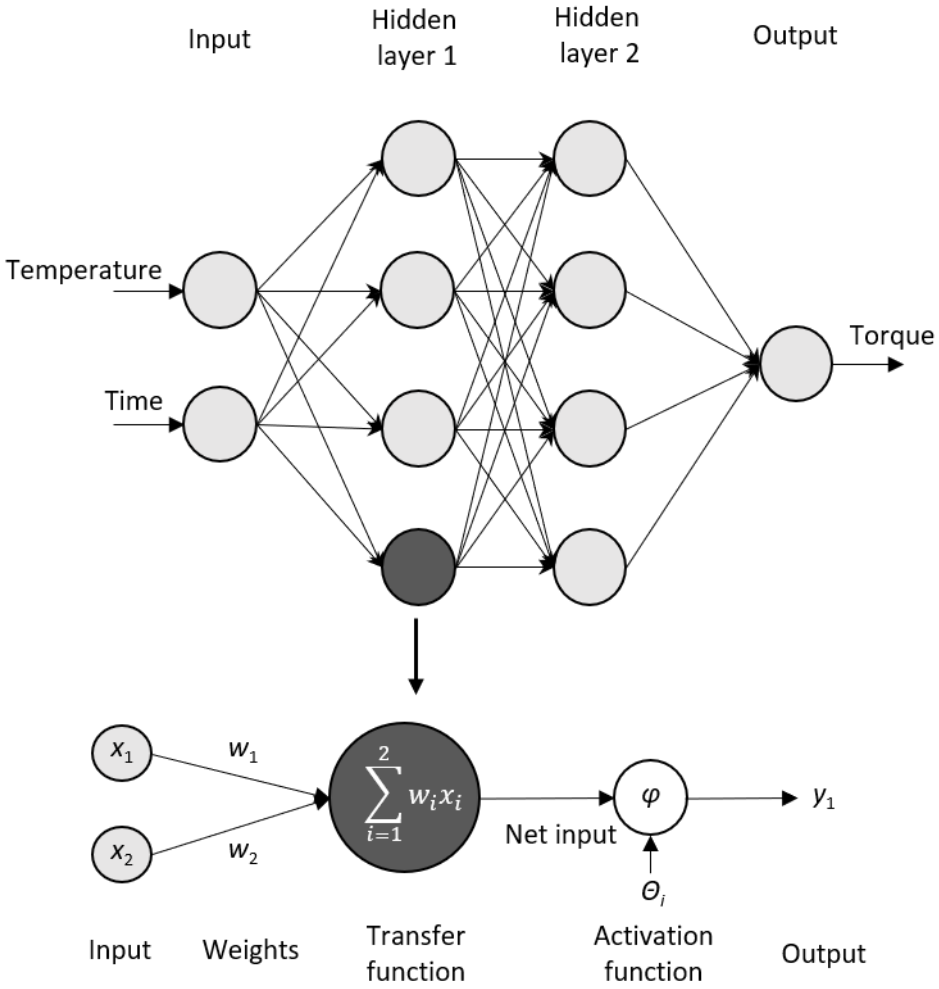

Figure 2. Example of the ANN architecture with two neurons in the input layer, two hidden layers with four neurons in each, and one neuron in the output layer

Output = activation (dot (input, kernel)) + bias (1)

where the *output* represents the output data, *activation* is the activation function, which is passed as the activation argument, *dot* is a numpy dot product of all inputs and their corresponding weights, *input* is the input data, *kernel* is the weight data created by the layer and *bias* is a bias vector created by the layer, which, in the Keras model, is assumed to learn its values [16].

In this research, three activation functions were used to obtain the model with minimal error: rectified linear unit (ReLU), Sigmoid and Softplus activation functions. The ReLU and Sigmoid functions are frequently used in the ANN models [21,22], while Softplus is a relatively novel differentiable function. The ReLU function is a linear function, and it is described as [23]:

$f(x) = 0$; for $x < 0$ $\quad f(x) = x$ for $x \geq 0$ (2)

The Sigmoid function is a non-linear, continuously differentiable, monotonic, S-shaped curve, and can be described as following [24]:

$$f(x) = \frac{1}{1+e^{-x}} \tag{3}$$

Softplus function is defined as [25]:

$f(x) = \ln (1+e^x)$ (4)

Significant parts of an ANN architecture are the loss function and optimizer. In this study, the mean squared error (MSE) was used as the loss function and for training, the model Adam optimizer in TensorFlow was tested. Adam

CC BY NC ND

optimizer is commonly used since it is computationally efficient, well suited for problems that are large in terms of data and appropriate for non-stationary objectives [26,27].

Number of training epochs can cause a problem in training neural networks, where too many epochs may lead to overfitting of the training dataset, whereas epoch lack results in an underfitted model [16]. In the present work, 50, 100 and 150 epochs were tested, and, in order to avoid underfitting and overfitting, number of epochs was set to 100.

The last step in ANN model building is its validation, where the extracted trained model of the training phase is split and is going through the validation phase using the testing dataset. Validation is conducted by using random 20 % of the dataset as a test, while the rest of data is used for training. There is a requirement for the training and validation loss function values to be near zero compared to the respective initial values, representing the sum of errors for each data point.

Additional model validation was performed by comparing the ANN predictions with the experimentally obtained curves, where the MAPE and MSE were used as statistical methods.

MAPE and MSE are calculated by eqs. (5) and (6), respectively:

$$\text{MAPE} = \frac{1}{n} \cdot \sum_{i=1}^{n} \left| \frac{A_i - F_i}{2} \right| \tag{5}$$

$$\text{MSE} = \frac{1}{n} \sum_{i=1}^{n} (A_i - F_i)^2 \tag{6}$$

where n is the number of fitted points, A_i is the actual value and F_i is the forecast value.

In the prediction phase, the developed ANN model was tested for three different activation functions to predict torque data at 150 and 170 °C. Furthermore, numbers of hidden layers and neurons were varied to increase the model accuracy and reliability. Lastly, the predicted vulcanization data are validated by the experimentally obtained curves.

3. RESULTS AND DISCUSSION

3. 1. ANN model

Developed ANN model was trained with rheometric data obtained at 140, 160 and 180 °C [13], where three activation functions (Softplus, ReLU, Sigmoid) and the number of neurons in hidden layer were varied. Firstly, the tests were run with 2, 3, 4 and 5 neurons in one hidden layer for each activation function, and the results of statistical error, as an elimination criterion (MAPE and MSE), are shown in Table 1.

Table 1. Prediction results for rheometric curves determined at 150 and 170 °C by using three different activation functions (ANN with one hidden layer)

Activation function		Softplus		ReLU		Sigmoid	
		Temperature, °C					
No of neurons	Statistical method	150	170	150	170	150	170
2	MAPE,%	5.102	8.293	4.014	5.344	6.423	8.662
	MSE, $dN^2\,m^2$	0.234	0.524	0.4	0.522	0.37	0.556
3	MAPE, %	5.328	9.298	4.584	4.827	6.07	8.133
	MSE, $dN^2\,m^2$	0.306	0.627	0.406	0.489	0.323	0.502
4	MAPE, *%*	3.099	4.84	3.493	4.826	6.078	8.419
	MSE, $dN^2\,m^2$	0.111	0.216	0.341	0.489	0.324	0.523
5	MAPE, *%*	5.772	8.123	5.14	7.921	5.598	8.988
	MSE, $dN^2\,m^2$	0.322	0.515	0.238	0.472	0.288	0.667
10	MAPE, *%*	2.351	3.441	6.601	8.146	5.886	8.551
	MSE, $dN^2\,m^2$	0.152	0.221	0.506	0.646	0.295	0.567
15	MAPE, *%*	2.421	4.1	2.85	3.691	5.566	8.446
	MSE, $dN^2\,m^2$	0.101	0.149	0.169	0.236	0.269	0.516
20	MAPE, *%*	7.834	4.282	3.793	11.646	5.192	8.985
	MSE, $dN^2\,m^2$	0.491	0.18	0.189	0.971	0.237	0.671

It can be seen that ANN models using Softplus and Sigmoid activation functions enabled the adequate rheometric curve predictions at 150 °C, while, at 170 °C, the error was high. Furthermore, the ANN model with ReLU activation function and one hidden layer with 2, 3, 4 or 5 neurons cannot predict torque dependence on time, at 150 and 170 °C. These results led to increased number of neurons (10, 15 and 20) in the hidden layer (Table 1). More than 20 neurons were not tested since high number of neurons can cause overfitting. The ANN model with ReLU activation function with higher numbers of neurons in the hidden layer resulted in lower MAPE and MSE values. However, the ANN prediction of vulcanization process at 170 °C is not satisfactory.

In order to increase the prediction accuracy, ANN model with two hidden layers was developed, and the results are shown in Table 2.

Table 2. Prediction results of rheometric curves determined at 150 and 170 °C for three different activation functions (ANN with two hidden layers containing the same number of neurons)

Activation function		Softplus		ReLU		Sigmoid	
		Temperature, °C					
No of neurons	Statistical method	150	170	150	170	150	170
2	MAPE, %	8.556	5.318	6.21	7.673	6.35	8.573
	MSE, $dN^2 m^2$	0.65	0.32	0.568	0.626	0.366	0.55
3	MAPE, %	7.745	5.031	3.57	4.809	6.029	7.789
	MSE, $dN^2 m^2$	0.631	0.275	0.215	0.393	0.307	0.485
4	MAPE, %	4.788	8.563	3.395	7.111	6.328	8.467
	MSE, $dN^2 m^2$	0.208	0.552	0.169	0.395	0.34	0.562
5	MAPE, %	1.423	2.849	5.19	9.389	5.427	8.938
	MSE, $dN^2 m^2$	0.042	0.109	0.26	0.641	0.261	0.636
10	MAPE, %	2.167	2.118	6.335	7.111	5.712	7.907
	MSE, $dN^2 m^2$	0.068	0.04	0.332	0.395	0.295	0.556
15	MAPE, %	1.627	1.462	7.228	5.738	5.115	8.446
	MSE, $dN^2 m^2$	0.033	0.025	0.469	0.29	0.24	0.515
20	MAPE, %	0.574	1.989	4.918	8.562	5.974	0.515
	MSE, $dN^2 m^2$	0.006	0.032	0.2	0.537	0.305	0.529

It can be observed that the increase in the number of neurons in two hidden layers led to a decrease in MAPE and MSE values. Additionally, the ANN with two hidden layers provided superior results in comparison with the ANN with one hidden layer. As the ANN model using Softplus activation function resulted in the most accurate prediction, it is discussed here in more details. It can be seen that the ANN model with two hidden layers containing 20 neurons provides MAPE lower than 1.99 % and MSE lower than 0.032 $dN^2 m^2$. Comparison of the experimental data and prediction of the developed ANN model is shown in Figure 2.

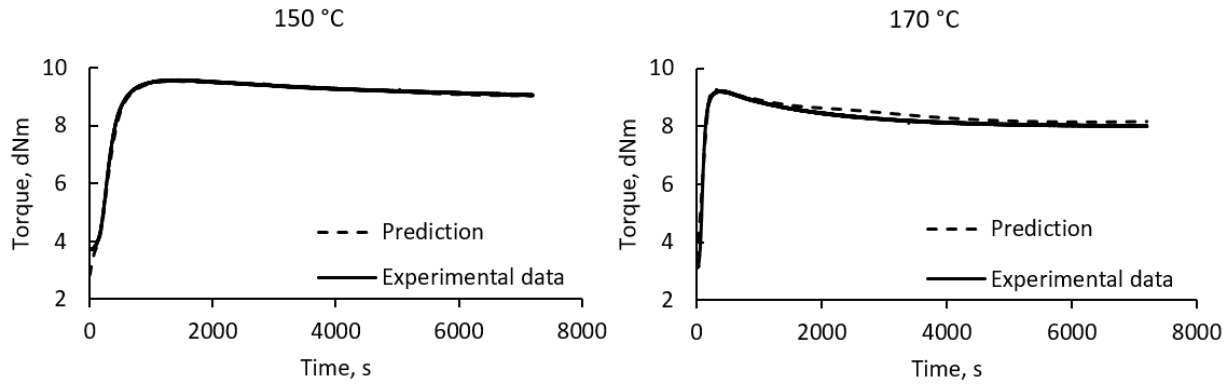

Figure 2. Experimental and predicted vulcanization data for 150 and 170 °C (experimental data are from [13])

The developed ANN model accurately predicted the torque dependences on time at test temperatures, enabling the fast and stable rheological prediction using only three rheological measurements, which is very important from the energy and cost savings aspects.

CC BY NC ND

4. CONCLUSIONS

The aim of this work was to develop the fast and accurate ANN model for rheological data prediction of NR/SBR rubber blend, using free software (Python), facilitating the vulcanization kinetics estimation and leading to time and cost savings, significant for the rubber community. The number of hidden layers, neurons in hidden layers and activation function (Softplus, ReLU, Sigmoid) were optimized in order to minimize the vulcanization data prediction error. The ANN model using Softplus as the activation function, containing 20 neurons in each of two hidden layers, resulted in the most accurate curing curve foresight. The predicted and experimental data were compared, and MAPE and MSE values were less than 1.99 % and 0.032 dN^2 m^2, respectively.

Acknowledgements: The authors would like to acknowledge the Ministry of Education, Science and Technological Development of the Republic of Serbia for the financial support, Project No. 451-03-9/2021-14/200134.

REFERENCES

[1] Ghoreishy MHR. A state-of-the-art review on the mathematical modeling and computer simulation of rubber vulcanization process. *Iran Polym J (English Ed).* 2016;25:89–109. https://doi.org/10.1007/s13726-015-0405-5

[2] Alwaan IM. Rheological characterization and modeling of vulcanization kinetics of natural rubber/starch blends. *J Appl Polym Sci*. 2018;135:27–9. https://doi.org/10.1002/app.46347

[3] Leroy E, Souid A, Deterre R. A continuous kinetic model of rubber vulcanization predicting induction and reversion. *Polym Test*. 2013;32:575–82. https://doi.org/10.1016/j.polymertesting.2013.01.003

[4] Erfanian MR, Anbarsooz M, Moghiman M. A three dimensional simulation of a rubber curing process considering variable order of reaction. *Appl Math Model.* 2016;40:8592–604. https://doi.org/10.1016/j.apm.2016.05.024

[5] Ghoreishy MHR, Rafei M, Naderi G. Optimizationofthevulcanizationprocessofathickrubber article using an advanced computer simulation technique. *Rubber Chem Technol.* 2012;85:576–89. https://doi.org/10.5254/rct.12.88917

[6] Khang TH, Ariff ZM. Vulcanization kinetics study of natural rubber compounds having different formulation variables. *J Therm Anal Calorim.* 2012;109:1545–53. https://doi.org/10.1007/s10973-011-1937-3

[7] Zhao L, Hu X. A variable reaction order model for prediction of curing kinetics of thermosetting polymers. *Polymer (Guildf).* 2007;48:6125–33. https://doi.org/10.1016/j.polymer.2007.07.067

[8] El Labban A, Mousseau P, Bailleul JL, Deterre R. Numerical natural rubber curing simulation, obtaining a controlled gradient of the state of cure in a thick-section part. *AIP Conf Proc.* 2007;907:921–6. https://doi.org/10.1063/1.2729631

[9] Wang B, Ma JH, Wu YP. Application of artificial neural network in prediction of abrasion of rubber composites. *Mater Des*. 2013;49:802–7. https://doi.org/10.1016/j.matdes.2013.01.047

[10] Yu Y, Adu K, Tashi N, Anokye P, Wang X, Ayidzoe MA. RMAF: Relu-Memristor-Like Activation Function for Deep Learning. *IEEE Access*. 2020;8:72727–41. https://doi.org/10.1109/ACCESS.2020.2987829

[11] Schwartz GA. Prediction of rheometric properties of compounds by using artificial neural networks. *Rubber Chem Technol.* 2001;74:116–23. https://doi.org/10.5254/1.3547632

[12] Karaağaç B, Inal M, Deniz V. Artificial neural network approach for predicting optimum cure time of rubber compounds. *Mater Des.* 2009;30:1685–90. https://doi.org/10.1016/j.matdes.2008.07.010

[13] Bera O, Pavličević J, Ikonić B, Lubura J, Govedarica D, Kojić P. A new approach for kinetic modeling and optimization of rubber molding. *Polym Eng Sci.* 2021;61:879–90. https://doi.org/10.1002/pen.25636

[14] Ghoreishy MHR, Rafei M, Naderi G. Optimization of the vulcanization process of a thick rubber article using an advanced computer simulation technique. *Rubber Chem Technol*. 2012;85:576–89. https://doi.org/10.5254/rct.12.88917

[15] Vijayabaskar V, Gupta R, Chakrabarti PP, Bhowmick AK. Prediction of properties of rubber by using artificial neural networks. *J Appl Polym Sci.* 2006;100:2227–37. https://doi.org/10.1002/app.22356

[16] Kazi MK, Eljack F, Mahdi E. Predictive ANN models for varying filler content for cotton fiber/PVC composites based on experimental load displacement curves. *Compos Struct.* 2020;254:112885. https://doi.org/10.1016/j.compstruct.2020.112885

[17] Elkatatny S. Real-Time Prediction of Rheological Parameters of KCl Water-Based Drilling Fluid Using Artificial Neural Networks. *Arab J Sci Eng.* 2017;42:1655–65. https://doi.org/10.1007/s13369-016-2409-7

[18] Saldaña M, Ayala L, Torres D, Toro N. Global sensitivity analyses of a neural networks model for a flotation circuit. *Hem Ind*. 2020;74:247–56. https://doi.org/10.2298/HEMIND20060523S

[19] Abadi M, Barham P, Chen J, Chen Z, Davis A, Dean J, Devin M, Ghemawat S, Irving G, Isard M, Kudlur M, Levenberg J, Monga R, Moore S, Murray DG, Steiner B, Tucker P, Vasudevan V, Warden P, Wicke M, Yu Y, Zheng X. TensorFlow: A system for large-scale machine learning, *Proceedings of the 12th USENIX Symposium on Operating Systems Design and Implementati*. November 2–4, 2016, Savannah, GA, USA, pp. 265-283.

[20] Sarang P. Artificial Neural Networks with TensorFlow 2. *Artif Neural Networks with TensorFlow 2.* 2021. https://doi.org/10.1007/978-1-4842-6150-7

[21] Bezabeh BB, Mengistu AD. The effects of multiple layers feed-forward neural network transfer function in digital based ethiopian soil classification and moisture prediction. *Int J Electr Comput Eng*. 2020;10:4073–9. https://doi.org/10.11591/ijece.v10i4. pp 4073-4079

[22] Dučić N, Ćojbašić Ž, Slavković R, Jordović B, Purenović J. Optimizacija hemijskog sastava u proizvodnji flotacijskih kugli zasnovana na inteligentnoj softverskoj detekciji. *Hem Ind.* 2016;70:603–12. https://doi.org/10.2298/HEMIND150715068D

[23] Lecun Y, Bengio Y, Hinton G. Deep learning. *Nature.* 2015;521:436–44. https://doi.org/10.1038/nature14539

[24] Nasr MS, Moustafa MAE, Seif HAE, El Kobrosy G. Application of artificial neural network (ANN) for the prediction of EL-AGAMY wastewater treatment plant performance-EGYPT. *Alexandria Eng J*. 2012;51:37–43. https://doi.org/10.1016/j.aej.2012.07.005

[25] Chasiotis VK, Tzempelikos DA, Filios AE, Moustris KP. Artificial neural network modelling of moisture content evolution for convective drying of cylindrical quince slices. *Comput Electron Agric.* 2020;172:105074. https://doi.org/10.1016/j.compag.2019.105074

[26] Park S, Park H. ANN Based Intrusion Detection Model. vol. 927. *Springer International Publishing*.; 2019. https://doi.org/10.1007/978-3-030-15035-8_40

[27] Ramalingam V V, Ragavendran R. Prediction of liver disease using artificial neural network with adam optimizer. *J Crit Rev*. 2020;7:1287–92. https://doi.org/10.31838/jcr.07.17.164

SAŽETAK

Predviđanje vulkanizacije gume korišćenjem veštačke neuronske mreže

Jelena D. Lubura, Predrag Kojić, Jelena Pavličević, Bojana Ikonić, Radovan Omorjan i Oskar Bera

Univerzitet u Novom Sadu, Tehnološki fakultet Novi Sad, Bulevar cara Lazara 1, 21000 Novi Sad, Srbija

(Stručni rad)

Za sprovođenje efikasnog procesa vulkanizacije u gumarskoj industriji neophodni su pouzdani reološki rezultati umrežavanja kaučukovih smeša. Stoga, osnovni cilj ovog rada bio je razvoj napredne veštačke neuronske mreže (engl. *artificial neural network*, ANN) za brzo i tačno predviđanje vulkanizacije komercijalno dostupne elastomerne smeše za dobijanje gumenih proizvoda. ANN je trenirana na prethodno određenim eksperimentalnim podacima obrtnog momenta u zavisnosti od vremena na pet različitih temperatura, u temperaturnom opsegu od 140 do 180 °C, sa korakom od 10 °C. ANN model je razvijen pomoću platforme za mašinsko učenje *TensorFlow* primenom *Keras* modela i programskog jezika Pajton (*Python*), gde su model i optimizator bili sekvencijalni model i adam, redom. Sledeće aktivacione funkcije: *ReLU*, sigmoidna i *Softplus*, korišćene su za minimizaciju greške, gde je ANN model sa *Softplus* funkcijom pokazao najtačnije rezultate predviđanja. Varirani su brojevi neurona i slojeva, gde je ANN model sa dva sloja, i 20 neurona u svakom sloju, dao najbolje rezultate. Predloženi ANN model je treniran na podacima dobijenim na temperaturama od 140, 160 i 180 °C, a zatim je korišćen za predviđanje zavisnosti obrtnog momenta od vremena za dve preostale temperature vulkanizacije u datom eksperimentalnom setu (150 i 170 °C). Dobijena rešenja su potvrđena kao tačna predviđanja upotrebom različitih numeričkih metoda, za sve ispitivane temperature, gde su vrednosti srednje apsolutno procentualno odstupanje (*engl*. mean absolute percentage error MAPE) i srednje kvadratno odstupanje (*engl*. mean squared error MSE) manje od 1,99% i 0,032 $dN^2\,m^2$, redom.

Ključne reči: umrežavanje gume; mašinsko učenje; reološka svojstva gume

CC BY NC ND

Extraction of ammonium nickel sulfate hexahydrate by hydrometallurgical process from the hyperaccumulating plant *Odontarrhena muralis* – case study from Serbia

Branislav Marković[1], Dragana Ranđelović[1], Gvozden Jovanović[1], Gordana Tomović[2], Ksenija Jakovljević[2], Tomica Mišljenović[2] and Miroslav Sokić[1]

[1]*Institute for Technology of Nuclear and Other Mineral Raw Materials, Franchet d'Esperey Boulevard 86, Belgrade, Serbia*
[2]*Institute of Botany and Botanical Garden, Faculty of Biology, University of Belgrade, Takovska 43, Belgrade, Serbia*

Abstract

Phytomining is a new promising technique that is based on using hyperaccumulating plants which biomass is utilized as a bio-ore for metal extraction. The Ni-hyperaccumulating species *Odontarrhena muralis* is widely distributed on ultramafic soils in Serbia, and could be a promising candidate for Ni agromining. In the present study, efficiency of a hydrometallurgical process for Ni recovery using biomass of *O. muralis* wild population through the synthesis of Ni salts from plant ash in the form of ammonium nickel sulfate hexahydrate, $Ni(NH_4)_2(SO_4)_2\ 6H_2O$ – (ANSH) was assessed. The average Ni content in the plant from ultramafic sites in West Serbia was up to 3.300 g kg^{-1}. The mass yield of ANSH crystals from the crude ash was ~12 % with the average purity of 73 % were obtained. By optimizing the purification process before precipitation of ANSH crystals, it is possible to obtain salt crystals of higher purity, which increases the economic profitability of this process. The results of this preliminary study on wild population of *O. muralis* show the increased potential for implementation of phytomining practices as an alternative way of Ni extraction on ultramafic sites in Serbia.

keywords: phytomining, bio-ore, leaching, nickel extraction.

Available on-line at the Journal web address: http://www.ache.org.rs/HI/

ORIGINAL SCIENTIFIC PAPER

UDC: 351.823:669.243:669.162.1

Hem. Ind. **75 (5)** 285-296 (2021)

1. INTRODUCTION

One of the main consequences of development and increasingly intensive anthropogenic activities is the generation of vast quantities of waste, often containing significant concentrations of potentially toxic elements (*e.g*. heavy metals). At the same time, intensive mining significantly depletes existing ore reserves, making the ores more expensive to extract and process. Therefore, in recent decades, new techniques have been developed that allow recycling of metal(oid)s, *i.e*. extraction from waste materials or from substrates with concentrations of metals or their compounds not sufficient for economically acceptable mining. One such technique is phytomining, in which selected hyperaccumulating plants are grown on a metal-bearing substrate with the aim of concentrating high amounts of the metal(oid)s in the biomass [1]. After the biomass is harvested, it is used as a bio-ore for metal(oid)s extraction. This process is similar to phytoextraction, with the difference that the biomass obtained by classical phytoextraction is treated as waste, while in the process of phytomining, it is a raw material for the recovery of metals or their compounds [2]. Hyperaccumulator plant species are those capable of accumulating metal(oid)s in the aboveground tissues at concentrations 100 – 1000-fold higher than in "normal" plants and higher than the threshold specifically proposed for most potentially toxic elements [3]. Hyperaccumulation of metal(oid)s is a rather unusual and rare phenomenon that has been described in about 700 vascular plants [4]. Most of these species hyperaccumulate Ni, almost exclusively on ultramafic soils, which are uninhabitable for many plant species due to the soil specific physical and chemical properties. The largest ultramafic areas in Europe are

Corresponding author: Branislav Marković, Institute for Technology of Nuclear and Other Mineral Raw Materials, Franchet d'Esperey Boulevard 86, Belgrade, Serbia
E-mail: b.markovic@itnms.ac.rs
Paper received: o1 July 2021; Paper accepted: 23 October 2021; Paper published: 1 November 2021.
https://doi.org/10.2298/HEMIND210701027M

CC BY NC ND

located in the Balkans, as large blocks or smaller outcrops [5] with significant representation in West and South-West Serbia. To be considered a hyperaccumulator of Ni, a plant has to contain more than 1.00 g kg^{-1} Ni in the dry matter of the aboveground tissues when growing in its natural habitat [3]. The largest number of Ni hyperaccumulators has been found in the genus *Odontarrhena* C. A. Mey ex Ledeb. (syn. *Alyssum* L. pro parte, sect. *Odontarrhena* (Meyer) Koch). One hyperaccumulator plant species belonging to this genus is *Odontarrhena muralis* (Waldst. & Kit.) Endl. (syn. *Alyssum murale* L.), which has been shown to accumulate up to 20.000 g Ni per kg dry weight [1]. Nickel concentrations of up to 2.926 g kg^{-1} in roots, 6.793 g kg^{-1} in shoots and 13.160 g kg^{-1} in leaves of *O. muralis* were found at different ultramafic sites in Serbia [6].

Ash from the plant combustion can be regarded as a bio-ore from which Ni or its products can be obtained either by pyrometallurgical or hydrometallurgical means. Li and co-workers have explored the pyrometallurgical extraction of metallic Ni by feeding biomass or ash directly into a smelter [7], while the hydrometallurgical extraction of metallic Ni can be performed from a leachate solution [8,9]. Not only metallic Ni, but also its various compounds can be recovered from plant ash, such as Lewis acid catalysts [10,11] or various Ni salts (ammonium nickel sulfate hexahydrate [12], nickel sulfide [13] or nickel hydroxide [14]). However, precipitation of Ni by direct leaching using water proved to be ineffective due to complexation of Ni with stronger ligands [15]. Ultimately, biomass ashing has shown promising results provoking various research studies related to optimization the ashing temperature, leaching agents, stirring rate, acid concentration, and other operating parameters towards more economically feasible and environmentally sustainable solutions [16,17].

After effective leaching, once an aqueous solution of $NiSO_4$ is obtained in sufficient concentration and purity, Ni products can be obtained in numerous forms, starting with $NiSO_4$ itself. With the addition of ammonium sulfate ($(NH_4)_2SO_4$) to the solution, ammonium nickel sulfate hexahydrate can be obtained, or nickel hydroxide $Ni(OH)_2$ can be precipitated by a suitable base such as MgO, NaOH or K_2CO_3. In addition, nickel hydroxide can be used as a final product or converted into nickel sulfamate ($Ni(NH_2SO_3)_2$), which is used for nickel electroplating, or it can be converted into nickel citrate ($Ni_3(C_6H_5O_7)_2$) using citric acid ($C_6H_8O_7$). Taking into account that all these Ni products must be of the highest purity (above 98 %) to be considered commercially viable, ammonium nickel sulfate hexahydrate, $Ni(NH_4)_2(SO_4)_2{\times}6H_2O$ – (ANSH) is a suitable Ni electroplating salt that can be obtained as a hydrometallurgical upgrade of Ni resulting from the phytomining process [18,19]. As grades of global Ni ore reserves continue to decline, the last decade has seen a shift from high-grade, low-volume ores to low-grade, high-volume ores. This decline has led to even greater volumes of waste produced by the mining industry, creating larger areas in need of remediation [20]. Bio-ores such as plant ash have a higher Ni concentration then common lateritic ores and do not contain Fe and Mg silicates, which are present in the soil matrix and could increase the cost of metal extraction. This fact shows a double benefit of phytomining; not only it helps in the remediation of waste contaminated soil, but it also produces higher-grade Ni bio-ores [21]. Unfortunately, despite the scientific validation of phytomining, the mining industry has not conducted testing beyond the pilot scale required to prove viability of this process in "real life". New research trends in the field of phytomining are moving toward more specifically designated studies to field conditions and valorization of bio-ores in terms of profit and environmental safety [22,23].

Several long-term studies have been conducted to optimize agronomic techniques for *Odontarrhena* species cultivation and Ni extraction from the low-productive ultramafic soils [24–26]. Mineral fertilizers (N, P, K) were found to be the most efficient, although significant results were also obtained with co-cropping and manure application [27–29]. Large variability of Ni concentrations in plant organs of *Odontarrhena* spp. clearly indicates that substrate properties (pH, amount of organic matter, water capacity, *etc.*) are important factors for development of these species [30]. Genetic structure of local populations also affects greatly the amount of Ni extracted from the soil. In view of this, it is of particular importance to conduct experiments at the local level to assess the potential for efficient metal recovery from native populations. Development of a customized process of *O. muralis* cultivation, biomass collection, and Ni extraction could lead to a sustainable and environmentally friendly methodology for Ni extraction from low-productive ultramafic outcrops in Serbia. This study aimed to test the efficiency of a hydrometallurgical process for Ni recovery from wild population of *Odontarrhena muralis* biomass through synthesis of Ni salts in the form of ammonium nickel sulfate hexahydrate, $Ni(NH_4)_2(SO_4)_2{\times}6H_2O$ – (ANSH) from the plant ash. This study represents a preliminary attempt to develop a method for Ni phytoextraction from hyperaccumulating plant populations in Serbia.

2. EXPERIMENTAL

Aboveground biomass of *O. muralis* was collected during the flowering phase in July 2019 at an ultramafic site in West Serbia (Mt Maljen, Tometino polje). The plant material was separated into leaves (OML), stems (OMS), and flowers (OMF), as well as the rest of the whole plant biomass and air-dried. The elemental composition of the plant material, ash, effluents, and leachates was analyzed by atomic absorption spectrometry (PinAAcle 900T PerkinElmer, Inc, Norwalk, CT, USA) with three replicates. Chemical elements of interest in this study were: Ni (as the only valorizing element), K, Ca (elements present in the plant that may interfere with the Ni extraction), Fe, and Mg (elements that may compete with Ni and reduce the purity of the final products). To determine contents of these elements in the plant biomass, the samples were priorly dissolved using the nitric acid-perchloric acid digestion method [31], and the inorganic elements (Ni, Ca, Mg, Fe, and K) were determined directly from the resulting solution. However, for determination of the Ni content in ash samples, the acid digestion method using aqua regia was applied [32], while for the remaining elements (Ca, Mg, Fe, and K), an alkali digesting method using HF+$HClO_4$ followed by H_2O+HCl dissolution was used [33]. For liquid samples such as effluents and leachates, the elemental content was determined directly by atomic absorption spectrometry. Standard Carl Roth solutions were used to calibrate the absorption curves for all sample types and elements. Apple leaf standard reference material NIST 1515 was used to verify the accuracy of the method.

Following the procedure developed by Zhang *et al.* [13] for more efficient extraction of Ni, the air-dried biomass was burned at 550 °C for 4 h. Potassium was removed from the ash by washing, which was repeated once with deionized water at a solid-liquid ratio of 1:4 for a period of 15 min using hand agitation. After washing, leaching of Ni from the ash was carried out using 2 M sulfuric acid (96 % *p.a.* Lachner, Czech Republic) heated to 95 °C with a solid-liquid mass ratio of ash to the acid of 1:9. Before crystallization of ANSH from the leachate, a two-step purification was performed to remove Fe and Mg. In the first step, $Ca(OH)_2$ (*p.a.* Sigma-Aldrich Chemie GmbH, Germany) was added at the concentration of 10 % to the leachate for neutralization and Fe removal. In the second step, NaF (p.a. Sigma-Aldrich Chemie GmbH, Germany) was added in excess of 10 % to remove Mg from the leachate. After each purification step, the leachate was vacuum filtered. Finally, to crystallize ANSH from the purified leachate, $(NH_4)_2SO_4$ (*p.a.* Merck, Germany) was added in excess of 20 %, and the solution was heated to 60°C to dissolve all salts. To increase the cooling and to crystallize higher amounts of ANSH, the solution was stored overnight at 4 °C.

Analysis of ANSH crystals and the solution after crystallization was performed by inductively coupled plasma optical emission spectrometry ICP-OES (Spectro Genesis, USA), using Smart Analyzer Vision Software. All chemical analyses were performed using three replicates.

Mineral phase composition of the samples was determined by using X-ray diffraction (XRD). XRD patterns were obtained on an automated diffractometer (PHILIPS PW-1710, Eindhoven, The Netherlands) using a Cu tube operated at 40 kV and 30 mA. The instrument was equipped with a diffracted beam curved graphite monochromator and a Xe-filled proportional counter. Diffraction data were collected in the 2 h Bragg angle range from 4 to 65°, counting for 1 s (qualitative identification) at every 0.02° step. Divergence and receiving slits were fixed at 1 and 0.1, respectively. All XRD measurements were performed at room temperature in a stationary sample holder.

Scanning electron microscopy (SEM) analyses were performed using a JEOL JSM–6610LV scanning electron microscope (JEOL Inc., USA) equipped with an INCA energy–dispersive X–ray analysis unit (EDS). An acceleration voltage of 20 kV was used. The analyzed samples were coated with a fine layer of gold dust to be visible under the microscope.

3. RESULTS AND DISCUSSION

3. 1. Chemical analyses of dry plant biomass and raw ash

Chemical compositions of the leaves (OML), stems (OMS), and flowers (OMF) of *O. murale* are shown in Table 1, as well as chemical compositions of the total aboveground plant biomass and the ash produced during combustion. According to the results, the highest Ni concentration was found in the leaves of *O. muralis*, which is in agreement with the results of other authors [34,35].

CC BY NC ND

Table 1. Element contents in stems (OMS), leaves (OML), flowers (OMF), total aboveground plant biomass (OM) and raw ash (RA)

Sample	Content, g kg^{-1}				
	Ca	Fe	K	Mg	Ni
OMS	5.968 ± 0.0231	n.d.*	11.104 ± 0.0304	1.612 ± 0.0147	1.003 ± 0.0112
OML	23.901 ±0.00666	0.0987 ±0.0038	11.326 ± 0.0119	4.410 ± 0.0103	4.790 ±0.0040
OMF	1.710 ± 0.0116	0.102 ±0.0036	17.995 ± 0.0142	4.020 ± 0.00351	2.980 ±0.00557
OM	12.923 ± 0.0135	0.102 ±0.0036	13.609 ± 0.0536	32.908 ± 0.0145	3.115 ± 0.0483
RA	159.075 ± 0.0512	2.092 ± 0.0258	163.034 ± 0.0331	35.926 ± 0.0234	30.120 ± 0.0429

*n.d.- non determined below threshold of 0.0005

The initial aboveground plant biomass of ~610 g (OM) was reduced to 45 g of raw ash (RA) during combustion, which means that ~93 % of the plant mass was burned. As shown in Table 1, the Ni content in ash is about 10-fold higher than that in the plant dry matter, which is consistent with literature data [16].

XRD analysis of the aboveground plant biomass (OM), shown in Figure 1, revealed the presence of the following mineral phases: bunsenite (NiO), aranite (K_2SO_4), alcite ($CaCO_3$), dolomite ($CaMg(CO_3)_2$), apatite ($Ca_5(PO_4)_3(OH,Cl,F)$), gorgeyite ($K_2Ca_5(SO_4)_6H_2O$), and fairchilde ($K_2Ca(CO_3)_2$). The predominant phases are aranite, calcite, and fairchilde, while bunsenite and apatite are present in lower amounts while gorgeyite is represented the least. Dolomite could be also present in the sample since its strongest diffraction peaks overleap with the peaks of the other present phases.

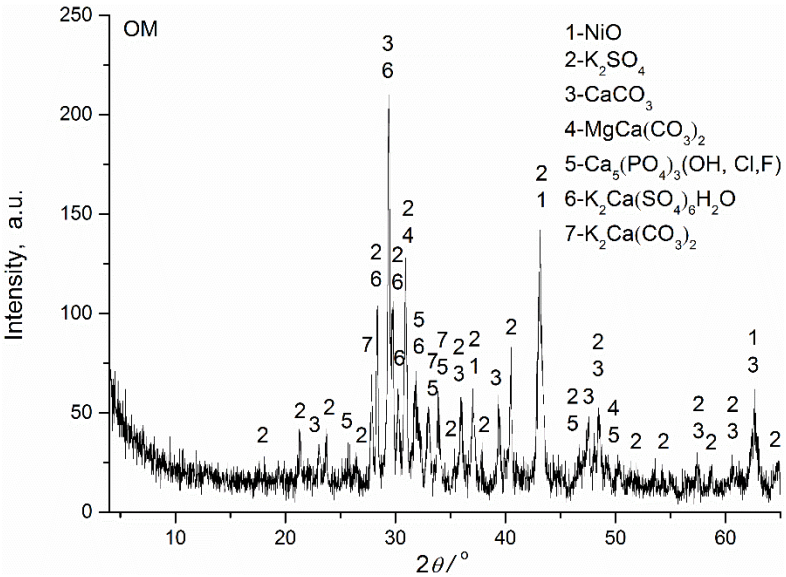

Figure 1. XRD analysis of the aboveground plant biomass (OM)

XRD analysis of raw ash (RA), presented in Figure 2, indicated the presence of the following mineral phases: calcite ($CaCO_3$), bunsenite (NiO), arkanite (K_2SO_4), apatite ($Ca_5(PO_4)_3(OH,Cl,F)$), sylvite (KCl), K_2CO_3, fairchilde ($K_2Ca(CO_3)_2$), panasqueiraite $CaMgPO_4(OH)$, and $K_2SO_4CaSO_4{\cdot}5H_2O$. The predominant phase is calcite, while somewhat less present phases are bunsenite, aranite, K_2CO_3, and fairchilde.

As the XRD patterns show (Figs. 1 and 2), mineral compositions before (OM) and after combustion (RA) are not significantly different, the only difference being concentrations (Table 1). In addition, the SEM-EDS analysis of the RA sample (Fig. 3) confirmed the presence of nickel at the high concentration of 3.87 wt %, validating the results obtained by the chemical analysis. Morphology of the analyzed ash surface is similar to those found in other studies [16].

Effects of combustion on raw ash properties were reported in literature, moving from a lab muffle furnace to a pilot-scale boiler in scale-up studies [17]. Although ash quantity and quality were altered due to differences in temperatures and residence times, after washing and acid leaching, these differences did not affect Ni recovery in the leachate. While it was shown that using a pilot or industrial furnace would be efficient for burning large amounts of biomass, further research should be conducted to investigate potential energy recovery from the biomass combustion.

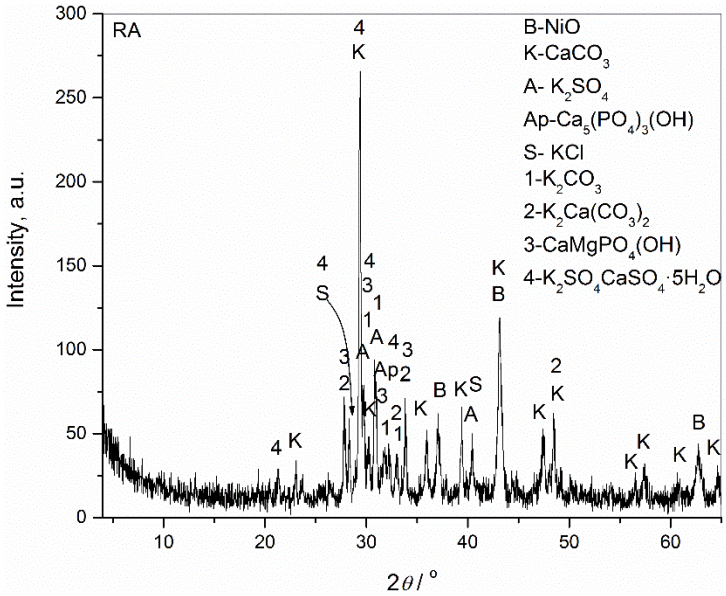

Figure 2. XRD analysis of raw ash (RA)

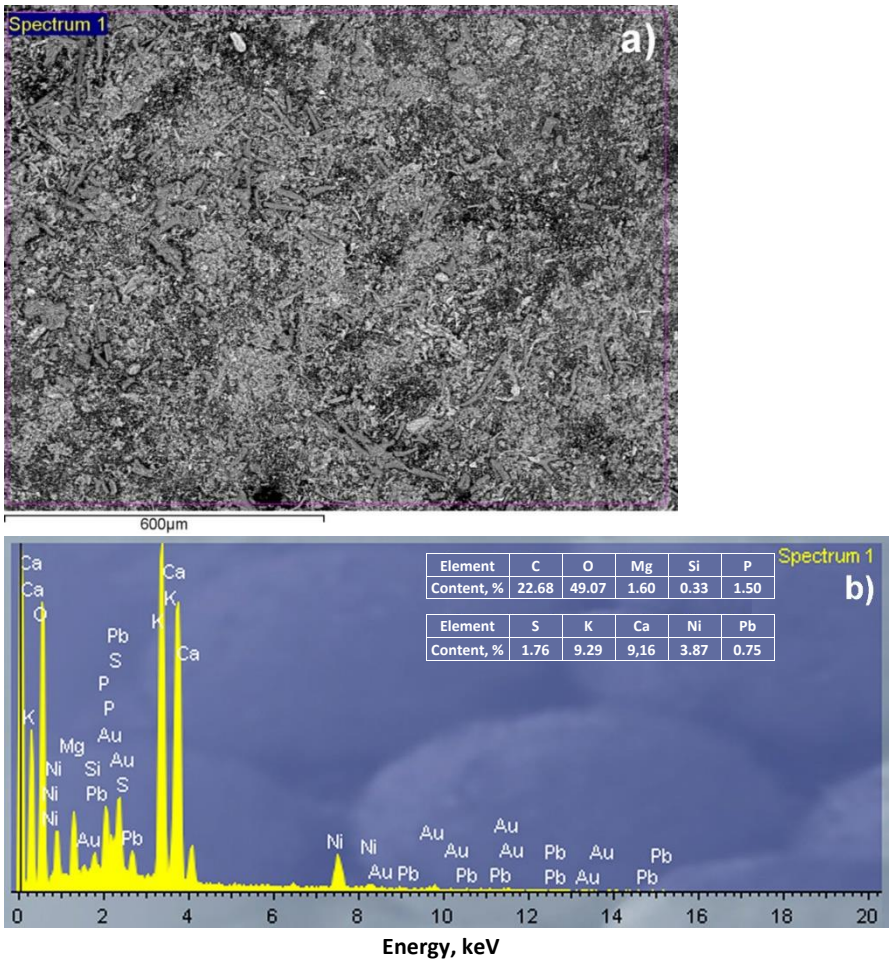

Figure 3. SEM-EDS analysis of the RA surface: (a) SEM micrograph, (b) the corresponding EDS spectrum together with numerical values

3. 2. Ash washing and potassium removal

Element concentrations determined in ash after the first and second washing step (WA-1 and WA-2) and in the corresponding effluents are shown in Table 2. The amount of water required for washing is determined by the dry

CC BY NC ND

weight of the ash, as it was found that the optimum solid-liquid ratio is 1:4. Potassium removal is most efficient at this ratio, as solid-liquid contact is reduced at higher solid phase values [13,18].

Table 2. Element contents in ash after the first (WA-1) and second washing step (WA-2) and in the corresponding effluents (EF-1 and EF-2, respectively)

Sample	Ca	Fe	K	Mg	Ni
			Content, g kg^{-1}		
WA-1	250 ± 42.6	2.420 ± 0.13	185 ± 13.5	57.5 ± 7.1	47.5 ± 5.3
WA-2	217 ± 28.3	2.220 ± 0.800	38.5 ± 3.6	48.7 ± 5.2	40 ± 6.9
			Content, mg dm^{-3}		
EF-1	11.0 ± 0.700	0.58 ± 0.050	27100 ± 285	11.7 ± 6.30	1.20 ± 0.100
EF-2	9.50 ± 0.120	0.230 ± 0.030	5670 ± 72	26.3 ± 8.90	0.700 ± 0.060

By comparing the data for RA (Table 1) and washed ash samples (Table 2), it can be noticed that concentrations of all elements in the ash increased upon first washing. This is due to the massive weight loss in the ash due to leaching of K_2CO_3, which is confirmed by a significant amount of potassium determined in the effluent WA-1 (Table 1). In specific, the weight loss after the first washing step was about 25 % after the first washing step and about further 10 % after the second washing step.

Expected reduction in concentrations of all investigated elements in the ashes is noted after the second washing step. Since most of potassium was removed during the first step, alkalinity of the effluent was lowered, allowing for the subsequent extraction of magnesium and calcium.

3. 3. Leaching and purification

According to a previously reported study [36], optimal parameters for leaching Ni from *O. muralis* ashes to obtain a yield of Ni in the leachate of 10.2 g dm^{-3} were: the temperature of 95°C in 1.9M sulfuric acid for 240 min at the solid-liquid ratio of 150 g dm^{-3}. This was confirmed by Zhang [13], who reported the temperature of 70°C as sufficient, but to avoid the use of concentrated acid, leaching at 95°C is more efficient. In addition to the indicated temperature, the optimum leaching conditions are an ash-to-acid solid-liquid mass ratio of 1:9, process duration of 2 h, and 2M sulfuric acid concentration [13]. Moreover, previous studies on the leaching kinetics of ashes of a hyperaccumulating plant *Alyssum murale* by sulfuric acid [37] showed that extraction of Ni was mainly affected by the temperature and acid concentration and that the extraction rate of all the elements analyzed (Ca, Fe, K, Mg, Mn, Ni, P) was neither limited nor controlled by external film diffusion.

After the second washing and drying, and before leaching, in the present work the solid-liquid ration of 1:9 mass ratio was adopted according to the procedure. During the leaching process, the Ni content in the ash decreased from ~40 to ~4 g kg^{-1}, as shown in Table 3.

Table 3. Element contents in washed ashes after leaching (SW), leachate before purification (L1), and leachate after purification (L2)

Sample	Ca	Fe	K	Mg	Ni
			Content, g kg^{-1}		
SW	132.0 ± 37.2	0.342 ± 0.020	1.32 ± 0.40	4.60 ± 2.10	3.99 ± 0.30
			Content, mg dm^{-3}		
L1	530 ± 25.8	262 ± 2.3	3430 ± 135	15200 ± 23.8	8500 ±35.7
L2	120 ± 17.3	174 ± 1.8	1580 ± 58.6	3960 ±74	5400 ± 44

XRD analysis of washed ashes prior leaching (WA-2) and washed ashes after leaching (SW), (Figs. 4 and 5, respectively) show that the phases present in the WA-2 sample are calcite ($CaCO_3$), and bunsenite (NiO), while in the SW sample only, the presence of gypsum $CaSO_4 \cdot 2H_2O$ is detected.

Furthermore, the XRD analysis together with the SEM-EDS investigation (Fig. 6) confirm that the residue Ni at the concentration of ~4 g kg^{-1} (Table 3), remained after leaching in the SW sample, is not chemically bound in the form of

NiO compound. Thus, we can assume that the remaining Ni is bound by a stronger ligand not dissoluble by sulfuric acid, dispersed in small undetectable amounts throughout the ash sample.

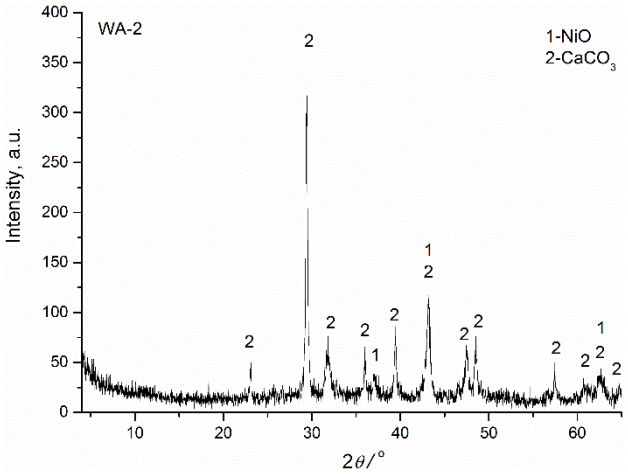

Figure 4. XRD analysis of washed ashes prior leaching (WA-2)

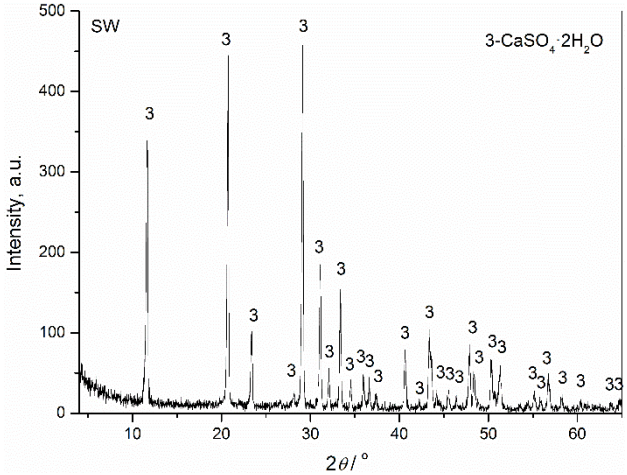

Figure 5. XRD analysis of washed ashes after leaching (SW)

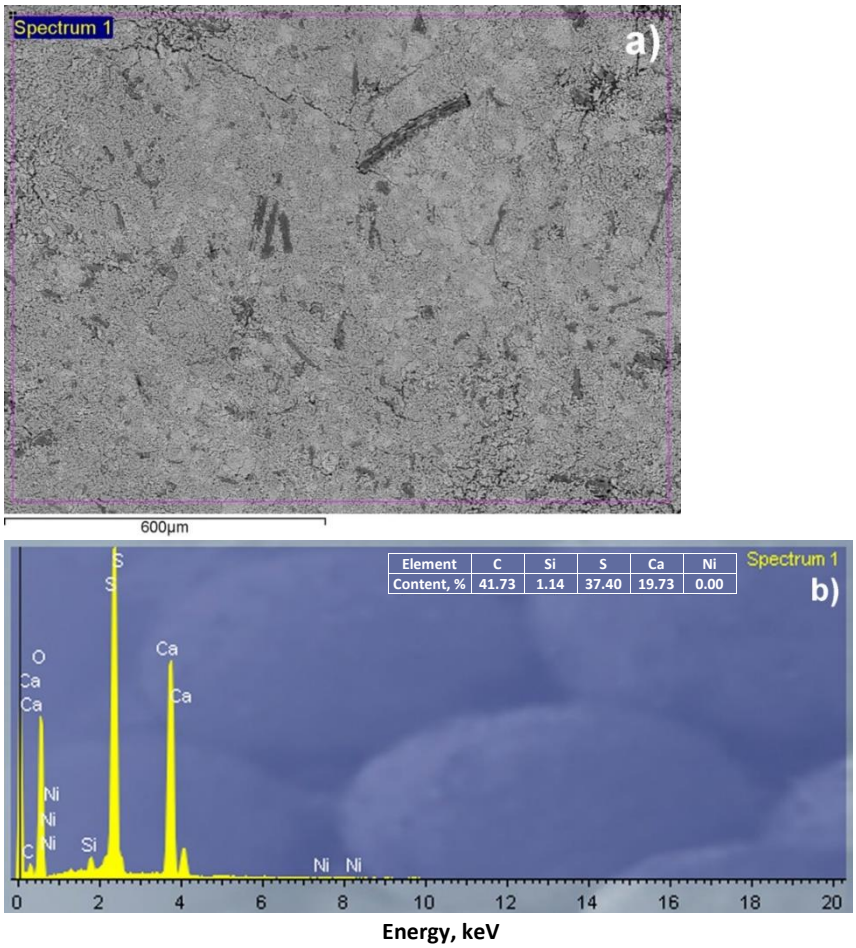

Figure 6. SEM-EDS analysis of the surface of washed ash after leaching: (a) SEM micrograph, (b) the corresponding EDS spectrum together with numerical values

After leaching and before crystallization of ANSH, the leachate had to be purified, which was carried out in two steps. In the first step, Fe was removed by precipitation in the form of $Fe(OH)_3$ due to its low solubility (1.5×10^{-15} g dm^{-3} [38]), according to the equation (1).

$$3Ca(OH)_2 + Fe_2(SO_4)_3 \rightarrow 2Fe(OH)_3 + 3CaSO_4 \quad (1)$$

It was shown in literature [16] that the precipitation by $Ca(OH)_2$ is significantly more efficient as compared to the use of NaOH used previously [36]. In addition, 10 % suspension of $Ca(OH)_2$ was recommended, as there is a risk of losing a significant amount of Ni trapped in the $CaSO_4$ precipitate when a 20 % suspension is used. As shown in Table 3, there was a decrease in Ni concentration from 8.50 to 5.40 g dm^{-3} after purification. This drop can infer that there is a small amount of Ni trapped in the $CaSO_4$ precipitate even when a 10 % suspension is used.

The next step of purification was the removal of Mg from the leachate since the presence of this element would inhibit ANSH crystallization by precipitation in the form of $MgNH_4PO_4$. As mentioned in the experimental section, this step was performed by adding NaF to the leachate resulting in the reaction (2).

$$MgSO_4 + 2NaF \rightarrow MgF_2 + Na_2SO_4 \quad (2)$$

Since the solubility of MgF_2 is lower than the solubility of NiF_2 (0.13 g kg^{-1} *vs.* 25.6 g kg^{-1} in water at 25 °C [39]), all Ni will remain in the leachate. NaF is added in excess of 10 % regarding the Mg content in the leachate before purification (L1, Table 3). However, the content of Mg in the obtained ANSH crystals (Table 4), suggests that the Mg removal from the leachate was not sufficient as compared to previous studies [16].

During MgF_2 precipitation according to equation (2), there is also CaF_2 precipitation, equation (3):

$$Ca^{2+} + 2NaF \rightarrow CaF_2 + 2Na^+ \quad (3)$$

Although the Mg concentration in the leachate is higher (Table 3), CaF_2 is precipitated first due to the lower solubility product (4.0×10^{-11} mol^3 dm^{-9} for CaF_2 and 6.4×10^{-9} mol^3 dm^{-9} for MgF_2 at 18-25 °C [38]). Therefore, when calculating the amount of NaF required to remove Mg from the leachate, the amount of present Ca has to be considered.

After purification, the leachate may be subjected to evaporation to increase the Ni concentration. However, over-evaporation should be avoided to prevent precipitation of various dissolved Ni salts (*e.g.* NiF_2, $NiSO_4$, $Ni(OH)_2$, *etc.*), already present in the leachate.

3. 4. Crystallization

To crystallize ANSH, ammonium sulfate $(NH_4)_2SO_4$ was added to the purified leachate in 20 % excess and the suspension was heated to 60 °C. The precipitation was carried out according to the equation:

$$NiSO_4 + (NH_4)_2SO_4 + 6H_2O \rightarrow Ni(NH_4)_2(SO_4)_2\times6H_2O \quad (4)$$

After completion of the reaction, the solution was cooled and left overnight to promote ANSH crystallization. Next, the ANSH crystals were vacuum filtered and dried. Recrystallization was performed after drying the salt crystals to increase the purity of ANSH (as suggested in literature [13]), since the solubility of ANSH in water is 175.0 g kg^{-1} at 60 °C while only 19.0 g kg^{-1} at 0 °C.

Chemical compositions of ANSH crystals and the solution after crystallization (SAC) are shown in Table 4.

Table 4. Chemical composition of ANSH crystals and the solution after crystallization (SAC)

Sample	As	Ca	Cd	Co	Cr	Cu	Fe	K
	Content, g kg^{-1}							
ANSH	<0.030	<0.010	<0.030	<0.010	0.017 ± 0.040	<0.010	0.350 ± 0.250	24.500 ±0. 540
	Content, mg dm^{-3}							
SAC	<0.03	<0.01	<0.03	<0.01	0.017	<0.01	0.359	24.9
	Mg	Mn	Na	Ni	P	Pb	Zn	
	Content, g kg^{-1}							
ANSH	20.90 ± 0.44	0.016 ± 0.004	0.060 ± 0.002	110.00 ± 1.04	0.340 ± 0.060	<0.010	0.970 ± 0.220	
	Content, mg dm^{-3}							
SAC	21.2	0.016	0.057	111	0.35	<0.01	0.99	

The purity of the acquired dried ANSH crystals weighing 5.2 ± 0.4 g was 73 % (Ni: 110.0 ± 1.04 g kg^{-1}). This is somewhat lower than purities reported in literature of 88.8 % (Ni: 132.0 ± 3.0 g kg^{-1}) [36] and 99.1 % (Ni: 149.0 ± 1.0 g kg^{-1}) [13].

The main reason for differences in purity is the insufficient removal of Mg during the purification step, which can be easily remedied by using a higher amount of NaF by taking into account the presence of Ca in the leachate.

3. 5. Feasibility of Ni phytomining by *O. muralis* in Serbia

Ultramafic areas represent natural sources of Ni, which concentration is often quite higher than the established limits [40, 41], but still below the grades suitable for conventional mining. Therefore, such areas are considered particularly favorable for the development of phytomining techniques. The largest ultramafic massifs in Europe are located in Serbia [42], where suitable areas could be selected to establish phytomining plots. A wide range of nickel concentrations has been recorded in the ultramafic soils of Serbia, *i.e*. from 0.750, up to 2.300 g kg^{-1} [43], generally mostly exceeding 1.000 g kg^{-1}. For example, a median Ni concentration from 7 ultramafic sites in Serbia was reported as 1.330 g kg^{-1} [44]. Even at small geographical scales, microedaphic factors can lead to significant differences in soil Ni concentrations and strongly influence the degree of Ni accumulation in some hyperaccumulating species [45]. Organic matter contents as well as the contents of macronutrients such as N, P, K, also greatly vary between the sites [43,44,46]. Therefore, appropriate agrochemical analyses are required before establishing phytomining plots. Long-term field trials in Albania [27] and studies in Austria and Greece [47] have demonstrated that phytomining could become an economically viable agricultural cropping system if the appropriate agronomic techniques are applied. However, these agronomic practices should be well adapted to regional conditions. For example, manure seems to be much less effective than inorganic fertilizers in acidic soils with low Ni mobility, while it is much more efficient in soils with high concentrations of available Ni [47]. Therefore, appropriate agronomic practices adapted to the present edaphic and climatic conditions could be proposed for selected agromining plots in Serbia after the initial examination of soil properties.

Based on the high phenotypic plasticity and Ni concentrations of up to 13.200 g kg^{-1} detected in its leaves [6], *O. muralis*, a native metallophyte widely distributed on ultramafic substrates in Serbia, could be a suitable candidate for Ni agromining. According to the results of field trials with *O. muralis* in Albania, the optimal annual Ni yield could reach up to 100 kg ha^{-1} [27], while in the first studies with the same species, conducted without fertilization, only 3 kg Ni ha^{-1} were harvested [24]. Apart from *O. muralis*, several other Ni hyperaccumulators are widely distributed in Serbia, including species of the genus *Noccaea*. Although species from this genus have lower biomass production than *O. muralis*, up to 30 kg Ni ha^{-1} was obtained in the biomass of *N. goesingensis* (Halácsy) F. K. Mey. in Austria [26]. As numerous populations of *N. kovatsii* (Heuff.) F. K. Mey. and *N. praecox* (Wulfen) F. K. Mey., phylogenetically closely related to *N. goesingensis*, have been detected in Serbia with Ni concentrations above 10.0 g kg^{-1} [44], the potential of these autochthonous species for Ni phytomining in Serbia could be also assessed.

Life Cycle Assessment (LCA) of Ni phytomining chain was conducted for *O. murale* in Albania, identifying opportunities for improvement and showing the overall low environmental impact of the whole process [48]. LCA showed that anti-erosion practices have to be taken into account, coupled with optimizations and improvements of the Ni-recovery process, especially in terms of processing generated effluents or solid residues from the synthesis of the ANSH salts. Moreover, the possibility of using heat generated by biomass combustion and returning certain by-products from the process to the field in order to improve soil fertility could reduce the costs and increase the added value of the whole phytomining process.

In the future, after the successful technological acquisition of high-purity ANSH crystals or another valuable Ni product, an economic feasibility study of Ni phytomining in Serbia should be conducted to assess the potential environmental impact. The preliminary results of this study reveal the potential for establishing sustainable Ni phytomining plots in Serbia using native Ni hyperaccumulating species *O. murale*, based on the experiences gained in the European network of agromining field sites [18].

5. CONCLUSION

The average Ni content in *O. muralis* populations from ultramafic sites in West Serbia was up to 3.300 g kg^{-1}, indicating hyperaccumulation potential and suitability for a successful Ni recovery. During combustion of the plant biomass, the weight was reduced for ~93 %, and the resulting ash was a suitable raw material for Ni extraction. After

CC BY NC ND

the leaching process, crude ash yielded ANSH crystals with purity of 73 %. The purity of the recovered crystals can be further increased by adjusting the Mg removal from the leachate during the purification process before crystal precipitation.

Results of this study show the potential for implementing phytomining practices in ultramafic areas in Serbia. Moreover, by optimizing the hydrometallurgical process of ANSH extraction, it is possible to obtain salt crystals of higher purity, which would increase the economic profitability of this process. In addition, it is possible to significantly increase the Ni yield by establishing cultivation plots, where appropriate agronomic methods could be implemented.

Acknowledgements: The authors are grateful to the Ministry of Education, Science and Technological Development of the Republic of Serbia (Contract numbers: 451-03-9/2021-14/200023 and 451-03-9/2021-14/200178) for the financial support for this investigation.

REFERENCES

[1] Chaney RL, Angle JS, Broadhurst CL, Peters CA, Tappero R V, Sparks DL. Improved understanding of hyperaccumulation yields commercial phytoextraction and phytomining technologies. *J Environ Qual*. 2007;36(5):1429-1443 https://doi.org/10.2134/jeq2006.0514

[2] Chaney RL, Baker AJM, Morel JL. The long road to developing agromining/phytomining. In: van der Ent A, Baker AJM, Echevarria G, Simonnot M-O, Morel JL, eds. Agromining: farming for metals. *Extracting unconventional resources using plants*. 2nd ed. Cham, Switzerland: Springer Nature; 2021:1-22 https://doi.org/10.1007/978-3-030-58904-2

[3] van der Ent A, Baker AJM, Reeves RD, Pollard AJ, Schat H. Hyperaccumulators of metal and metalloid trace elements: facts and fiction. *Plant Soil*. 2013;362(1):319-334 https://doi.org/10.1007/s11104-012-1287-3

[4] Reeves RD, Baker AJ, Jaffré T, Erskine PD, Echevarria G, van der Ent A. A global database for plants that hyperaccumulate metal and metalloid trace elements. *New Phytol*. 2018;218(2):407-411 https://doi.org/10.1111/nph.14907

[5] Stevanović V, Tan K, Iatrou G. Distribution of the endemic Balkan flora on serpentine I.–obligate serpentine endemics. *Plant Syst Evol*. 2003;242(1):149-170 https://doi.org/10.1007/s00606-003-0044-8

[6] umi AF, Mihailović N, Gajić BA, Niketić M, Tomović G. Comparative study of hyperaccumulation of nickel by *Alyssum murale* sl populations from the ultramafics of Serbia. *Polish J Environ Stud*. 2012;21(6):1855-1866

[7] Li Y-M, Chaney R, Brewer E, Roseberg R, Angle JS, Baker A, Reeves R, Nelkin J. Development of a technology for commercial phytoextraction of nickel: economic and technical considerations. *Plant Soil*. 2003;249(1):107-115 https://doi.org/10.1023/A:1022527330401

[8] Tennakone K, Senevirathna MKI, Kehelpannala KVW. Extraction of pure metallic nickel from ores and plants at Ussangoda, Sri Lanka. *J Natl Sci Found Sri Lanka*. 2007;35(4):245-250 https://doi.org/10.4038/jnsfsr.v35i4.1313

[9] Barbaroux R, Mercier G, Blais J-F, Morel J-L, Simonnot M-O. A new method for obtaining nickel metal from the hyperaccumulator plant *Alyssum murale*. *Sep Purif Technol*. 2011;83:57-65 https://doi.org/10.1016/j.seppur.2011.09.009

[10] Losfeld G, Escande V, Jaffré T, L'Huillier L, Grison C. The chemical exploitation of nickel phytoextraction: an environmental, ecologic and economic opportunity for New Caledonia. *Chemosphere*. 2012;89(7):907-910 https://doi.org/10.1016/j.chemosphere.2012.05.004

[11] Grison C, Escande V, Petit E, Garoux L, Boulanger C, Grison C. *Psychotria douarrei* and *Geissois pruinosa*, novel resources for the plant-based catalytic chemistry. *RSC Adv*. 2013;3(44):22340-22345 https://doi.org/10.1039/C3RA43995J

[12] Barbaroux R. Développement d'un procédé hydrométallurgique de récupération du nickel à partir de la plante hyperaccumulatrice Alyssum murale. Thesis. Quebec, Canada: University of Quebec, Institut national de la recherche scientifiqu; 2010 (in French) http://espace.inrs.ca/id/eprint/1765/

[13] Zhang X. Hydrometallurgical process for the valorization of nickel contained in hyperaccumulating plants. Thesis. Lorraine, France: Université de Lorraine; 2014 https://hal.univ-lorraine.fr/tel-01751083

[14] Vaughan J, Riggio J, Chen J, Peng H, Harris HH, van der Ent A. Characterisation and hydrometallurgical processing of nickel from tropical agromined bio-ore. *Hydrometallurgy*. 2017;169:346-355 https://doi.org/10.1016/j.hydromet.2017.01.012

[15] Guilpain M, Laubie B, Zhang X, Morel JL, Simonnot M-O. Speciation of nickel extracted from hyperaccumulator plants by water leaching. *Hydrometallurgy*. 2018;180:192-200 https://doi.org/10.1016/j.hydromet.2018.07.024

[16] Zhang X, Laubie B, Houzelot V, Plasari E, Echevarria G, Simonnot M-O. Increasing purity of ammonium nickel sulfate hexahydrate and production sustainability in a nickel phytomining process. *Chem Eng Res Des*. 2016;106:26-32 https://doi.org/10.1016/j.cherd.2015.12.009

[17] Houzelot V, Laubie B, Pontvianne S, Simonnot M-O. Effect of up-scaling on the quality of ashes obtained from hyperaccumulator biomass to recover Ni by agromining. *Chem Eng Res Des*. 2017;120:26-33 https://doi.org/10.1016/j.cherd.2017.02.002

[18] Kidd PS, Bani A, Benizri E, Gonnelli C, Hazotte C, Kisser J, Konstantinou M, Kuppens T, Kyrkas D, Laubie B. Developing sustainable agromining systems in agricultural ultramafic soils for nickel recovery. *Front Environ Sci*. 2018;6:44 https://doi.org/10.3389/fenvs.2018.00044

[19] Simonnot M-O, Vaughan J, Laubie B. Processing of bio-ore to products. In: van der Ent A, Echevarria G, Baker A, Morel J, eds. *Agromining: Farming for Metals*. Cham, Switzerland: Springer; 2018: 39-51 https://doi.org/10.1007/978-3-319-61899-9_3

[20] Bian Z, Miao X, Lei S, Chen S, Wang W, Struthers S. The challenges of reusing mining and mineral-processing wastes. *Science*. 2012; 337(6095):702-703 https://doi.org/10.1126/science.1224757

[21] van der Ent A, Baker AJM, Reeves RD, Chaney RL, Anderson CWN, Meech JA, Erskine PD, Simonnot M-O, Vaughan J, Morel JL, Echevarria G, Fogliani B, Rongliang Q, Mulligan DR. Agromining: farming for metals in the future? Environ Sci Technol. 2015;49:4773–4780 https://doi.org/10.1021/es506031u

[22] Sheoran V, Sheoran AS, Poonia P. Phytomining: A review. *Miner Eng*. 2009;22(12):1007-1019 https://doi.org/10.1016/j.mineng.2009.04.001

[23] Li C, Ji X, Luo X. Visualizing hotspots and future trends in phytomining research through scientometrics. *Sustainability*. 2020;12(11):4593 https://doi.org/10.3390/su12114593

[24] Bani A, Echevarria G, Sulçe S, Morel JL, Mullai A. In-situ phytoextraction of Ni by a native population of *Alyssum murale* on an ultramafic site (Albania). *Plant Soil*. 2007;293(1):79-89 https://doi.org/10.1007/s11104-007-9245-1

[25] Cerdeira-Pérez A, Monterroso C, Rodríguez-Garrido B, Machinet G, Echevarria G, Prieto-Fernández Á, Kidd PS. Implementing nickel phytomining in a serpentine quarry in NW Spain. *J Geochemical Explor*. 2019;197:1-13 https://doi.org/10.1016/j.gexplo.2018.11.001

[26] Rosenkranz T, Hipfinger C, Ridard C, Puschenreiter M. A nickel phytomining field trial using *Odontarrhena chalcidica* and *Noccaea goesingensis* on an Austrian serpentine soil. *J Environ Manage*. 2019;242:522-528 https://doi.org/10.1016/j.jenvman.2019.04.073

[27] Bani A, Echevarria G, Sulçe S, Morel JL. Improving the agronomy of *Alyssum murale* for extensive phytomining: a five-year field study. *Int J Phytoremediation*. 2015;17(2):117-127 https://doi.org/10.1080/15226514.2013.862204

[28] Nkrumah PN, Chaney RL, Morel JL. Agronomy of 'metal crops' used in agromining. In: van der Ent A, Echevarria G, Baker AJM, Echevarria G, Simonnot M-O, Morel JL, eds. *Agromining: farming for metals. Extracting unconventional resources using plants*. 2nd ed. Cham, Switzerland: Springer Nature; 2021:23-46 https://doi.org/10.1007/978-3-030-58904-2_2

[29] Hipfinger C, Rosenkranz T, Thüringer J, Puschenreiter M. Fertilization regimes affecting nickel phytomining efficiency on a serpentine soil in the temperate climate zone. *Int J Phytoremediation*. 2020:1-8 https://doi.org/10.1080/15226514.2020.1820446

[30] Pędziwiatr A, Kierczak J, Waroszewski J, Ratié G, Quantin C, Ponzevera E. Rock-type control of Ni, Cr, and Co phytoavailability in ultramafic soils. *Plant Soil*. 2018;423(1):339-362 https://doi.org/10.1007/s11104-017-3523-3

[31] Hseu Z-Y. Evaluating heavy metal contents in nine composts using four digestion methods. *Bioresour Technol*. 2004;95(1):53-59 https://doi.org/10.1016/j.biortech.2004.02.008

[32] Peña Icart M. Desarrollo y aplicación de metodologías mediante la simulación de las condiciones digestivas de peces para la evaluación de la biodisponibilidad de metales en sedimentos marinos. Thesis. Cadiz, Spain: Universidad de Cádiz; 2013 (in Spanish) http://hdl.handle.net/10498/15520

[33] Kara D, Özsavaşçi C, Alkan M. Investigation of suitable digestion methods for the determination of total phosphorus in soils. *Talanta*. 1997;44(11):2027-2032 https://doi.org/10.1016/S0039-9140(97)00014-3

[34] Stamenković UM, Andrejić G, Mihailović N, Šinžar-Sekulić J. Hyperaccumulation of Ni by *Alyssum murale* Waldst. & Kit. from ultramafics in Bosnia and Herzegovina. *Appl Ecol Environ Res*. 2017;15(3):359-372 https://doi.org/10.15666/aeer/1503_359372

[35] Xhaferri B, Shallari S, Echevarria G, Bani A. Nickel accumulation by *Alyssum murale* in serpentine sites of Prrenjas and Rajce, Albania. *Eur Acad Res*. 2018;6(8):4791-4803

[36] Barbaroux R, Plasari E, Mercier G, Simonnot M-O, Morel J-L, Blais J-F. A new process for nickel ammonium disulfate production from ash of the hyperaccumulating plant *Alyssum murale*. *Sci Total Environ*. 2012;423:111-119 https://doi.org/10.1016/j.scitotenv.2012.01.063

[37] Houzelot V, Ranc B, Laubie B, Simonnot M-O. Agromining of hyperaccumulator biomass: study of leaching kinetics of extraction of nickel, magnesium, potassium, phosphorus, iron, and manganese from *Alyssum murale* ashes by sulfuric acid. *Chem Eng Res Des*. 2018;129:1-11 https://doi.org/10.1016/j.cherd.2017.10.030

[38] Ростислав Л, Молочко В, Андреева Л. *Константы Неорганических Веществ. Справочник*. Москва: Дрофа; 2006 (in Russian)

[39] Lide DR. *CRC Handbook of Chemistry and Physics*.85 th ed. Boca Raton, London, New York, Washington: CRC press; 2004.

[40] Marescotti P, Comodi P, Crispini L, Gigli L, Zucchini A, Fornasaro S. Potentially toxic elements in ultramafic soils: a study from metamorphic ophiolites of the Voltri Massif (Western Alps, Italy), *Minerals* 2019;9:502 https://doi.org/10.3390/min9080502

[41] Kierczak J, Pietranik A, Pędziwiatr A. Ultramafic geoecosystems as a natural source of Ni, Cr, and Co to the environment: A review. *Sci Total Environ*. 2020:142620 https://doi.org/10.1016/j.scitotenv.2020.142620

[42] Pavlović P, Kostić N, Karadžić B, Mitrović M. *The Soils of Serbia*. Springer; 2017 https://doi.org/10.1007/978-94-017-8660-7

[43] Tomović GM, Mihailović NL, Tumi AF, Gajić BA, Mišljenović TD, Niketić MS. Trace metals in soils and several Brassicaceae plant species from serpentine sites of Serbia. *Arch Environ Prot*. 2013;39(4):29-49 https://doi.org/10.1007/s11104-019-04402-5

[44] Mišljenović T, Jovanović S, Mihailović N, Gajić B, Tomović G, Baker AJM, Echevarria G, Jakovljević K. Natural variation of nickel, zinc and cadmium (hyper) accumulation in facultative serpentinophytes *Noccaea kovatsii* and *N. praecox*. *Plant Soil*. 2020;447(1):475-495 https://doi.org/10.2478/aep-2013-0039

[45] Mišljenović T, Jakovljević K, Jovanović S, Mihailović N, Gajić B, Tomović G. Micro-edaphic factors affect intra-specific variations in trace element profiles of *Noccaea praecox* on ultramafic soils. *Environ Sci Pollut Res*. 2018;25(31):31737-31751 https://doi.org/10.1007/s11356-018-3125-5

[46] Jakovljević K, Mišljenović T, Jovanović S, Grujić M, Mihailović N, Tomović G. *Plantago subulata* as indicator of potentially toxic elements in the substrate. *Environ Sci Pollut Res*. 2021;28(16):20668-20681 https://doi.org/10.1007/s11356-020-11952-0

[47] Bani A, Pavlova D, Garrido-Rodríguez B, Kidd PS, Konstantinou M, Kyrkas D, Morel JL, Prieto-Fernandez A, Puschenreiter M, Echevarria G. Element Case Studies in the Temperate/Mediterranean Regions of Europe: Nickel. In: van der Ent A, Baker AJM, Echevarria G, Simonnot M-O, Morel JL, eds. *Agromining: farming for metals. Extracting unconventional resources using plants.* 2nd ed. Cham, Switzerland: Springer Nature; 2021:341-363 https://doi.org/10.1007/978-3-030-58904-2_16

[48] Rodrigues J, Houzelot V, Ferrari F, Echevarria G, Laubie B, Morel J-L, Simonnot M-O, Pons M-N. Life cycle assessment of agromining chain highlights role of erosion control and bioenergy. *J Clean Prod*. 2016;139:770-778 https://doi.org/10.1016/j.jclepro.2016.08.110

SAŽETAK

Ekstrakcija amonijum-nikl-sulfat-heksahidrata hidrometalurškim procesom iz biljke hiperakumulatora *Odontarrhena muralis* – studija slučaja iz Srbije

Branislav Marković[1], Dragana Ranđelović[1], Gvozden Jovanović[1], Gordana Tomović[2], Ksenija Jakovljević[2], Tomica Mišljenović[2] i Miroslav Sokić[1]

[1]Institut za tehnologiju nuklearnih i drugih mineralnih sirovina, Bulevar Franša d'Eperea 86, Beograd, Srbija
[2]Institut za botaniku i Botanička bašta, Biološki fakultet, Univerzitet u Beogradu, Takovska 43, Beograd, Srbija

(Naučni rad)

Fitorudarenje je savremena tehnika koja koristi biljke hiperakumulatore kao vrstu bio-rude u cilju ekstrakcije metala iz njihove biomase. Hiperakumulator nikla, vrsta Odontarrhena muralis široko je rasprostranjena na ultramafitskim zemljištima u Srbiji i može biti potencijalno dobar izbor za primenu u fitorudarenju nikla. U ovoj studiji ispitana je efikasnost hidrometalurškog procesa regeneracije nikla iz biomase prirodnih populacija O. muralis putem sinteze soli nikla iz pepela biljaka u formi amonijum-nikl-sulfat heksahidrata $Ni(NH_4)_2(SO4)_{2\times}6H_2O$ (ANSH). Prosečan sadržaj nikla u populaciji O. muralis sa ultramafitskih područja u Zapadnoj Srbiji iznosio je 3.300 g kg^{-1}. Maseni prinos ANSH kristala iz početne količine sirovog pepela je bio oko 12% prosečne čistoće 73 %. Optimizacijom procesa prečišćavanja koji prethodi precipitaciji ANSH kristala, moguće je dobiti kristale povećane čistoće, što bi uvećalo ekonomsku profitabilnost ovog procesa. Rezultati ove preliminarne studije na prirodnim populacijama O. muralis u Srbiji pokazuju značajan potencijal za implementaciju prakse fitorudarenja kao alternativnog načina za ekstrakciju nikla sa ultramafita ovog područja.

Ključne reči: fitorudarenje, bio-ruda, luženje, ekstrakcija nikla

Upgrading fuel potentials of waste biomass via hydrothermal carbonization

Jelena Petrović[1], Marija Simić[1], Marija Mihajlović[1], Marija Koprivica[1], Marija Kojić[2] and Ivona Nuić[3]

[1]Institute for Technology of Nuclear and Other Mineral Raw Materials, 86 Franchet d'Esperey St., 11000 Belgrade, Serbia
[2]Institute of Nuclear Sciences "Vinča", University of Belgrade, Laboratory for Radiation Chemistry and Physics "Gamma", 12-14 Mike Petrovića Alasa St., P.O. Box 522, 11001 Belgrade, Serbia
[3]Faculty of Chemistry and Technology, University of Split, Department of Environmental Engineering, 35 Ruđera Boškovića St., 21000 Split, Croatia

Abstract

In recent decades, massive exploitation of fossil fuels caused a growing demand for the production of energies from renewable sources. Hydrochar obtained from waste biomass via hydrothermal carbonization (HTC) possesses good potentials as a biofuel. Therefore, we performed HTC of corn cob, paulownia leaves, and olive pomace at different temperatures (180, 220, and 260 °C). The main goal of this study was to comparatively evaluate the influence of HTC conditions on the structure and fuel characteristics of the obtained solids. The results showed that the yields of hydrochar decrease significantly with increasing temperature in all samples. The carbon content and higher heating value increased and reached the highest values in hydrochars obtained at 260 °C, while the content of volatile matter decreased. Furthermore, the Van Krevelen diagram reveals that the transformation of feedstock to lignite-like products upon HTC was achieved. In this study, the results showed that processes of dehydration and decarboxylation during HTC provoke intensive biomass transformation and that hydrochars obtained at higher temperatures have significantly enhanced fuel properties and fewer volatiles compared to the feedstock.

Keywords: biomass conversion; hydrochar; biofuel; corn cob; paulownia leaves; olive pomace.

Available on-line at the Journal web address: http://www.ache.org.rs/HI/

ORIGINAL SCIENTIFIC PAPER

UDC: 662.6:662.734:62-663.8

Hem. Ind. **75 (5)** 297-305 (2021)

1. INTRODUCTION

Over the years, the increasing demand for energy caused extensive depletion of fossil fuels, which led to a series of environmental problems. To minimize these damaging effects, many countries have turned to the adoption and implementation of the concept of a bio-based economy, which involves the utilization of waste biomass as new value-added materials, instead of landfilling. Waste biomass is a source that includes different agricultural and forest residues, municipal waste streams, sewage sludge, organic waste, and others. However, the direct application of crude biomass has several disadvantages that include low energetic potential, hygroscopic nature, and release of volatiles during combustion [1,2]. Additionally, high ash content due to the presence of different metals in raw biomass causes corrosion, clogging, and/or clinkers formation in the furnaces. The mentioned problems impair the quality and combustion efficiency of the solid fuel and therefore reduce the motivation for waste biomass utilization. To overcome these disadvantages, development of thermochemical conversion processes of biomass into multi-functional products received considerable attention. These technologies are torrefaction, pyrolysis, gasification, and hydrothermal carbonization (HTC) [3-5]. The last-mentioned technology has been recognized as highly effective for production of carbon-rich material, hydrochar, from wet and waste biomass.

Corresponding author: Institute for Technology of Nuclear and Other Mineral Raw Materials, 86 Franchet d'Esperey St., 11000 Belgrade, Serbia, Tel/Fax: +381 11 3691 722
E-mail: j.petrovic@itnms.ac.rs
Paper received: 07 May 2021; Paper accepted: 11 October 2021; Paper published: 27 October 2021.
https://doi.org/10.2298/HEMIND210507025P

CC BY NC ND

HTC process is carried out in a sealed autoclave, in which the biomass in water suspension is exposed to moderate temperatures (180-280 °C) and autogenetic pressure (up to 50 bar). Reaction times vary from several minutes to several hours. Unlike traditional conversion methods, the main advantage of HTC is that it proceeds at much milder reaction conditions. Besides, water as a reaction medium enables processing of wet biomass without prior drying. These characteristics significantly reduce the costs and energy consumption during carbonization and enable utilization of a wide range of waste biomass. Moreover, HTC exhibits a high carbon conversion rate, without methane or CO_2 emission [4-7].

Main products of feedstock decomposition under HTC conditions are carbon-rich hydrochar and process water, rich in organic components. Reaction pathways that cause transformation of the raw biomass into hydrochar include hydrolysis, dehydration, decarboxylation, condensation, polymerization, and aromatization [8]. During the HTC process, water acts as a non-polar solvent and catalyzes the degradation of the biomass constituents. As previously established, this degradation begins with hydrolysis, which requires lower reaction temperatures, while higher temperatures promote dehydration, decarboxylation and condensation reactions [3,9]. Furthermore, carbonization in aqueous medium provides a number of oxygenated functional groups at the solid surface [9]. It is known that the structure and characteristics, and thus further application, of the obtained carbonaceous solids, depend on the applied process conditions, as well as the feedstock type [4,5,7,10]. Previous research has shown that reaction temperature has the most significant role in hydrochar formation. At lower reaction temperatures, hydrochars abundant in functional groups on their surface are formed. This feature makes these materials suitable for potential utilization as adsorbents. On the other hand, elevated temperatures provoke the formation of materials with higher carbon contents and better energetic properties, but with lower solid yield due to intense degradation [9,11].

Summarizing previous findings, it can be concluded that the structure and characteristics of the obtained hydrochars are significantly different from the parental feedstock. Hydrochars exhibit superior performance that includes higher carbon content and energy density, better dewaterability and stability, more reactive groups on the surfaces and improved fuel properties [2,11,12]. Moreover, during carbonization inorganic components are leached into the process water, so hydrochar displays a lower ash content as compared to the starting biomass [6]. Current valorization of hydrochar involves its potential utilization for water purification, as an energy source, for carbon sequestration, as bio-fertilizers, energy storage materials, *etc.* [2,4,5,13-15]. With this regard, numerous waste streams (agricultural residues, algae, municipal solid waste, and sewage sludge) have been utilized as precursors to produce hydrochars [2]. Special attention is drawn to the use of waste lignocellulosic biomass, like agricultural and forest residues, since HTC conversion of these materials provides valuable chemicals, energy sources, adsorbents, and more.

This paper focuses on the valorization of three different bio-residues (corn cob, paulownia leaves, and olive pomace) *via* HTC. The main goal was to examine the influence of process temperature on the structure and characteristics of the obtained hydrochars, towards determination of potentials for further utilization as an alternative energy source. With this aim, solids yield, elemental analysis, along with combustion characteristics that include volatile matter contents, higher heating values (*HHV*), and energy densification (*ED*) were determined in all obtained hydrochars and compared to the feedstock. The practical significance of this paper is to determine suitability of selected biomass as a precursor for the production of energy-rich biofuels, with simultaneous reduction of waste generation in the environment.

2. MATERIALS AND METHODS

2. 1. Biomass collection and preparation

The selected waste biomass samples, corn cob (CC), paulownia leaf (PL), and olive pomace (OP) were randomly collected from open landfill sites where they were disposed after processing. The collected feedstock was air-dried, ground, and sieved in order to provide homogeneity of the sample prior to hydrothermal treatment. Hydrothermal experiments were performed with sieved sample fractions of 0.5 mm.

2. 2. Hydrothermal experiments and hydrochar characterization

In order to produce hydrochar from prepared feedstock, a laboratory autoclave (Carl Roth, Model II, 250 cm^3, Germany) equipped with a temperature controller, thermocouple and a manometer, was used. During the treatment, 10 g of waste biomass in 150 cm^3 of ultrapure water (solid to liquid mass ratio 1:15) were hydrothermally carbonized at three different temperatures: 180, 220, and 260 °C, within 1 h. The pressure during the carbonization process was not controlled. It was autogenic and saturated corresponding to the applied carbonization temperature. Upon completion of carbonization, the solid product was separated from the process water by filtration, rinsed several times using ultrapure water, dried in an oven at 105 °C to constant weight, weighted, and stored until further experiments. The obtained hydrochars were labeled according to the biomass type and temperature at which it was produced, as follows: CC-180, CC-220 and CC-260 (for the CC carbonized at 180, 220, and 260 °C, respectively); PL-180, PL-220 and PL-260 (for the PL carbonized at 180, 220, and 260 °C, respectively), and OP-180, OP-220 and OP-260 (for the OP carbonized at 180, 220, and 260 °C, respectively).

Mass yield of the obtained hydrochars was determined as the ratio of dry hydrochar and dry biomass [4]. Volatile matter (VM) and ash was determined by the standard ASTM D1762-84 (2007) procedure. Additionally, elemental analysis (C, H, N, S) of all samples was performed by using a Vario EL III; C, H, N, S/O Elemental Analyzer (Elementar, Germany) equipped with a thermal conductivity detector (TCD), while O contents (%) were calculated by subtracting the sum of the obtained elemental values from 100 %. The *HHV* and *ED* values were calculated from the results of elemental analysis according to equations (1) and (2), respectively [16,17]:

$$HHV = 0.3491C + 1.1783H + 0.1005S - 0.1034O - 0.0151N - 0.0211Ash \quad (1)$$

where *C, H, S, O, N* and *Ash* are the mass percentages of the elemental carbon, hydrogen, sulfur, oxygen and nitrogen, and ash content, respectively.

$$ED = \frac{HHV_{\text{hydrochar}}}{HHV_{\text{biomass}}} \quad (2)$$

All experiments were performed in triplicate and average values is shown in the results.

3. RESULTS

Influence of the process temperature on the solid yield of hydrochars obtained at 180, 220, and 260 °C for the three starting biomass types (CC, PL and OP) is demonstrated in Figure 1.

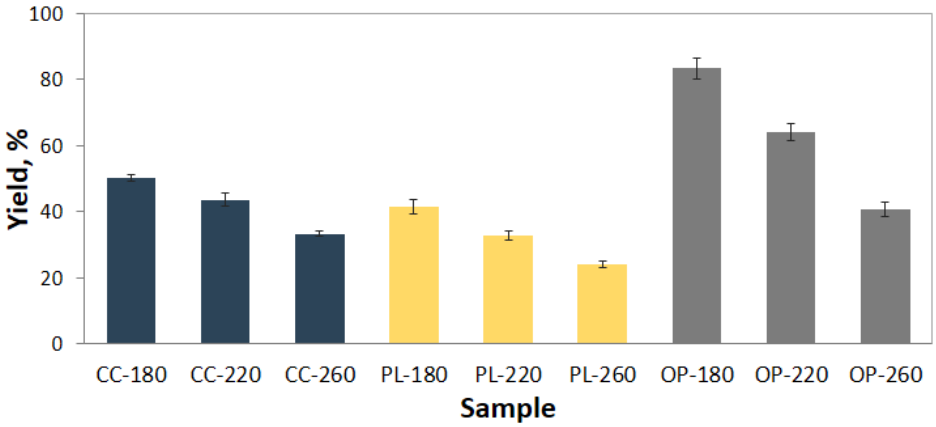

Figure 1. Yields of solid hydrochars obtained from corn cob (CC), paulownia leaf (PL), and olive pomace (OP) at different carbonization temperatures (180, 220 and 260 °C)

As it can be seen, the solid yield of all produced hydrochars decreased with the temperature increase and reached the lowest values for materials produced at 260 °C. Although this decrease is observed for all investigated biomass

types, it was the most pronounced for OP, decreasing from 83.25±3.05 % at 180 °C to 40.63±2.02 % at 260 °C. This progressive weight loss upon the increase the reaction temperature can be explained by degradation of the basic constituents of lignocellulosic biomass (hemicellulose, cellulose and lignin) during the hydrothermal treatment, particularly as a result of intense dehydration and decarboxylation reactions with simultaneous leaching of organic and water-soluble components from the solid into the process water. It is known that the degradation of hemicellulose under HTC conditions begins already at 180 °C, while reaction temperatures above 200 °C are required for decomposition of cellulose and lignin into smaller constituents [4,5,18]. Therefore, it can be expected that lignin-rich biomass provides higher mass yields. Accordingly, the highest mass yield observed for the OP-180 in comparison to the CC-180 and PL-180 suggests that OP probably contains more cellulose and lignin than more easily degradable hemicelluloses. On the other hand, the lowest yields are noticed for all PL hydrochars (from 41.44±2.23 % to 24.00±1.05 %) indicating that the main constituents of this biomass are thermally unstable lignocellulosic compounds, which underwent the greatest degradation during the HTC treatment. Our results are in accordance with previous studies of the influence of temperature on the mass yield of hydrochars from different biomass precursors [2,19,20]. It was found that the biomass type directly affected the mass yields of hydrochars produced at the same hydrothermal conditions [2]. The authors stated that the mass yield from a mixed feedstock, such as olive pomace, depends not only on the lignocellulose content but also on interactions between the biomass constituents [2]. According to their observations, the achieved yield upon carbonization at 220 °C was 65.8 and 64.8 % for olive pomace and walnut shell, respectively, which is comparable to the OP-220 yield in the present study (64.00±2.46 %). Recently, in two separate studies a gradual decrease in the hydrochar yield was reported as the temperature was increased from 180 to 260 °C [19,20]. The obtained hydrochars solid yields were in the range 57.20-38.32 % for the spent mushroom substrate [19] and 53.8-35.0 % for the food waste [20]. These values are in accordance with the results of solid yields obtained in our study. Similar to our observations, the decreasing trend as a result of pronounced biomass decomposition with an increase in the reaction temperature was also noticed during carbonization (180-240 °C) of eucalyptus, giant bamboo, coffee wood and coffee parchment [21], as well as during optimization of the HTC process for production of grape pomace [4] and miscanthus [5] hydrochars.

To gain a better insight into the transformation and improvement of fuel characteristics of the obtained hydrochars, analyses of volatile substances, elemental composition, *HHV* and *ED* were performed. Table 1 summarizes the results of volatiles and elemental composition for three selected biomass types before and after carbonization treatment.

Table 1. Volatile contents and elemental compositions for initial biomass samples and hydrochars produced at different temperatures.

Sample	Content, %					
	Volatiles	C	H	N	S	O
CC	90.45±2.14	43.81±0.05	6.08±0.01	0.41±0.11	<0.01	48.86±0.16
CC-180	91.56±1.05	47.20±0.15	5.95±0.01	0.42±0.06	<0.01	46.29±0.20
CC-220	81.83±0.66	48.98±0.04	5.88±0.00	0.28±0.02	<0.01	44.59±0.06
CC-260	55.42±0.21	69.30±0.11	4.88±0.01	0.57±0.01	<0.01	25.11±0.11
PL	76.70±0.71	45.75±0.16	6.03±0.03	3.82±0.02	0.50±0.04	38.19±0.13
PL-180	75.31±1.03	55.24±0.15	6.37±0.12	3.34±0.11	0.45±0.02	29.21±0.06
PL-220	71.15±0.87	60.64±0.08	6.36±0.01	3.08±0.01	0.37±0.02	23.07±0.10
PL-260	62.10±0.58	64.54±0.16	6.34±0.01	3.18±0.20	0.35±0.08	16.72±0.08
OP	82.86±1.37	53.86±0.12	7.28±0.02	1.13±0.03	<0.01	37.53±0.11
OP-180	87.15±2.01	60.93±0.14	7.75±0.08	1.05±0.07	<0.01	30.29±0.31
OP-220	79.66±1.01	64.08±0.17	7.30±0.01	0.75±0.05	<0.01	27.89±0.22
OP-260	66.77±0.42	70.97±0.18	6.80±0.00	0.83±0.06	<0.01	21.41±0.25

From the results (Table 1) it can be concluded that hydrothermal carbonization promoted degradation of volatiles in almost all tested samples. These results vary depending on the biomass type used as a precursor. Consequently, one of the significant objectives of this study was to realize which type of biomass and which carbonization temperature are the most suitable for production of hydrochars with the best fuel characteristics. With this regard, it can be noticed that the CC has the highest content of volatile matter (90.45±2.14 %), although the other two biomass samples have also

rather high contents of volatiles. High amount of volatiles is one of the peculiarities of biomass feedstock. This feature is one of the main obstacles for direct combustion of raw biomass since it causes higher reactivity and lower enthalpy, and further, leads to low combustion efficiency, evaporation and emission problems, which are the opposite effects in comparison to fossil coal [22]. Therefore, it can be concluded that CC, PL, and OP are not suitable to be exploited as efficient fuel sources. However, as it can be seen in Table 1, hydrothermal treatment at higher temperatures promoted a significant reduction in the VM content. The exception to this trend was found in OP-180 and CC-180 samples, which showed a slight increase in the VM content in comparison to the initial biomass samples. An increase in volatile matter content (from 80.7 to 82.2 %) during hydrothermal treatment of municipal solid waste at 180 °C was previously reported [23]. Since lignocellulose under HTC conditions starts to hydrolyze at 180 °C, a reason for this unexpected behavior could be accumulation of leached volatile compounds from the process water onto the formed hydrochar surface [24]. Wang *et al.* [25] also observed adsorption of volatile compounds during carbonization of sludge. The authors reveal that this phenomenon is mostly pronounced during HTC treatment at 180 °C, while a further increase in temperature promotes reduction in devolatilization rate and formation of a more stable hydrochar. Consistently, a general decrease in volatile contents upon temperature increase was also noticed during our research. The most intensive reduction in this content is observed in the CC hydrochars, and thus the CC-260 has only 55.42±0.21 % of volatiles, which is significantly lower than that in PL-260 (62.10±0.58 %) and OP-260 (66.77±0.42 %) samples. The observed significant VM content reductions in produced hydrochars upon the temperature increase from 180 to 260 °C is probably induced by hydrolysis, dehydration and decarboxylation of lignocellulosic biomass constituents. Although the mechanism of biomass conversion to hydrochar is not yet fully elucidated, numerous authors have found that it begins with the hydrolysis that causes devolatilization of biomass macromolecules into oligomers and monomers. These fragments are subject to subsequent degradation mechanisms that include dehydration and decarboxylation, followed by aromatization to the formation of carbon rich solids [2,7,9,15,16]. Simultaneous occurrence of these degradation reactions during HTC causes formation of hydrochars with lower volatile contents as compared to the corresponding starting biomasses [2,15,16]. The results (Table 1) indicate that this degradation is more pronounced at higher carbonization temperatures. In hydrothermal carbonization of olive mill wastewater, a decrease in the volatile matter content from 84.00 % to 78.21 % was also noticed during carbonization at different temperatures [15]. Besides, VM content reduction after HTC processing of wood sawdust, walnut shell, tea stalk, olive pomace, apricot seed and hazelnut husk was also observed by Kabakci and Baran [2].

Chemical transformations during HTC can be best described by the results of elemental analysis regarding C, H and O contents. It can be deduced that the hydrochars elemental content is highly dependent on the carbonization temperature. Hence, with the simultaneous lowering of the volatiles, a significant increase in the C content in hydrochar samples was observed. The increase in the reaction temperature from 180 to 260 °C promoted a gradual increase in the C content in the CC samples from the initial 43.81±0.05 % to 47.20±0.15 in CC-180 and up to 69.30±0.11 % in CC-260. Besides, both OP and PL also show an increase in the C content that ranged from 53.86±0.12 % in the OP up to 70.97±0.18 % (OP-260), and from 45.75±0.16 % for PL to 64.54±0.16 % (PL-260). The observed increase in the C content reveals that intensive carbonization of biomass occurred. On the contrary, H and O contents decreased with the increase in the reaction temperature, which further confirms dehydration and decarboxylation of biomass during the HTC process.

According to the obtained values for C, H and O contents, atomic ratios (H/C and O/C) were calculated for all biomass and hydrochar samples. The evolution of H/C and O/C atomic ratios of raw CC, OP, PL and its hydrochars could be visualized by the Van Krevelen diagram [26,27] in Figure 2.

A van Krevelen diagram (named after the Dutch chemical engineer Dirk Willem van Krevelen) represents graphical plots used to illustrate difference in chemical composition of natural fuels like biomass and fossil fuels, by plotting H/C atomic ratios as a function of O/C atomic ratios obtained from elemental analysis [26,27]. This diagram provides a clear insight into the chemical transformation and coalification of biomass to carbon-rich materials, which occur as a result of demethanation, dehydration and decarboxylation reactions during HTC [7,13]. High H/C and O/C atomic ratios indicate the presence of plant macromolecules, such as cellulose, hemicellulose and lignin, while low coefficients are typical for aromatic structures [10].

CC BY NC ND

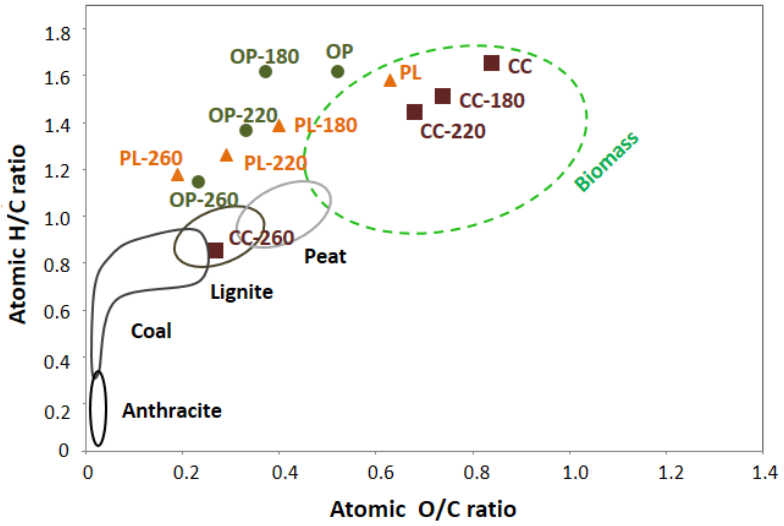

Figure 2. Van Krevelen diagram of starting biomass samples and the obtained hydrochars along with data for typical fuels (typical value range for biomass is indicated by a green circle)

It could be seen in Figure 2 that all three feedstock samples are located in the region characteristic for raw biomass [3-5,7,19,26]. On the other hand, as the carbonization temperature increases, a more progressive decrease in atomic ratios is observed, and the position of the obtained hydrochars has shifted to the lower-left corner of the Van Krevelen diagram (Fig. 2). This practically means that higher reaction temperatures promote the removal of H_2O and CO_2 from feedstock during HTC, followed by intensive condensation of polycyclic structures, whereby a more aromatic lignite-like hydrochar is formed. Thus, Figure 2 shows that the increase of the applied HTC temperature from 180 to 260 °C, induced translocation of hydrochar positions from the region of biomass, through the peat stage, all the way close to the lignite region. There, the CC-260 is on the boundary of lignite and coal, indicating CC carbonization at 260 °C to the material which is structurally similar to commercial coal. Energy sources that exhibit low H/C and O/C atomic ratios were regarded as remarkably desirable due to reduced energy loss and smoke formation during direct combustion [3]. Our results show such desired achievement since the obtained hydrochars showed lower atomic ratios in relation to the corresponding precursors.

Based on our findings, it can be concluded that hydrothermal treatment significantly improves the fuel characteristics of waste biomass, and provides potentials for further application of hydrochars as an energy source. Calculated values of *HHV* and *ED* further confirm these conclusions (Table 2).

Table 2. HHV values and energy density (ED) of waste biomass and obtained hydrochar samples

Sample	*HHV* / MJ kg^{-1}	*ED*
CC	17.31±0.03	-
CC-180	18.69±0.05	1.08±0.00
CC-220	19.41±0.01	1.12±0.00
CC-260	27.33±0.03	1.58±0.00
PL	18.99±0.08	-
PL-180	23.65±0.15	1.25±0.01
PL-220	26.13±0.02	1.38±0.00
PL-260	28.06±0.05	1.48±0.01
OP	23.45±0.06	-
OP-180	27.24±0.15	1.16±0.00
OP-220	28.07±0.06	1.19±0.01
OP-260	30.55±0.07	1.30±0.00

HHV values increased with the increase in temperature from 180 to 260 °C where the highest value was obtained for OP-260 amounting to 30.55±0.07 MJ kg^{-1}. Although the starting biomasses exhibited high *HHV* values, hydrothermal treatment further enhanced this fuel characteristic for almost 10 MJ kg^{-1} in the CC-260 and PL-260 samples while about 6 MJ kg^{-1} in the OP-260 sample. Removal of substances with low *HHV* such as hemicellulose (13.9 MJ kg^{-1}) [28] and

cellulose (16.5 MJ kg^{-1}) [28] from the biomass during HTC can cause an increase in *HHV* of the produced hydrochars [1,28]. Furthermore, as the reaction temperature was elevated degradation of structure constituents was accelerated, causing higher *HHV*. Besides, when compared to lignite (16.3 MJ kg^{-1}) [29], all obtained hydrochars from exhibit better energy potentials (Table 2) than this commercial coal. The upward trend caused by the elevation of the process temperature is also noticeable for the *ED* (Table 2). The increase in the *ED* value varied depending on the biomass type, and it ranged from 1.08±0.00 to 1.58±0.00 for CC, from 1.16±0.00 to 1.30±0.00 for OP and from 1.25±0.01 to 1.48±0.01 for PL. Thus, both energy parameters increased with the increase in the process temperature. Similar findings were obtained earlier for olive pomace mill, food waste and spent mushroom substrate hydrochars in studies of potential applications as energy sources [15,19,30]. However, when comparing all of the obtained hydrochars, although the PL-260 sample shows a high *HHV* value, it is characterized by a very low yield, which significantly reduces its potential for commercial application as a solid fuel. This could represent an obstacle for the valorization of PL into a fuel source *via* the HTC technology. Therefore, it is practically very important to determine the best reaction conditions as well as the type of biomass, which will provide the material with the best characteristics for further use as a fuel. Summarizing our results, it can be concluded that the CC and OP hydrochars obtained at higher temperature can be considered as potential candidates for use as solid biofuels because these materials are characterized by good yields, satisfactory *HHV* values and energy density, while the content of volatiles is significantly reduced.

4. CONCLUSIONS

Within this study, hydrothermal carbonization was successfully utilized for valorization of waste corn cob, olive pomace and paulownia leaf into carbon-rich solid materials. Hydrochars produced at different carbonization temperatures displayed distinct structural and fuel characteristics. Results reveal that the increase in the reaction temperature causes a decrease in the solid yield due to degradation of the biomass matrix. Besides, all hydrochars showed lower volatile matter, hydrogen and oxygen contents, with a simultaneous significant increase in the carbon content and heating values. Summarizing the results obtained in this study, it can be concluded that hydrochars produced at higher carbonization temperatures show superior fuel characteristics compared to the corresponding starting raw materials. The overall results emphasize the potential of HTC technology to exploit waste biomass as a precursor for novel energy sources with upgraded combustion performance.

Acknowledgements: The authors are grateful to the Serbian Ministry of Education, Science and Technological Development for the financial support of this investigation (contract no. 451-03-9/2021-14/200023).

REFERENCES

[1] Qi R, Xu Z, Zhou Y, Zhang D, Sun Z, Chen W, Xiong M. Clean solid fuel produced from cotton textiles waste through hydrothermal carbonization with $FeCl_3$: Upgrading the fuel quality and combustion characteristics. *Energy*. 2021; 214: 118926 https://doi.org/10.1016/j.energy.2020.118926

[2] Kabakcı SB and Baran SS. Hydrothermal carbonization of various lignocellulosics: Fuel characteristics of hydrochars and surface characteristics of activated hydrochars. *Waste Manage*. 2019; 100: 259-268 https://doi.org/10.1016/j.wasman.2019.09.021

[3] Kambo SH and Dutta A. Strength, storage, and combustion characteristics of densified lignocellulosic biomass produced via torrefaction and hydrothermal carbonization. *Appl Energy*. 2014; 135: 182-191 https://doi.org/10.1016/j.apenergy.2014.08.094

[4] Petrović J, Perišić N, Dragišić Maksimović J, Maksimović V, Kragović M, Stojanović M, Laušević M, Mihajlović M. Hydrothermal conversion of grape pomace: Detailed characterization of obtained hydrochar and liquid phase. *J Anal Appl Pyrol*. 2016; 118: 267-277 https://doi.org/10.1016/j.jaap.2016.02.010

[5] Mihajlović M, Petrović J, Maletić S, Kragulj Isakovski M, Stojanović M, Lopičić Z, Trifunović S. Hydrothermal carbonization of *Miscanthus × giganteus*: Structural and fuel properties of hydrochars and organic profile with the ecotoxicological assessment of the liquid phase. *Energy Convers Manage*. 2018; 159: 254-263 https://doi.org/10.1016/j.enconman.2018.01.003

[6] Pauline AL and Joseph K. Hydrothermal carbonization of organic wastes to carbonaceous solid fuel –A review of mechanisms and process parameters. *Fuel*. 2020; 279: 118472. https://doi.org/10.1016/j.fuel.2020.118472

[7] Reza MT, Andert J, Wirth B, Busch D, Pielert J, Lynam JG, Mumme J. Hydrothermal Carbonization of Biomass for Energy and Crop Production. *Appl Bioenergy.* 2014; 1: 11-29 https://doi.org/10.2478/apbi-2014-0001

CC BY NC ND

[8] Wang T, Zhai Y, Zhu Y, Li C, Zeng G. A review of the hydrothermal carbonization of biomass waste for hydrochar formation: process conditions, fundamentals, and physicochemical properties. *Renew Sustain Energy Rev*. 2018; 90: 223-247 https://doi.org/10.1016/j.rser.2018.03.071

[9] Funke A and Ziegler F. Hydrothermal carbonization of biomass: A summary and discussion of chemical mechanisms for process engineering. *Biofuel Bioprod Biorefin.* 2010; 4: 160-177 https://doi.org/10.1002/bbb.198

[10] Cao X, Ro KS, Libra JA, Kammann CI, Lima I, Berge N, Li L, Li Y, Chen N, Yang J, Deng B, Mao J. Effects of Biomass Types and Carbonization Conditions on the Chemical Characteristics of Hydrochars. *J Agric Food Chem*. 2013; 61: 9401-9411 https://doi.org/10.1021/jf402345k

[11] Jain A, Balasubramanian R, Srinivasan MP. Tuning hydrochar properties for enhanced mesopore development in activated carbon by hydrothermal carbonization. *Micropor Mesopor Mat*. 2015; 203: 178-185 https://doi.org/10.1016/j.micromeso.2014.10.036

[12] Zhang L, Wang Q, Wang B, Yang G, Lucia LA, Chen J. Hydrothermal carbonization of corncob residues for hydrochar production. *Energy Fuels*. 2015; 29: 872-876 https://doi.org/10.1021/ef502462p

[13] Fuertes AB and Sevilla M. Hierarchical microporous/mesoporous carbon nanosheets for high-performance supercapacitors. *ACS Appl Mater Interf*. 2015; 7: 4344-4353 https://doi.org/10.1021/am508794f

[14] Petrović J, Stojanović M, Milojković J, Petrović M, Šoštarić T, Laušević M, Mihajlovć M. Alkali modified hydrochar of grape pomace as a perspective adsorbent of Pb^{2+} from aqueous solution. *J Environ Manage.* 2016; 182: 292–300. https://doi.org/10.1016/j.jenvman.2016.07.081

[15] Azzaz AA, Jeguirim M, Kinigopoulou V, Doulgeris C, Goddard ML, Jellali S, Matei Ghimbeu C. Olive mill wastewater: From a pollutant to green fuels, agricultural and water source and bio-fertilizer-Hydrothermal carbonization. *Sci Total Environ*. 2020; 733: 139314 https://doi.org/10.1016/j.scitotenv.2020.139314

[16] Kim D, Lee K, Park KY. Hydrothermal carbonization of anaerobically digested sludge for solid fuel production and energy recovery. *Fuel*. 2014; 130: 120-125 https://doi.org/10.1016/j.fuel.2014.04.030

[17] Lu X, Ma X, Chen X. Co-hydrothermal carbonization of sewage sludge and lignocellulosic biomass: Fuel properties and heavy metal transformation behavior of hydrochars. *Energy*. 2021; 221: 119896 https://doi.org/10.1016/j.energy.2021.119896

[18] Afolabi OOD, Sohail M, Cheng YL. Optimisation and characterisation of hydrochar production from spent coffee grounds by hydrothermal carbonization. *Renew Energy*. 2020; 147: 1380-1391 https://doi.org/10.1016/j.renene.2019.09.098

[19] Kojić M, Petrović J, Petrović M, Stanković S, Porobić S, Marinović-Cincović M, Mihajlović M. Hydrothermal carbonization of spent mushroom substrate: Physicochemical characterization, combustion behavior, kinetic and thermodynamic study. *J Anal Appl Pyrol*. 2021; 155: 105028 https://doi.org/10.1016/j.jaap.2021.105028

[20] Wang T, Zhai Y, Zhu Y, Gan X, Zheng L, Peng C, Wang B, Li C, Zeng G. Evaluation of the clean characteristics and combustion behavior of hydrochar derived from food waste towards solid biofuel production. *Bioresour Technol.* 2018; 266: 275-283 https://doi.org/10.1016/j.biortech.2018.06.093

[21] Mendoza Martinez CL, Sermyagina E, Saari J, de Jesus MS, Cardoso M, de Almeida GM, Vakkilainen E. Hydrothermal carbonization of lignocellulosic agro-forest based biomass residues. *Biomass Bioenergy.* 2021; 147: 106004 https://doi.org/10.1016/j.biombioe.2021.106004

[22] Sharma HB, Panigrahi S, Dubey BK. Hydrothermal carbonization of yard waste for solid bio-fuel production: Study on combustion kinetic, energy properties, grindability and flowability of hydrochar. *Waste Manage*. 2019; 91: 108-119 https://doi.org/10.1016/j.wasman.2019.04.056

[23] Ischia G, Fiori L, Gao L, Goldfarb JL. Valorizing municipal solid waste via integrating hydrothermal carbonization and downstream extraction for biofuel production. *J Clean Prod.* 2021; 289: 125781 https://doi.org/10.1016/j.jclepro.2021.125781

[24] Santos Santana M, Pereira Alves R, da Silva Borges WM, Francisquini E, Guerreiro MC. Hydrochar production from defective coffee beans by hydrothermal carbonization. *Bioresour Technol.* 2020; 300: 122653 https://doi.org/10.1016/j.biortech.2019.122653

[25] Wang L, Li A, Chang Y. Hydrothermal treatment coupled with mechanical expression at increased temperature for excess sludge dewatering: Heavy metals, volatile organic compounds and combustion characteristics of hydrochar. *Chem Eng J*. 2016; 297: 1-10 https://doi.org/10.1016/j.cej.2016.03.131

[26] McKendry P. Energy production from biomass (part 2): conversion technologies. *Bioresour Technol*. 2002; 83: 47-57 https://doi.org/10.1016/S0960-8524(01)00119-5

[27] Ahmad M and Subawi H. New Van Krevelen diagram and its correlation with the heating value of biomass. *Res J Agric Environ Manage*. 2013; 2: 295-301 http://apexjournal.org/rjaem/archive/2013/Oct/fulltext/Ahmad%20and%20Subawi.pdf

[28] Kim D, Lee K, Park KY. Upgrading the characteristics of biochar from cellulose, lignin, and xylan for solid biofuel production from biomass by hydrothermal carbonization. *J Ind Eng Chem.* 2016; 42: 95-100 https://doi.org/10.1016/j.jiec.2016.07.037

[29] He C, Giannis A, Wang JY. Conversion of sewage sludge to clean solid fuel using hydrothermal carbonization: Hydrochar fuel characteristics and combustion behavior. *Appl Energy.* 2013; 111: 257-266 https://doi.org/10.1016/j.apenergy.2013.04.084

[30] Akarsu K, Duman G, Yilmazer A, Keskin T, Azbar N, Yanik J. Sustainable valorization of food wastes into solid fuel by hydrothermal Carbonization. *Bioresour Technol.* 2019; 292: 121959 https://doi.org/10.1016/j.biortech.2019.121959

SAŽETAK

Poboljšanje gorivnog potencijala otpadne biomase primenom hidrotermalne karbonizacije

Jelena Petrović[1], Marija Simić[1], Marija Mihajlović[1], Marija Koprivica[1], Marija Kojić[2] i Ivona Nuić[3]

[1]Institut za tehnologiju nuklearnih i drugih mineralnih sirovina, Bulevar Franše d'Eperea 86, 11000 Beograd, Srbija
[2]Institut za nuklearne nauke „Vinča“, Laboratorija za radijacionu hemiju i fiziku, „Gama“, Univerzitet u Beogradu, Mike Petrovića Alasa 12-14, P.O. Sektor 522, 11001 Beograd, Srbija
[3]Kemijsko-tehnološki fakultet Sveučilišta u Splitu, Odsjek za inženjerstvo zaštite okoliša, Ruđera Boškovića 35, 21000 Split, Hrvatska

(Naučni rad)

Poslednjih decenija masovna eksploatacija fosilnih goriva dovela je do sve veće potražnje za proizvodnjom energije iz obnovljivih izvora. Hidročađi dobijene hidrotermalnom karbonizacijom (engl. hydrothermal carbonization, HTC) otpadne biomase poseduju veliki potencijal kao biogorivo. U ovom radu su zato hidrotermalno karbonizovani oklasak kukuruza, listove paulovnije i kominu masline na različitim temperaturama (180, 220 i 260 °C). Glavni cilj ovog rada jeste uporedna procena uticaja HTC uslova na strukturu i gorivne karakteristie dobijenih proizvoda. Dobijeni rezultati su pokazali da se prinosi hidročađi značajno smanjuju sa porastom temperature u svim uzorcima. Sadržaj C i gornje toplotne moći rastu i dostižu najviše vrednosti u hidročađima dobijenim na 260°C, dok se sadržaj isparljivih materija smanjuje. Dalje, Van Krevelenov dijagram ukazuje da je tokom HTC procesa postignuta transformacija sirovine u proizvode slične lignitu. Naime, rezultati su pokazali da procesi dehidratacije i dekarboksilacije izazivaju intenzivnu transformaciju biomase i da hidročađi dobijene na višim temperaturama imaju značajno poboljšana gorivna svojstva i manji sadržaj isparljivih materija u poređenju sa polaznom sirovinom.

Ključne reči: konverzija biomase; hidročađ; biogorivo; oklasak kukuruza; lišće paulovnije; komina masline

Application of impregnated biocarbon produced from soybean hulls in dye decolorization

Aleksandra Kulić Mandić, Milena Bečelić Tomin, Gordana Pucar Milidrag, Milena Rašeta and Đurđa Kerkez

Faculty of Sciences, University of Novi Sad, Department of Chemistry, Biochemistry and Environmental Protection, 21000 Novi Sad, Serbia

Abstract

Waste soybean hulls (WSH) were investigated as a Fe-support in two forms: raw and carbonized (*i.e*. biocarbon, BC), as possible value-added materials. Fe-impregnation was implemented in order to produce heterogeneous Fenton catalysts for Reactive Blue 4 dye degradation. Materials characterization demonstrated a rise in the specific surface area due to decomposition of WSH constituents during carbonization (to obtain BC) and thermal activation (to obtain Fe-WSH and Fe-BC), thus producing catalysts with high mesoporosity and hematite as the active site for Fenton reaction. Among the investigated materials, Fe-WSH showed the greatest ability for $^{\bullet}OH$ production in acidic medium. Next, the heterogeneous Fenton process was optimized by using response surface methodology, which resulted in selection of the following reaction conditions: 3 mM H_2O_2, 100 mg Fe-WSH, reaction time of 180 min, at a constant pH 3, RB4 concentration of 50 mg dm^{-3} and at room temperature. The achieved dye removal and mineralization were 85.7 and 66.8 %, respectively, while the catalyst showed high stability and the reaction intermediates formed during the oxidation process had a low inhibitory effect on *Vibrio fischeri* bacteria.

Keywords: valorization; Fe(III)-impregnation; response surface methodology; Reactive Blue 4; reuse.

Available on-line at the Journal web address: http://www.ache.org.rs/HI/

ORIGINAL SCIENTIFIC PAPER

UDC: 66.099.72:676.87:
(662.734+582.736.308)

Hem. Ind. **75 (5)** 307-320 (2021)

1. INTRODUCTION

Textile industry has a highly demanding production in terms of water, chemicals and energy consumption. Only in cotton dyeing process more than 100 L of fresh water is used per 1 kg of textile, where unfixed reactive dyes (up to 50 % of the initial concentration) end up in wastewaters [1,2]. The dye presence in water bodies has a highly negative influence on aquatic organisms [3]. For example, Reactive Blue 4 (RB4) dye, which is commonly used, shows acute toxicity to fish [4]. Structurally, RB4 consists of a dichlorotriazine group and anthraquinone chromophore. Due to its high water solubility and low biodegradability, wastewater treatment is required in processes using this dye [5,6].

Advanced oxidation processes (AOPs), based on radical generation with significant redox potential, can non-selectively degrade dye aromatic structures. Among many AOPs, the heterogeneous Fenton process is emphasized due to simple operation, wide application range and successful pollutant oxidation [7–12]. As biological treatments are commonly used in textile industry, Fenton reaction can be implemented as a pre- or post-technique in the hybrid wastewater treatment.

Synthesis of active, stable, and reusable catalyst is a top concern for researchers. An overview of various support materials used as catalysts in heterogeneous Fenton reaction was given in recent review studies [7,9,13]. Some of the mostly used are clays, zeolites, activated carbon, silicates and biosorbents. A common method for catalyst preparation is

Corresponding author: Milena Bečelić-Tomin, Faculty of Sciences, Department of Chemistry, Biochemistry and Environmental Protection, 21000 Novi Sad, Serbia

E-mail: milena.becelic-tomin@dh.uns.ac.rs

Paper received: 27 April 2021; Paper accepted: 12 August 2021; Paper published: 1 October 2021.

https://doi.org/10.2298/HEMIND210427023K

CC BY NC ND

wet impregnation [14], which is accomplished in two steps: (1) dispersion of the metal precursor onto the support surface and in the interparticle space and (2) thermal activation in order to modify the surface and texture of the raw material [3,15,16].

With the growth of human population, production of agricultural solid waste is on rise [17]. From a circular economy point of view, it is important to support additional uses of low-quality agricultural by-products and turn them into valuable resources, thus supporting cascading of materials as long as possible [18]. Carbonization is commonly used in order to prepare porous biocarbon materials for application in wastewater treatment [19,20]. Recently, Fenton-like application of such materials (fruit shells, straws, *etc*.) was reviewed [21].

One of the possible waste streams that can be used in such manner is soybean hulls. In Serbia, production of soybean is on a constant rise and data show yield of 806407 t in 2020 [22], which ranks Serbia among countries with the highest average yield in Europe. Waste soybean hulls (WSH) account for 7-8 % of the total soybean mass [23,24]. Some of the investigated applications of WSH are: ethanol and bio-oil production, animal feed [24], fermentable sugars [25], cellulose nanofibers [26], cellulose pulp [23], energy source by pyrolysis [27], activated carbon production [28] and adsorption in wastewater treatment [24]. Still, it could be seen that WSH have not been studied as a catalyst support raw material yet.

The focus of this work was to test bio-waste (soybean hulls) value addition as a Fenton catalyst support in the process of RB4 dye decolorization. For this purpose, thermal (carbonization) and chemical (Fe-impregnation) treatments of WSH were performed. Effects of the waste modification were confirmed by using different methods (Brunauer-Emmett-Teller (BET) method, scanning electron microscopy coupled with energy dispersive spectrometry (SEM/EDS), Fourier-transform infrared (FTIR) spectroscopy and X-ray diffraction (XRD) analysis). Optimization of dye decolorization was conducted by using response surface methodology (RSM). Central composite design (CCD) was used to simultaneously investigate effects of selected factors and to interpret the results using a statistical model. Dye degradation products, effluent toxicity, catalyst stability and reusability were monitored.

2. MATERIALS AND METHODS

All chemicals were used as obtained without purification. RB4 (CAS 13324-20-4, dye content ≥35 %, molecular formula: $C_{23}H_{14}Cl_2N_6O_8S_2$), $Fe(NO_3)_3{\cdot}9H_2O$ (≥98 %), Na_2CO_3 (≥99.5 %), H_2O_2 (30 %, w/w), 95–97 % H_2SO_4, catalase from bovine liver (CAS 9001-05-2), methanol (≥99.9 %) were purchased from Sigma-Aldrich (USA). All solutions were prepared with deionized water (DI). WSH were kindly provided by a soybean processing company with the industrial capacity of 250,000 t per year (AP Vojvodina, Serbia). Upon the receipt raw WSH were ground to the 0.3 mm fraction.

2. 1. Catalyst preparation

Two materials were used as Fe-catalyst supports: raw and carbonized WSH. The biowaste carbonization was conducted at 550 °C for 4 h in a muffle furnace with the aim to produce biocarbon (BC).

In our previous work [29] we tested the improved Fe-impregnation method with the use of ultrasound (US) waves in order to shorten the required time for catalyst preparation. In that case, bentonite clay was used as the Fe-support. In the present work, the optimal parameters from this procedure were applied: the Fe^{3+}/material ratio of 3 mmol g^{-1}, the suspension exposure to US waves during impregnation and the calcination temperature of 350 °C Firstly, the support material suspension (1 g in 50 cm^3 DI) was mixed for 30 min. Then, the impregnation precursor (55 cm^3 of 0.2 mol dm^{-3} $Fe(NO_3)_3{\cdot}9H_2O$ solution was mixed with powdered Na_2CO_3 at the molar ratio of $[Na^+]/[Fe^{3+}]=1$) was sonicated for 5 min (20 kHz and 10 % amplitude; Ultrasonic Homogenizer Sonopuls HD 2200, Bandelin, Germany). The processed Fe-precursor was added drop-by-drop to the material suspension and US was applied for 10 min. The impregnated WSH or BC were dried in a water bath (100 °C) and washed several times with DI water. After drying and calcination (350 °C, 2 h), the samples were labeled as Fe-WSH and Fe-BC.

2. 2. Characterization methods

WSH, BC, Fe-WSH and Fe-BC were subjected to the structural analysis by the Autosorb iQ Surface Area Analyzer (Quantachrome Instruments, USA), after sample degassing (105 °C). Specifically, the multi-point BET (Brunauer-Emmett-

Teller) method was used for determination of the specific surface area; BJH (Barrett-Joyner-Halenda), HK (Horvath-Kawazoe) and total pore volume (TPV) methods were used for determination of pore volume and size measurements (average pore radius, APR). Scanning electron microscopy (SEM) (TM3030, Hitachi High-Technologies, Japan) coupled with energy dispersive spectrometry (EDS) (Bruker Quantax 70 X-ray detector system, Bruker Nano, Germany) was used for the morphological analysis. The KBr pellet method was used for Fourier Transform infrared spectroscopy (FTIR) at a Thermo-Nicolet Nexus 670 spectrophotometer (USA) (4000-400 cm^{-1} range in a diffuse reflection mode at a 4 cm^{-1} resolution). A Rigaku MiniFlex 600 (USA) diffractometer with CuKα radiation (scanning range was $5 < 2\theta < 80°$ with 0.03° step) was used for X-ray diffraction analysis.

2. 3. Heterogeneous Fenton process

Control experiments of WSH, BC, Fe-WSH and Fe-BC application in sorption and the heterogeneous Fenton process were conducted under the following conditions: 100 mg of the prepared material was added to 100 cm^3 of RB4 solution (50 mg dm^{-3}). pH value was set to 3 with the use of diluted H_2SO_4 (WTW inoLab pH/ION 735, Germany). The Fenton reaction was initiated with 10 mM H_2O_2 (in sorption tests this step was left out). After 180 min of reaction, the mixture was filtered through a 0.45 μm membrane filter. Decolorization efficiency was determined by using a UV-Vis spectrophotometer (UV-1800, Shimadzu, Japan) at λ_{max}=597.5 nm. Stability of the materials was monitored by inductively coupled plasma-mass spectrometry (ICP-MS; Agilent Technology, Japan) as the total Fe content leached in the aqueous phase (EPA 6020B).

Central composite design (CCD) was employed to investigate decolorization efficiency as a response to 3 independent factor variations (Design-Expert 12 software-trial version; Stat-Ease Inc., USA). Examined variable ranges were selected based on literature review [6, 16, 30], and are presented in Table 1. 20 probe runs were created, including 6 replications of central levels. Analysis of variance (ANOVA) was used for further statistical analysis to identify interactions between selected variables and the response. Verification of the chosen model and optimal reaction conditions was performed by 5 confirmation runs.

Table 1. Experimental conditions and levels of independent variables ($c_{H_2O_2}$ - H_2O_2 concentration, $m_{catalyst}$ - catalyst mass, t – reaction time) according to CCD

Code	Variable	Level (α)				
		-α	-1	0	+1	+α
A	$c_{H_2O_2}$ / mM	0.6	3.0	6.5	10.0	12.4
B	$m_{catalyst}$ / mg	33	50	75	100	117
C	*t* / min	19	60	120	180	221

The optimal setting for the heterogeneous Fenton reaction was used for further kinetics analysis (0; 15; 30; 45; 60; 80; 100; 120; 150; 180 min). Decolorization efficacy and content of leached Fe were determined according to before mentioned procedures. Degree of RB4 mineralization was measured as the total organic carbon (TOC, LiquiTOC Elementar II, Japan) according to EPA 415.3 method. Evaluation of inhibitory effect on *Vibrio fischeri* bacteria (LUMIStox 300, Dr Lange, Germany; ISO 11348-1:2008) was conducted with freshly prepared bacteria suspension and after scavenging residual H_2O_2 by catalase solution [31] in all samples. NaCl was added in order to reach 20 g dm^{-3}, pH value (6.5-8) and concentration of dissolved O_2 (>3 mg dm^{-3}) were measured before testing. Sample inhibition was calculated from the luminescence intensity before and after sample addition to *V. fischeri* suspension. The impact of $^{\bullet}OH$ on the reaction efficiency was determined in the test with methanol as a radical scavenger (0.1 M MeOH was added before oxidant). Also, $^{\bullet}OH$ scavenging capacity (RSC) was measured according to the modified method reported in literature [32], after 15 min of reaction. Degradation products were analyzed by gas chromatography–mass spectrometry (GC-MS, Agilent 7890A/5975C, Japan), where EPA 3510C method was used for sample preparation and the manufacturer's method for determination of non- and semi-polar compounds. The reusability test was conducted 5 times under optimal reaction conditions (catalyst was washed with DI and dried (105 °C) after each use).

CC BY NC ND

3. RESULTS AND DISCUSSION

3. 1. Characterization study

Characterization of surface characteristics of both impregnated as well as the initial support materials was conducted by conventional methods to evaluate differences based on the modification path and future application possibilities.

BET method was employed for an indication of changes in textural features (Table 2). Low values of the surface area and the total pore volume as well as high average pore radius are obtained for WSH, which was expected due to the macroporous hulls nature. Balint *et al.,* [33] have indicated that carbonization and impregnation processes lead to an increase in porosity as a result of decomposition of the WSH cellular structure. Similar results were obtained in the present study. An increase in the surface area of biocarbon was observed from 0.3 to 11 m^2 g^{-1}. The impregnation process had further pronounced effect on micro- and mesopore volume, where a significant TPV rise, and APR reduction indicate appearance of mesoporous surfaces of the prepared catalysts (Fe-WSH and Fe-BC). The surface area expanded to 55 and 104 m^2 g^{-1}, respectively. The mechanical effect of ultrasound (microjets and shock waves) during modification can be responsible for breakdown of the catalyst support to smaller particles [34]. Thus, a larger surface area is available for $Fe(OH)_3$ precipitation during impregnation. Thermal activation at 350 ^oC had an important part in generating active and mesoporous catalysts, where hematite crystals may be produced.

Table 2. Textural features of investigated materials

Material	Surface area, m^2 g^{-1}	Micropore volume by HK, cm^3 g^{-1}	Mesopore volume by BJH, cm^3 g^{-1}	APR, nm	TPV, cm^3 g^{-1}
WSH	0.3	not detected	0.001	67.10	0.001
BC	11	0.004	0.054	9.76	0.056
Fe-WSH	55	0.022	0.177	6.32	0.174
Fe-BC	104	0.042	0.425	8.00	0.416

Surface topology was investigated by SEM and the obtained micrographs are presented in Figure 1. WSH has clear and well-ordered fibrous hull forms consisting of palisade (the outer epidermal layer of tightly packed macrosclereids) and hourglass cells (the hypodermal layer of osteosclereids with expanded ends). These anatomic hull parts are made of cellulose, hemicellulose and pectin (insoluble carbohydrates) and they are bound together with lignin [23]. The drastic influence of carbonization (Fig. 1b) resulted in a porous, “fluffy” appearance of residual ash. Further, the impregnation process (Fe ions incorporation and thermal activation) led to noticeable morphological changes of both WSH and BC (Figs 1c and d). A high number of irregularly shaped Fe-doped particles appeared on both materials. These aggregates differ in size, where Fe-WSH has generally rough particles of approximately 25 μm in size, while Fe-BC retained similar surface characteristics as biocarbon with many smaller particles. Validation of these strong, visual changes in WSH after modification can be linked with presented data on the increases in the surface area and mesopore volume (Table 2).

Elemental composition was quantified by the EDS method (Fig. 2). High O and C content (~46 wt.%) in WSH was foreseen due to the hull structure (Fig. 1a). Besides, Ca, K and Al (3.6, 3.0 and 1.0 wt.%, respectively) were also detected. Increase in K and Ca fractions, and appearance of Mg, Si, P and S in BC are connected to the main carbonization effect, destruction of organic matter that is followed by the release of gases, as reported in literature [27]. It is assumed, that this is the reason for the decrease in C and O contents after carbonization and thermal treatment in BC, Fe-WSH and Fe-BC samples. Moreover, the main impact of impregnation on WSH was replacement of Ca and K with high Fe content (66.9 wt.%). The simultaneous processes of Fe-(hydr)oxide transformation and WSH decomposition, led to production of a Fe-rich solid catalyst. Further, EDS also indicates successful impregnation of BC samples. The formed Fe-oxide resulted in an increase in Fe (19.5 wt.%) and O (38.4 wt.%) contents in Fe-BC. The difference in Fe contents after impregnation can relate to the porosity and average pore radius in support materials (Table 2). Namely, Fe diffusion during ultrasound impregnation was conditioned by the microporous WSH structure and mesopore enriched structure of BC. Additionally, the C percentage has risen to 9.0 wt.% after another thermal treatment of Fe-BC, which may be related to possible char production [33]. Ash like composition of Fe-BC (Fig. 1d) is partially preserved (Ca = 25; Mg = 4.0; Al, Si, P and K < 2 wt.%).

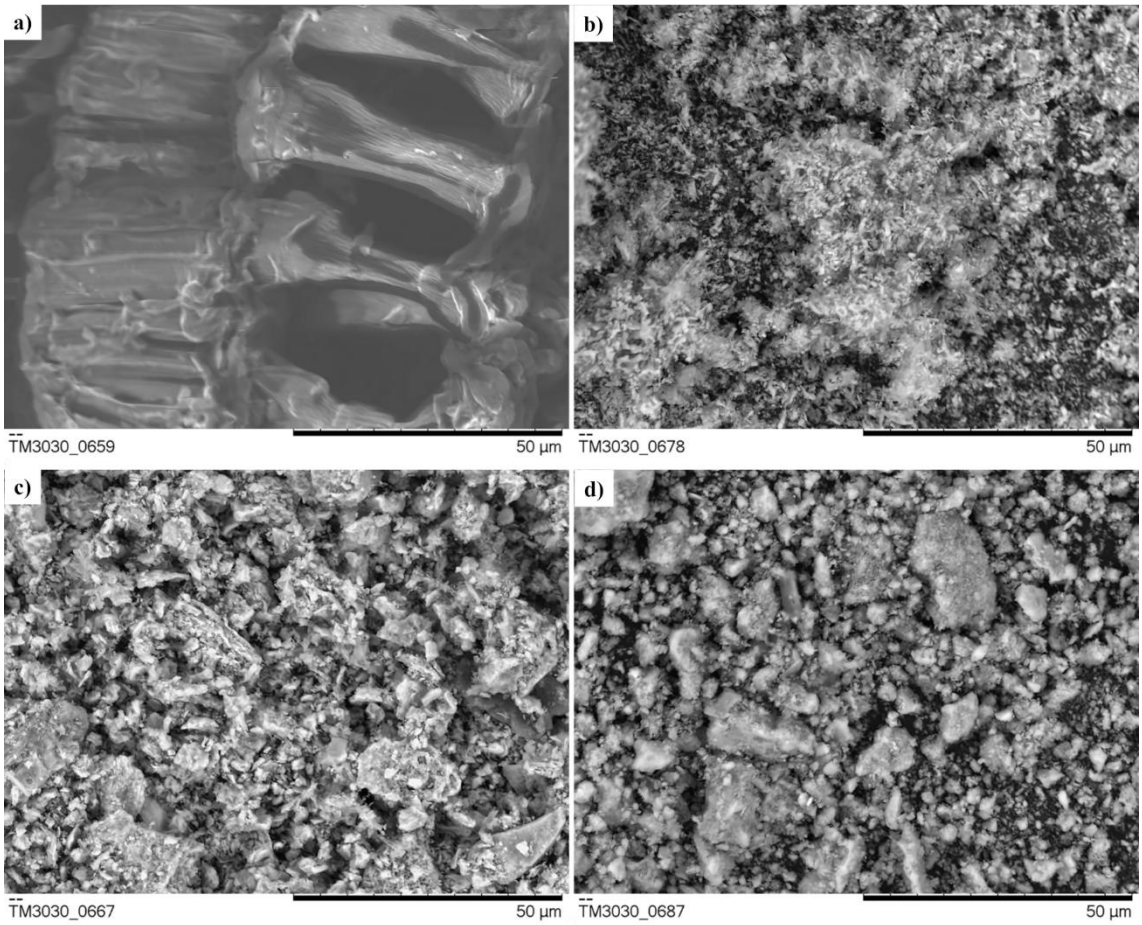

Fig. 1. SEM micrographs of: a) WSH, b) BC, c) Fe-WSH and d) Fe-BC

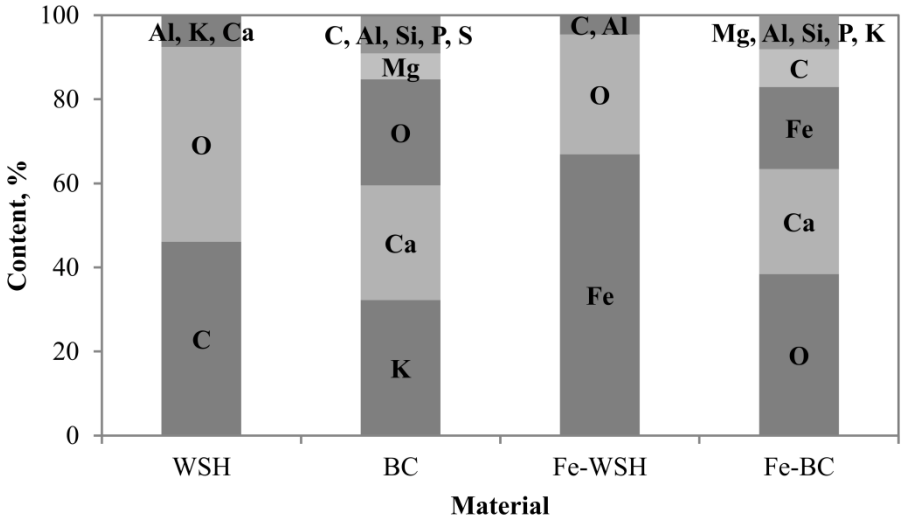

Fig. 2. Elemental composition by the EDS analysis of all investigated materials

Further confirmation of the WSH structure was obtained by the IR spectrum where the highest intensity band (3410 cm^{-1}) represents OH stretching vibrations of cellulose and moisture in the biomass. Also, two peaks at ~2900 cm^{-1} are associated with vibrations of CH and CH_2 asymmetrical stretching in hemicellulose. The peak at 1739 cm^{-1} is attributed to acetyl ester groups in hemicellulose and/or phenyl ester group between lignin and hemicellulose. Besides, the lignin aromatic ring (C=C) stretching is associated with 1645 cm^{-1} peak and CO stretching of cellulose (1035 cm^{-1})

CC BY NC ND

[26]. Carbonization induced lower BC surface functionality. The most prominent band is assigned to carbonate ion and has two peaks at 1460 and 876 cm^{-1} [35], which is in accordance with the obtained ash like surface (Fig. 1b and Fig. 2). When comparing to WSH, the reduction in intensity and small shift of peaks associated with OH (3440 cm^{-1}), CH, CH_2 (2916, 2850 cm^{-1}) and CO stretching (1057 cm^{-1}) are identified. WSH impregnation (Fe-WSH) leads to a significant increase in Fe content (Fig. 2) that produced two, strong intensity peaks of characteristic FeO stretching vibration (544, 453 cm^{-1}). OH (3404 cm^{-1}), C=C (1629 cm^{-1}) and CO (1049 cm^{-1}) vibrations are also present, but as less notable peaks. IR spectra of Fe-BC, additionally indicates the increase in the biocarbon yield shown by SEM/EDS, where carbonate ion peaks are prominent (1456, 874 cm^{-1}). CO stretching (1054 cm^{-1}) and OH vibrations (3427 cm^{-1}) have a higher intensity than the initial support (BC). While comparing impregnated materials, broad, medium intense absorption in the range 550-400 cm^{-1} could be assigned to FeO vibration. The difference between Fe-BC and Fe-WSH peak intensity in this IR region, further confirm the impregnation process outcome (EDS; Fig. 2).

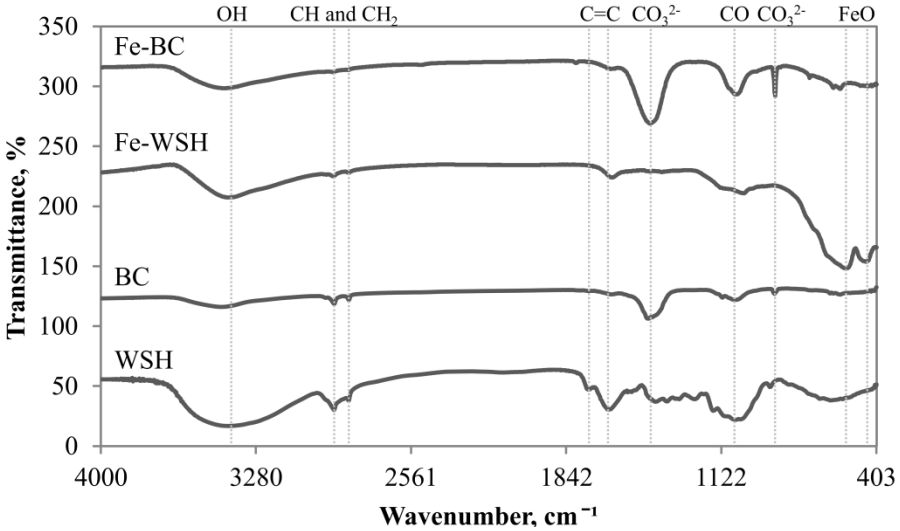

Fig. 3. FTIR spectra of all investigated materials with characteristic functional groups

XRD diffractogram profiles are shown in Figure 4. WSH shows a semicrystalline pattern with one crystalline peak (2 θ = 34.6°) and broad, amorphous humps (2 θ = 13-25°). Namely, peaks at 2θ = 17.3°, 20.5°, 22.3° and 34.6° are typical for type I cellulose, which is the most abundant native crystalline polymorph form [24]. With either modification (BC, Fe-WSH, Fe-BC), a semicrystalline pattern of WSH becomes crystalline due to the breakage of amorphous hull fractions (cellulose, hemicellulose). BC diffractogram shows many peaks, related to $CaCO_3$ (PDF 00-005-0586; 2 θ = 23.1, 29.4, 36.1, 39.4, 42.9, 47.4, 48.5 and 60.5°), Al_2O_3 (PDF 00-010-0173; 2θ = 25.9, 35.3 and 41.6) and SiO_2 (PDF 00-046-1045; 2θ = 26.5, 40.3 and 50.3°) while the peak with the highest intensity at 27.9° was due to fairchildite mineral ($K_2Ca(CO_3)_2$; PDF 00-900-8300; 2θ = 13.2, 19.4, 33.9, 44.4 and 48.1°). Diffraction peaks found after impregnation (Fe-WSH) correspond to hematite (PDF 00-033-0664), at angles 2θ = 24.2, 33.2, 35.7, 40.9, 49.5, 54.1, 62.7 and 64.0°. The same phase was detected in Fe-BC, with a slightly shifted peak (2θ = 32.7°), while the rest of the pattern is linked to $CaCO_3$ already identified as the main phase in carbonized WSH. In our work, both impregnated materials show crystalline patterns in contrary to the results reported by Chen *et al.,* [36], where corn husk retained amorphous pattern after similar processes. The average Fe_2O_3 crystal size was 26.2 nm (Fe-WSH) and 23.8 nm (Fe-BC) based on the Scherrer's formula [37], that confirms the thermal transformation of Fe-hydroxide to oxide at 350 °C.

All applied methods induced significant changes in surface morphology and chemistry after WSH modification. According to BET and SEM data, the surface area and porosity significantly expanded, while the other characterization methods confirmed the presence of Fe after impregnation. Namely, the retained ash like structure and increased surface area of Fe-BC, provide a basis for application of this material in the sorption process. On the other hand, Fe-WSH has the potential to be used as a Fenton reaction catalyst due to high Fe content. These assumptions are important for subsequent dye solution treatment.

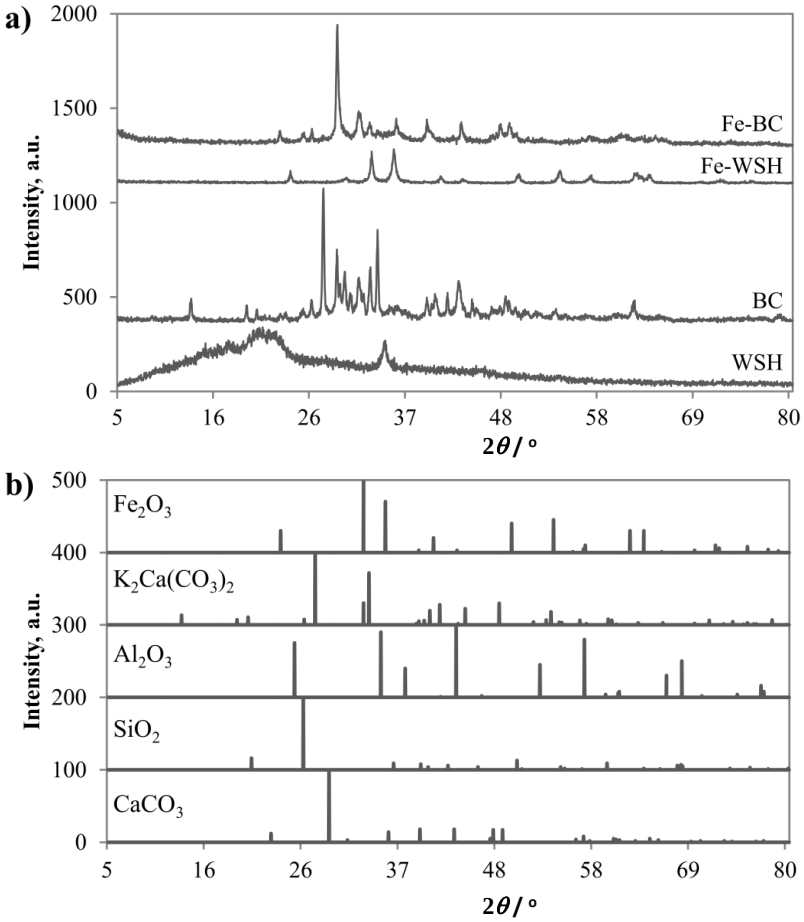

Fig. 4. XRD analysis: a) XRD diffractogram of four materials and b) PDF card peak patterns

3. 2. Application of biocarbon materials in dye decolorization

In order to understand decolorization of RB4 by the heterogeneous Fenton process using modified soybean hull biocarbon samples, control experiments were conducted (Fig. 5). A series of tests were performed at a pH 3 as optimal for the Fenton reaction. It is important to indicate that RB4 is anionic in nature in either acidic or alkaline medium [38].

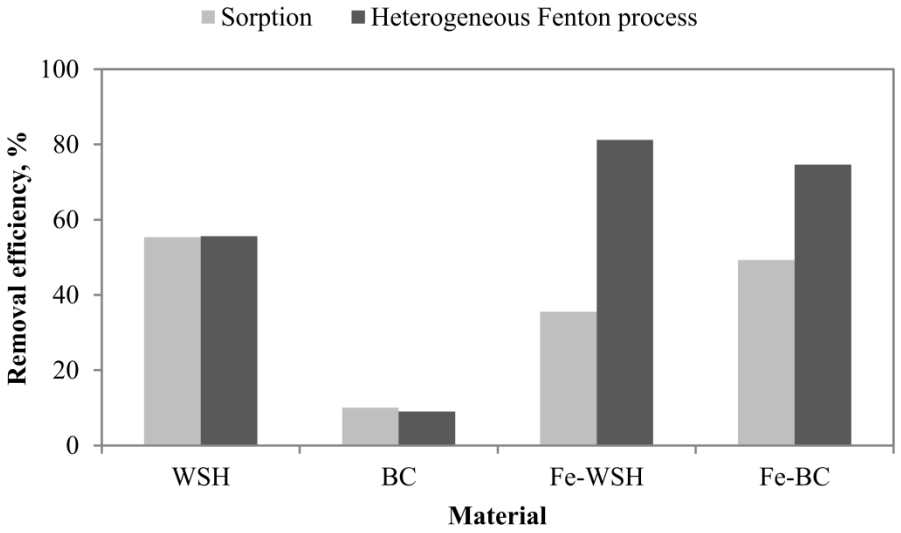

Fig. 5. Control experiments (adsorption and oxidation of RB4 dye solution) with the investigated materials. Reaction conditions: c_{RB4} = 50 mg dm^{-3}; V_{RB4} = 100 cm^{-3}; pH 3; $m_{material}$ = 100 mg; $c_{H_2O_2}$ = 10 mM.

CC BY NC ND

In both, sorption and Fenton processes, WSH exhibited a moderate RB4 removal, probably due to macroporosity and Fe absence. The carbonized material (BC) had the lowest activity, even though it had the increased surface area. The presence of Ca, K, Mg, Al (proved by EDS, XRD), may induce the alkaline surface as oxides of these metals are known strong bases [36]. After the pH adjustment, significant change in net surface charge is possible and therefore electrostatic repulsion of RB4 molecules is occurring. The presented BC nature and absence of transition metals, able to initiate the Fenton reaction, are the reason for the obtained RB4 removal of only 10 %.

In comparison to BC, dye sorption was improved with Fe-WSH and Fe-BC. It is assumed that the higher Fe content in Fe-WSH may be associated to the presence of many positively charged sites, able to electrostatically attract RB4 as compared to Fe-BC. Since the presence of Fe species was confirmed, the increased activity of impregnated catalysts in the Fenton process was not surprising. Namely, 81.3 and 74.7 % dye was removed with Fe-WSH and Fe-BC, respectively. The reason is the reaction between $\equiv Fe_2O_3$ and adsorbed H_2O_2. Electronic transfer results in the ferric complex ($\equiv Fe\text{-}OOH^{2+}$) formation and its further decomposition to $^{\bullet}OOH$ and $\equiv Fe^{2+}$, that leads to production of desired $^{\bullet}OH$ radicals [3, 39]. Additionally, the material stability is also an important factor. Measured Fe leaching varied depending on the applied material and type of the process. During the dye sorption test, 0.77 mg dm^{-3} (Fe-WSH) and 0.64 mg dm^{-3} (Fe-BC) of total Fe was detected in solution due to favored reaction between $\equiv Fe_2O_3$ and H^+ under acidic conditions. In the Fenton process, H_2O_2 decomposition results in higher catalyst stability, where Fe-WSH shows a lower leaching potential (0.13 mg dm^{-3}) than Fe-BC (0.39 mg dm^{-3}).

Given the importance of the efficiency of the material preparation method (required time, energy consumption) and the effectiveness of the Fenton process (percentage of the removed dye, catalyst stability), further optimization study of RB4 decolorization process was performed with Fe-WSH.

3. 3. Fe-WSH in the Fenton process – RSM optimization study

RSM was implemented to optimize *A* - $c_{H_2O_2}$, *B* - $m_{Fe\text{-}WSH}$ and *C* - reaction time to obtain a satisfying RB4 decolorization efficiency. The CCD matrix (factorial, *central*, **star** points) and removal efficiencies are presented in Table 3. As CCD is used for building a second order model, the backward stepwise regression of a quadratic model (α = 0.1) was implemented to find a reduced model that best explains the results. Adequacy of the reduced model was tested by the analysis of variance (ANOVA) by tests of the significance of regression model with individual model coefficients and lack of fit test.

Table 3. CCD design matrix and experimental results

Standard order	Run order	Factor *A* $c_{H_2O_2}$ / mM	Factor *B* $m_{Fe\text{-}WSH}$ / mg	Factor *C* *t* / min	Efficiency, %	
					Actual response	Predicted response
15	1	6.5	75	120	70.7	62.6
8	2	10.0	100	180	79.5	80.6
16	3	6.5	75	120	62.5	62.6
9	**4**	0.6	75	120	70.5	66.9
4	5	10.0	100	60	67.0	66.4
3	6	3.0	100	60	75.3	71.5
5	7	3.0	50	180	55.7	58.8
11	**8**	6.5	33	120	40.1	40.1
14	**9**	6.5	75	221	75.9	74.5
6	10	10.0	50	180	52.0	53.7
20	*11*	6.5	75	120	59.9	62.6
12	**12**	6.5	117	120	82.1	85.2
10	**13**	12.4	75	120	58.8	58.3
19	*14*	6.5	75	120	61.4	62.6
2	15	10.0	50	60	39.8	39.6
17	*16*	6.5	75	120	66.8	62.6
7	17	3.0	100	180	80.4	85.7
13	**18**	6.5	75	19	44.0	50.7
1	19	3.0	50	60	42.3	44.7
18	*20*	6.5	75	120	67.6	62.6

ANOVA, the fit and model comparison statistics and final equation provided by the backward elimination for decolorization prediction (in coded factors) are shown in Table 4. The results show the model significance (p-value <0.05) with the main, linear effects of A, B and C, while the two-level interaction and second-order effects are not significant (p-value >0.1). p-values for these coefficients were: C^2 = 0.1138, B^2 = 0.1734, BC = 0.4554, AC = 0.5667, AB = 0.8018 and A^2 = 0.9213. It was found that both m(Fe-WSH) and reaction time were the most significant factors for the RB4 decolorization. Obtained R^2 value (0.9289) is high, and indicates that the 92.9 % of the data variability is explained by the reduced model. Variation of the predicted data shown as the predicted R^2 (0.8937) is in good agreement with the adjusted R^2 (presents variation of the experimental data). High values of R^2, adjusted R^2 and predicted R^2 ~0.9 also indicate validation of the model. Additionally, the adequate precision value measures the range of the predicted data to the average prediction error. The desirable signal to noise ratio is larger than 4 with the adequate precision of 26.2 obtained with the reduced model indicates an adequate signal.

Table 4. ANOVA results for reduced central composite design, fit and model comparison statistics and final equation in terms of coded factors

Source	Sum of squares	df	Mean square	*F*-value	*p*-value	
Model	3232	3	1077	69.67	<0.0001	significant
A	89.34	1	89.34	5.778	0.0287	
B	2458	1	2458	159.0	<0.0001	
C	684.6	1	684.6	44.27	<0.0001	
Residual	247.4	16	15.46			
Lack of Fit	159.7	11	14.52	0.828	0.6330	not significant
Pure Error	87.72	5	17.54			
Cor Total	3479	19				
Std. Dev.	3.932		R^2	0.9289		
Mean	62.61		Adjusted R^2	0.9156		
Coefficient of Variance	6.280		Predicted R^2	0.8937		
			Adeq. Precision	26.22		
Decolorization efficiency, % = 62.61 - 2.56 *A* + 13.42 *B* + 7.08 *C*						

The main diagnostics plot is the normal probability of residuals (Fig. 6a), which reveals that errors are distributed normally and that there is a straight-line pattern of residuals. This finding supports the adequacy of the least-squares fit, which indicates the use of the proposed model for heterogeneous Fenton process optimization.

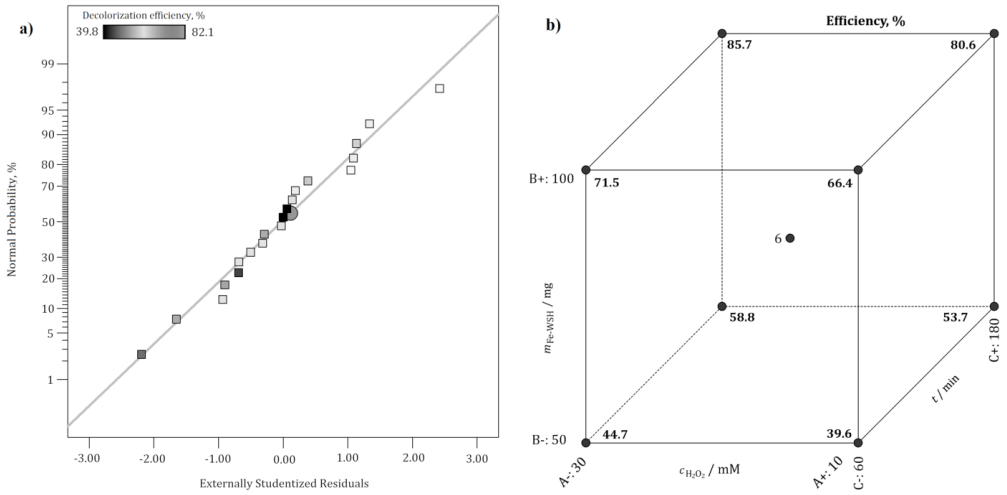

Fig 6. Diagnostic plot: a) normal probability vs. externally studentized residuals; Model graph: b) cube plot of predicted decolorization efficiency (A-left and right; B-up and down; C-front and back faces)

The cube plot (Fig. 6b) displays the three investigated factors variation outcomes in one place. Axes present three factors from in the range from low to high and coordinate points are predicted dye removals of factorial probes (Table 3). Oxidant concentration is an important factor for treatment efficacy [3,7,9] and the RSM analysis indicated that the

CC BY NC ND

lowest H_2O_2 concentration was optimal. It is assumed that reaction between 3 mM H_2O_2 and 100 mg Fe-WSH provided an adequate amount of •OH radicals for RB4 decolorization (85.7 %). Higher oxidant amounts reduced the process efficiency, due to production of less active hydroperoxylic radicals (•OOH) and H_2O [30]. Similar outcome was observed in literature [40] in the Fenton reaction between pyrite ash and RB4 dye, where 99.5 % removal was achieved with the initial H_2O_2 concentration of 4 mM. Moreover, the influence of Fe-WSH dose is important and beneficial for dye removal by heterogeneous Fenton reaction. Due to the catalyst increased dose and generally high surface area, mesoporosity and hematite crystals as active sites, adsorption and catalytic decomposition of H_2O_2 can occur simultaneously thus positively affecting treatment outcome. In a review paper on factors that affect catalytic activity the reaction time was stressed as an important parameter for achieving complete dye degradation [10]. Prolonged operation provides sufficient time for heterogeneous Fenton reagents to react. The reaction time has a positive and linear effect, where RB4 decolorization efficiency increased as the reaction time increased from 19 to 221 min (Table 3).

Overall, the desired goal of RSM was to optimize the RB4 decolorization efficiency. The predicted removal was 85.7 % and desirability function 0.762. The optimal reaction conditions were: 3 mM H_2O_2, 100 mg Fe-WSH, and reaction time of 180 min. The model verification test confirmed good correlation with the observed decolorization efficiency 85.2 % (mean value) with low standard deviation (1.8 %) in 5 consecutive runs.

3. 4. Evolution of RB4 mineralization

Heterogeneous Fenton optimal conditions were kept constant in the period from 5-180 min for determination of the reaction kinetics. Results depicted in Figure 7 show RB4 removal and mineralization, together with methanol •OH scavenging and *Vibrio fischeri* inhibition of the effluent during the reaction.

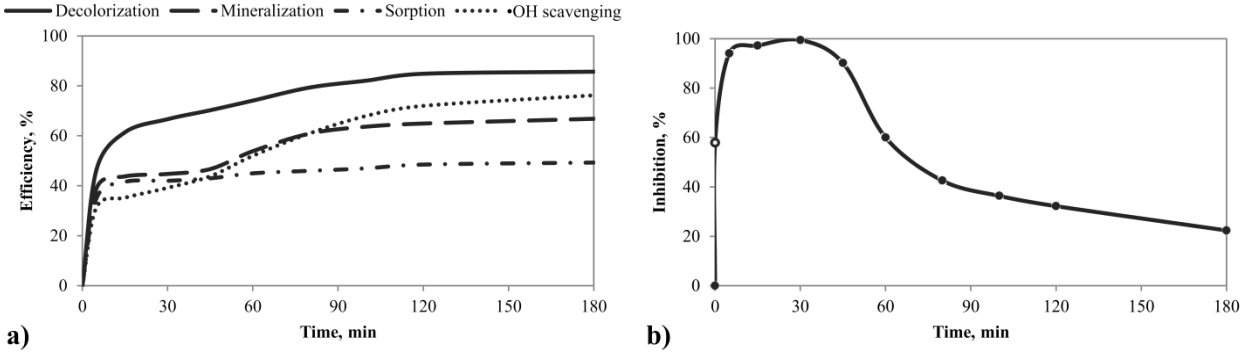

Fig. 7. Kinetics of RB4 oxidation: a) heterogeneous Fenton process performance and b) effluent acute toxicity on V. fischeri bacteria. Reaction conditions: c_{RB4}=50 mg dm^{-3}; V_{RB4}=100 cm^3; pH 3; $m_{material}$=100 mg; $c_{H_2O_2}$ = 3 mM

The highest rise in RB4 decolorization efficiency was detected in the first 15 min (from 46.6 to 61.4 %) with an intensifying effect up to 100 min (Fig. 7a). Reduction of Fe^{3+} by H_2O_2 happens during Fenton reaction initiation steps [11], which induces production •OH radicals. In the period from 100 to 180 min the reaction rate is slower and proceeds at a steady level, which is common for heterogeneous Fenton reaction propagation and termination steps. Dye mineralization had a similar trend, where TOC removal increases over the period up to 80 min, while afterwards the reaction proceeds slowly (66.8 %). The difference in observed RB4 decolorization and mineralization is due to different reaction pathways. Additionally, dye sorption was generally steady and in the range from 35.1 to 49.3 %, pointing to the significance of the Fenton reaction. When methanol was added as an •OH scavenger, ~50 % lower efficacy was obtained in the first 30 min. As the reaction proceeds, it is suspected that new radical species are formed [41], which further affect dye decolorization. The •OH radical scavenging test was also implemented to determine •OH radicals presence after 15 min, as it was assumed that the highest amount of radical species arises at that time. The identified capacity of 79.6 %, additionally confirms the Fenton reaction.

Finally, the acute toxicity test on *V. fischeri* bacteria was conducted (Fig. 7b) for all samples in the determined time range. The starting inhibition of the RB4 solution was 57.9 % (white point in the graph). The inhibition curve shows that RB4 intermediates are the most toxic in the first phase of the reaction (90.2 % up to 45 min). Afterwards, inhibition

greatly decreases to 22.4 % (180 min), thus presenting low toxicity to the non-selective bacteria. In a previous work [6], RB4 effluent after the Fenton process induced high toxicity (>95 %) due to detected polycyclic hydrocarbons and compounds that contained Cl atoms as degradation intermediates. It is assumed that similar compounds (with the inhibitory potential) are formed in the first 60 min, while during further reaction these compounds are degraded thus ensuring the sufficient effluent quality.

Under the optimal heterogeneous Fenton reaction conditions RB4 degradation products were analyzed by the GC-MS technique and detected compounds are presented in Table 5. Cyclic hydrocarbons, phthalates, organic acids and its esters, an organonitrogen compound, phenols and alcohols were identified by the NIST and AMDIS databases. It can be seen that the initial oxidation product of RB4 dye (1-amino-9,10-anthracenedione) was not found, which may be the evidence of molecule chromophore degradation by •OH radicals to phthalates, phenols and organic acids [2,42]. Also, triazine compounds were not found, thus confirming dye mineralization during the reaction time.

Table 5. GC-MS list of degradation products

Retention time, min	CAS number	Compound Name	Molecular formula
5.63	91203	Naphthalene	$C_{10}H_8$
8.58	112425	1-Undecanol	$C_{11}H_{24}O$
9.07	96764	Phenol, 2,4-bis(1,1-dimethylethyl)-	$C_{14}H_{22}O$
9.38	90437	o-Hydroxybiphenyl	$C_{12}H_{10}O$
15.2	36653824	1-Hexadecanol	$C_{16}H_{34}O$
16.8	84695	1,2-Benzenedicarboxylic acid, bis(2-methylpropyl) ester	$C_{16}H_{22}O_4$
19.5	84742	Dibutyl phthalate	$C_{16}H_{22}O_4$
19.7	57103	n-Hexadecanoic acid	$C_{16}H_{32}O_2$
23.7	129000	Pyrene	$C_{16}H_{10}$
24.3	112629	9-Octadecenoic acid (Z)-, methyl ester	$C_{19}H_{36}O_2$
30.3	117817	Bis(2-ethylhexyl) phthalate	$C_{24}H_{38}O_4$
33.5	0	l-Proline, N-methoxycarbonyl-, heptadecyl ester	$C_{24}H_{45}NO_4$

3. 5. Fe-WSH reusability

Fe-WSH stability is expressed as a content of leached Fe. Under the optimal Fenton reaction conditions and during the first 60 min, only 0.11 mg Fe dm^{-3} was detected in the aqueous phase. Until 180 min, 0.13 mg dm^{-3} in total was leached amounting to only 0.02 % of the total Fe amount in the system (66.9 mg Fe for 100 mg Fe-WSH, value obtained according to EDS analysis; Fig. 2), thus providing an insight in the high catalyst stability.

Additionally, a reusability test was performed (Fig. 8).

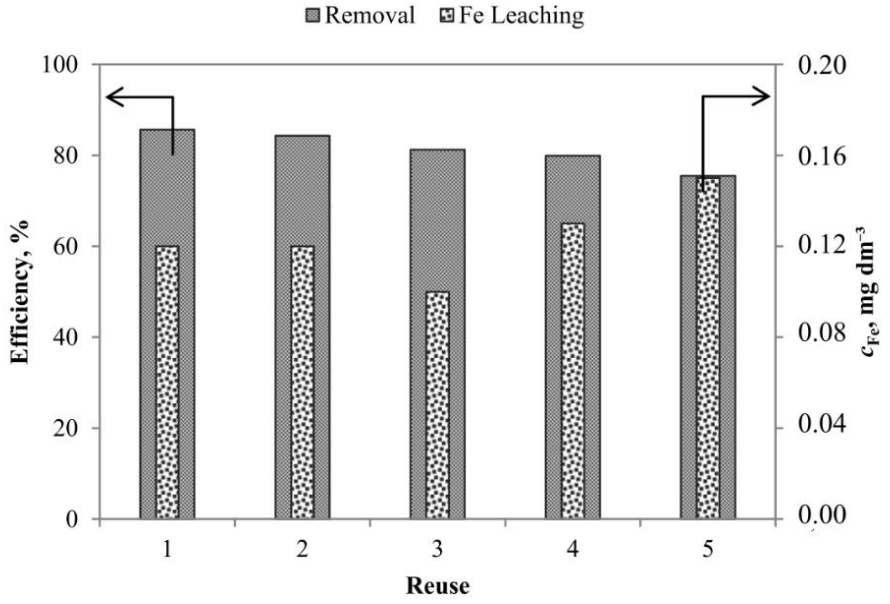

Fig. 8. Fe-WSH reusability test

CC BY NC ND

The Fe-WSH activity loss over 5 runs was ~12 % (1^{st} = 85.7; 5^{th} = 75.5 %), while the total Fe leaching was constant (up to 0.15 mg dm^{-3}). These results suggest that the catalyst has high physical-chemical stability. The reason for the observed efficiency reduction is due to possible adsorption of the dye and its intermediates, which were not completely removed by washing with DI water and at low temperature treatment. All presented results indicate that Fe-WSH is appropriate for effective synthetic dye degradation with long-term stability in acidic conditions.

4. CONCLUSION

In the present work, waste soybean hulls (WSH) were investigated as a Fe-support in two forms: raw and carbonized in order to contribute to agricultural solid waste value-addition. Facile ultrasound improved impregnation was implemented in order to produce heterogeneous Fenton catalyst for dye degradation. Characterization of the initial and obtained materials demonstrated increase in the specific surface area due to decomposition of WSH constituents during carbonization in order to obtain biocarbon (BC) and during further thermal activation and impregnation to obtain Fe-enriched materials (*i.e*. Fe-WSH and Fe-BC), thus producing catalysts with high mesoporosity and hematite as active sites for Fenton reaction. Among the investigated materials, BC could be used as an adsorbent in alkaline media, while Fe-WSH showed greater ability for •OH production in acidic conditions. Next, the heterogeneous Fenton reaction conditions were optimized by using the RSM and CCD experiment design. The following reaction conditions were indicated by the reduced model: 3 mM H_2O_2, 100 mg Fe-WSH and the reaction time of 180 min, at constant pH 3, the RB4 concentration of 50 mg dm^{-3} and at room temperature. The achieved dye removal and mineralization were 85.7 and 66.8 %, respectively, while the Fe-WSH catalyst showed high stability and reaction intermediates formed during the oxidation process had a low inhibitory effect on *Vibrio fischeri* bacteria. Lower oxidant demand and the possibilities for the catalyst reuse make the treatment more economical. For future use of the heterogeneous Fenton process in industrial wastewater treatment it is important to achieve the environmentally safe effluent with low toxicity and organic and inorganic loads. Likewise, cascading use of waste-originating catalysts (in wastewater treatment, construction, agriculture, etc.) should be enforced in design of circular economy systems.

Acknowledgements: The authors acknowledge the financial support of the Ministry of Education, Science and Technological Development of the Republic of Serbia [Grant No. 451-03-68/2020-14/200125] and the Science Fund of the Republic of Serbia [PROMIS – WasteWaterForce project (6066881)]. The authors also kindly thank a soybean processing company for providing raw SBH, PhD Goran Kitić and PhD Jovana Stanojev (Biosense Institute) for SEM/EDS analyses, PhD Srđan Rakić (Faculty of Sciences) for XRD analyses, and PhD Branko Kordić (Faculty of Sciences) for FTIR analyses.

REFERENCES

[1] Holkar CR, Jadhav AJ, Pinjari DV, Mahamuni NM, Pandit AB. A critical review on textile wastewater treatments: Possible approaches. *J. Environ. Manage.* 2016; 182: 351–366. https://dx.doi.org/10.1016/j.jenvman.2016.07.090

[2] Gözmen B, Kayan B, Gizir M, Heresnov A. Oxidative degradations of reactive blue 4 dye by different advanced oxidation methods. *J. Hazard. Mater.* 2009; 168: 129–136. https://dx.doi.org/10.1016/j.jhazmat.2009.02.011

[3] Hassan H, Hameed BH. Fe-Natural Zeolite as Highly Active Heterogeneous Catalyst in Decolorization of Reactive Blue 4. *Int. J. Environ. Sci. Dev.* 2020; 11: 133–137. https://dx.doi.org/10.18178/ijesd.2020.11.3.1239

[4] Fatma NY, Riyanti F, Hariani PL, Nurbaiti B. Synthesis of chitosan/alumina composite by sol gel method for adsorption of procion blue MX-R dye from wastewater songket industry. *J. Phys. Conf. Ser.* 2019; 1282: 012080. https://doi.org/10.1088/1742-6596/1282/1/012080

[5] da Silva RG, de Andrade AR. Degradation of the Dye Reactive Blue 4 by Coupled Photoassisted Electrochemistry at DSA®-Type Electrode. *J. Brazil. Chem. Soc.* 2016; 27: 857–865. http://dx.doi.org/10.5935/0103-5053.20150338

[6] Tomin MB, Kulic A, Kerkez D, Prica M, Rapajic S, Pilipovic DT, Pesic V. Reactive dye degradation using Fe-loaded bentonite as a Fenton-like catalyst: From process optimization to effluent acute toxicity. *Fresen. Environ. Bull.* 2017; 26: 8184–8198. https://www.prt-parlar.de/download_feb_2017/

[7] Zhang M, Dong H, Zhao L, Wang D, Meng D. A review on Fenton process for organic wastewater treatment based on optimization perspective. *Sci. Total Environ.* 2019; 670: 110–121. https://dx.doi.org/10.1016/j.scitotenv.2019.03.180

[8] Eloussaief M, Hamza W, Ghorbali G, Kallel N, Benzina M. Fe-Rich Aragonite Concretion Applied to Industrial Dye Purification Using Fenton and Photo-Fenton Technologies. *Waste Biomass Valori.* 2021; 12: 3303-3313. https://dx.doi.org/10.1007/s12649-020-01228-6

[9] Wang N, Zheng T, Zhang G, Wang P. A review on Fenton-like processes for organic wastewater treatment. *J. Environ. Chem. Eng.* 2016; 4: 762–787. https://dx.doi.org/10.1016/j.jece.2015.12.016

[10] Javaid R, Qazi UY. Catalytic oxidation process for the degradation of synthetic dyes: An overview. *Int. J. Environ. Res. Public Health.* 2019; 16: 2066. https://dx.doi.org/10.3390/ijerph16112066

[11] Zhu Y, Zhu R, Xi Y, Zhu J, Zhu G, He H. Strategies for enhancing the heterogeneous Fenton catalytic reactivity: A review. *Appl. Catal. B Environ.* 2019; 255: 117739. https://doi.org/10.1016/j.apcatb.2019.05.041

[12] Bello M, Raman AA, Asghar A. A review on approaches for addressing the limitations of Fenton oxidation for recalcitrant wastewater treatment. *Process Saf. Environ. Prot.* 2019; 126: 119-140. https://doi.org/10.1016/j.psep.2019.03.028

[13] Nidheesh PV. Heterogeneous Fenton catalysts for the abatement of organic pollutants from aqueous solution: A review. *RSC Adv.* 2015; 5: 40552–40577. https://dx.doi.org/10.1039/c5ra02023a

[14] Wang J, Bai Z. Fe-based catalysts for heterogeneous catalytic ozonation of emerging contaminants in water and wastewater. *Chem. Eng. J.* 2017; 312: 79–98. https://dx.doi.org/10.1016/j.cej.2016.11.118

[15] Girish CR. Various impregnation methods used for the surface modification of the adsorbent: A review. *Int. J. Eng. Technol.* 2018; 7: 330–334. https://dx.doi.org/10.14419/ijet.v7i4.7.20571

[16] Elías VR, Rodriguez PAO, Vaschetto EG, Pecchi GA, Huck-Iriart C, Casuscelli SG, Eimer GA. Tailoring the stability and photo-Fenton activity of Fe-modified nanostructured silicates by tuning the metal speciation from different synthesis conditions. *Mol. Catal.* 2020; 481: 110217. https://dx.doi.org/10.1016/j.mcat.2018.10.012

[17] Setiawan WK, Chiang KY. Crop Residues as Potential Sustainable Precursors for Developing Silica Materials: A Review. *Waste Biomass Valori.* 2020; 2207-2236. https://dx.doi.org/10.1007/s12649-020-01126-x

[18] Campbell-Johnston K, Vermeulen WJV, Reike D, Brullot S. The Circular Economy and Cascading: Towards a Framework. *Resour. Conserv. Recycl. X.* 2020; 7: 100038. https://dx.doi.org/10.1016/j.rcrx.2020.100038

[19] Xiang W, Zhang X, Chen J, Zou W, He F, Hu X, Tsang DCW, Ok YS, Gao B. Biochar technology in wastewater treatment: A critical review. *Chemosphere.* 2020; 252: 126539. https://dx.doi.org/10.1016/j.chemosphere.2020.126539

[20] Enaime G, Baçaoui A, Yaacoubi A, Lübken M. Biochar for wastewater treatment-conversion technologies and applications. *Appl. Sci.* 2020; 10: 3492. https://dx.doi.org/10.3390/app10103492

[21] Pan X, Gu Z, Chen W, Li Q. Preparation of biochar and biochar composites and their application in a Fenton-like process for wastewater decontamination: A review. *Sci. Total Environ.* 2021; 754: 142104. https://dx.doi.org/10.1016/j.scitotenv.2020.142104

[22] Statistical Office of the Republic of Serbia. Statistical Release PO16: Realized production of wheat and early fruit and expected yields of late crops, fruit and grapes, 2020. *Agric. Stat.* 2020; 262: 1-2. ISSN 0353-9555

[23] Barros PJR, Ascheri DPR, Santos MLS, Morais CC, Ascheri JLR, Signini R, dos Santos DM, de Campos AJ, Devilla IA. Soybean hulls: Optimization of the pulping and bleaching processes and carboxymethyl cellulose synthesis. *Int. J. Biol. Macromol.* 2020; 144: 208–218. https://dx.doi.org/10.1016/j.ijbiomac.2019.12.074

[24] Liu H-M, Li H-Y. Application and Conversion of Soybean Hulls. In: Kasai M, ed. *Soybean - The Basis of Yield, Biomass and Productivity.* IntechOpen; 2017: 111–132. https://dx.doi.org/10.5772/66744

[25] Qing Q, Guo Q, Zhou L, Gao X, Lu X, Zhang Y. Comparison of alkaline and acid pretreatments for enzymatic hydrolysis of soybean hull and soybean straw to produce fermentable sugars. *Ind. Crops Prod.* 2017; 109: 391–397. https://dx.doi.org/10.1016/j.indcrop.2017.08.051

[26] Neto WPF, Silvério HA, Dantas NO, Pasquini D. Extraction and characterization of cellulose nanocrystals from agro-industrial residue - Soy hulls. *Ind. Crops Prod.* 2013; 42: 480–488. https://dx.doi.org/10.1016/j.indcrop.2012.06.041

[27] Toro-Trochez JL, Carrillo-Pedraza ES, Bustos-Martínez D, García-Mateos FJ, Ruiz-Rosas RR, Rodríguez-Mirasol J, Cordero T. Thermogravimetric characterization and pyrolysis of soybean hulls. *Bioresour. Technol. Reports.* 2019; 6: 183–189. https://dx.doi.org/10.1016/j.biteb.2019.02.009

[28] Herde ZD, Dharmasena R, Sumanasekera G, Tumuluru JS, Satyavolu J. Impact of hydrolysis on surface area and energy storage applications of activated carbons produced from corn fiber and soy hulls. *Carbon Resour. Convers.* 2020; 3: 19–28. https://dx.doi.org/10.1016/j.crcon.2019.12.002

[29] Bečelić-Tomin M, Kulić A, Kerkez Đ, Pilipović DT, Pešić V, Dalmacija B. Synthesis of impregnated bentonite using ultrasound waves for application in the Fenton process. *Clay Miner.* 2018; 53: 203–212. https://dx.doi.org/10.1180/clm.2018.14

[30] Xiao C, Li J, Zhang G. Synthesis of stable burger-like α-Fe2O3 catalysts: Formation mechanism and excellent photo-Fenton catalytic performance. *J. Clean. Prod.* 2018; 180: 550–559. https://dx.doi.org/10.1016/j.jclepro.2018.01.127

[31] Trovó AG, Nogueira RFP, Agüera A, Fernandez-Alba AR, Malato S. Degradation of the antibiotic amoxicillin by photo-Fenton process - Chemical and toxicological assessment. *Water Res.* 2011; 45: 1394–1402. https://dx.doi.org/10.1016/j.watres.2010.10.029

[32] Milidrag GP, Prica M, Kerkez D, Dalmacija B, Kulic A, Pilipovic DT, Tomin MB. A comparative study of the decolorization capacity of the solar-assisted Fenton process using ferrioxalate and Al, Fe-bentonite catalysts in a parabolic trough reactor. *J. Taiwan Inst. Chem. Eng.* 2018; 93: 436–449. https://dx.doi.org/10.1016/j.jtice.2018.08.015

[33] Balint T, Chang BP, Mohanty AK, Misra M. Underutilized Agricultural Co-Product as a Sustainable Biofiller for Polyamide 6,6: Effect of Carbonization Temperature. *Molecules.* 2020; 25: 1455. https://dx.doi.org/doi:10.3390/molecules25061455

[34] Wu Q, Ouyang J, Xie K, Sun L, Wang M, Lin C. Ultrasound-assisted synthesis and visible-light-driven photocatalytic activity of Fe-incorporated TiO_2 nanotube array photocatalysts. *J. Hazard. Mater.* 2012; 199–200: 410–417. https://dx.doi.org/10.1016/j.jhazmat.2011.11.031

[35] Nandiyanto ABD, Oktiani R, Ragadhita R. How to read and interpret ftir spectroscope of organic material. *Indones. J. Sci. Technol.* 2019; 4: 97–118. https://dx.doi.org/10.17509/ijost.v4i1.15806

[36] Chen Y, Shi J, Du Q, Zhang H, Cui Y. Antibiotic removal by agricultural waste biochars with different forms of iron oxide. *RSC Adv.* 2019; 9: 14143–14153. https://dx.doi.org/10.1039/c9ra01271k

[37] Wang QJ, Liu RJ, Shen XQ, Wu DM, Li HH. Fabrication and methyl blue adsorption kinetics of α-Fe2O3 nanotubes by electrospinning. *Adv. Mater. Res.* 2013; 699: 302–307. https://dx.doi.org/10.4028/www.scientific.net/AMR.699.302

[38] Galan J, Trilleras J, Zapata PA, Arana VA, Grande-Tovar CD. Optimization of chitosan glutaraldehyde-cross linked beads for reactive blue 4 anionic dye removal using a surface response methodology. *Life*. 2021; 11: 1–20. https://dx.doi.org/10.3390/life11020085

[39] Zhao L, Lin ZR, Ma XH, Dong, YH. Catalytic activity of different iron oxides: Insight from pollutant degradation and hydroxyl radical formation in heterogeneous Fenton-like systems. *Chem. Eng. J.* 2018; 352: 343–351. https://dx.doi.org/10.1016/j.cej.2018.07.035

[40] Becelic-Tomin M, Dalmacija B, Rajic L, Tomasevic D, Kerkez D, Watson M, Prica M. Degradation of anthraquinone dye reactive blue 4 in pyrite ash catalyzed fenton reaction. *Sci. World J.* 2014; 234654. https://dx.doi.org/10.1155/2014/234654

[41] Schneider JT, Firak DS, Ribeiro RR, Peralta-Zamora P. Use of scavenger agents in heterogeneous photocatalysis: truths, half-truths, and misinterpretations. *Phys. Chem. Chem. Phys.* 2020; 22: 15723–15733. https://dx.doi.org/10.1039/d0cp02411b

[42] Stupar SL, Grgur BN, Radišić MM, Onjia AE, Ivanković ND, Tomašević AV, Mijin D. Oxidative degradation of Acid Blue 111 by electro-assisted Fenton process. *J. Water Process Eng. 2020;* 36: 101394. https://dx.doi.org/10.1016/j.jwpe.2020.101394

SAŽETAK

Primena impregnisanog biouglja proizvedenog iz sojinih ljuspica u procesu obezbojavanja boje

Aleksandra Kulić Mandić, Milena Bečelić-Tomin, Gordana Pucar Milidrag, Milena Rašeta i Đurđa Kerkez

Prirodno-matematički fakultet, Univerzitet u Novom Sadu, Departman za hemiju, biohemiju i zaštitu životne sredine, 21000 Novi Sad, Srbija

(Naučni rad)

U cilju moguće valorizacije, otpadne sojine ljuspice (engl. *waste soybean hulls*, OSLj) su ispitivane kao nosači jona Fe, u dve različite forme: sirovoj i karbonizovanoj (engl. *biocarbon*, BU). Impregnacija jonima Fe(III) je implementirana radi sinteze heterogenih Fenton katalizatora (Fe-OSLj i Fe-BU) za obezbojavanje vodenog rastvora *Reactive Blue 4* (RB4) boje. Karakterizacija materijala je pokazala porast specifične površine zbog dekompozicije konstituenata OSLj tokom karbonizacije (prilikom dobijanja BU) i termalne aktivacije (prilikom dobijanja Fe-OSLj i Fe-BU), gde su dobijeni katalizatori visoke mezoporoznosti sa hematitom kao aktivnom fazom za odvijanje Fentonove reakcije. Među pripremljenim materijalima, Fe-OSLj je pokazao značajnu sposobnost produkcije •OH radikala u kiseloj sredini. Dalje, optimizacija heterogenog Fenton procesa je izvedena primenom metodologije odzivnih površina (engl. *Respose Surface Methodology*, RSM), gde su redukovanim modelom izdvojeni sledeći uslovi reakcije: 3 mM H_2O_2, 100 mg Fe-OSLj, vreme reakcije od 180 min, pri konstantnim vrednostima pH = 3, koncentracije boje od 50 mg RB4 dm^{-3} i na sobnoj temperaturi. Postignuto je 88,7% i 66,8% obezbojavanja i mineralizacije RB4 boje, redom; Fe-OSLj je pokazao veliku stabilnost, a reakcioni intermedijeri formirani tokom oksidacionog procesa su imali nizak inhibitorni efekat na *Vibrio fischeri* bakterije.

Ključne reči: valorizacija; Fe(III)-impregnacija; metoda odzivnih površina; Reactive Blue 4; ponovna upotreba

YUCOMAT 2021: Sinergija nauke i društva i razvoj novih generacija istraživača svetske klase

IZVEŠTAJ SA KONFERENCIJE

Dragan Uskoković

Institut tehničkih nauka, Srpske akademija nauka i umetnosti, Beograd, Srbija

Uprkos svim neizvesnostima i ove godine je, od 30. avgusta do 3. septembra, u Herceg Novom održan 22. YUCOMAT, Konferencija Društva za istraživanje materijala Srbije. Na konferenciji je održano više plenarnih predavanja, ali i virtuelne "offline" prezentacije najeminentnijih naučnika iz celog sveta, predvođenih Stenlijem Vitingemom (Stanley Wittingham), jednim od tri dobitnika Nobelove nagrade za hemiju 2019. godine (za razvoj litijum-jonske baterije) i Andreom Gejmom (Andre Geim), jednim od dva dobitnka Nobelove nagrade za fiziku 2010. godine (za revolucionarne eksperimente sa grafenom). Pored toga, ne manje je bilo interesovanje za predavanja proslogodišnjeg i ovogodišnjeg dobitnika Velike nagrade Društva za trajan i izvanredan doprinos u oblasti novih materijala i nanotehnologija, Roberta Sinklera (Robert Sinclair) i Jurija Gogocija (Yury Gogotsi).

Keywords: life sciences; materials science; instrumentation and methods.

Available on-line at the Journal web address: http://www.ache.org.rs/HI/

PRIKAZ KNJIGA I DOGAĐAJA

UDK:005.745:006.82

Hem. Ind. **75 (5)** 321-327 (2021)

Organizacija nijedne YUCOMAT Konferencije do sada nije bila praćena sa tolikom neizvesnošću kao ovogodišnja. Neki od nas se sećaju treće YUCOMAT Konferencije, neposredno nakon NATO bombardovanja (od kraja marta pa do polovine juna 1999. godine), koja je održana sa samo jednim inostranim učesnikom: Đovanijem Batistonom (Giovanni Battiston) iz Nacionalnog saveta za istraživanja (CNR) iz Padove u Italiji. Neposredno po dolasku on je izjavio:"Ja sam obećao da ću doći i da ću održati predavanje na Vašoj Konferenciji, i došao sam", a nikome od nas nije bilo jasno kako je uspeo da dođe uprkos nepostojanju diplomatskih odnosa sa NATO zemljama. Prošle godine zbog pandemije COVID-19, po prvi put Konferencija nije održana, otkazana je neposredno uoči početka, kada se videlo da bi njeno održavanje bio ogroman rizik po zdravlje za sve učesnike.

Kada smo tokom juna i jula meseca ove 2021. godine došli do stote prijave, shvatili smo da su se stvorili uslovi za održavanje Konferencije, očekujući da će povoljna epidemiološka situacija i nadalje potrajati, i da ćemo svi zajedno u potpunosti poštovati sve epidemiološke mere i zaštititi i sve ljude iz okruženja i sebe. Zbog situacije koja se dosta pogoršala u celom svetu poslednjih dana pre početka Konferencije i ograničenosti putovanja, priličan broj predavača po pozivu je odlučilo da govore virtuelno, na daljinu, a mnogi su takođe odložili svoja predavanja za narednu godinu (23 YUCOMAT 2022, 29. avgust – 2. septembar, 2022). Petnaest plenarnih predavača je bilo u Programu, od kojih su pojedini poslali svoje prezentacije koje su bile predstavljene na Konferenciji u Virtuelnoj sesiiji i postavljene na internet strani Društva za istraživanje materijala, a troje plenarnih predavača je održalo predavanja uživo: Juri Gogoci (Yury Gogotsi), Ruslan Valijev (Ruslan Valiev) i Arben Merkoci (Arben Merkoci).

Od 100 autora koji su izložili svoje radove, usmeno i u obliku posterskih prezentacija, najviše ih je bilo iz Srbije, skoro 30 %, a zatim iz Češke, Slovenije, Poljske i Rusije (40 % ukupnog broja učesnika), a ostali su došli iz desetak drugih zemalja, sa ne više od 3-4 učesnika iz svake. Uz ove prezentacije održano je i dvadesetak usmenih predavanja i virtuelnih poster prezentacija. Pandemija je izmenila sastav učesnika, tako da smo ove godine imali sasvim drugačiju strukturu u odnosu na ranije godine, kada su dominirali učesnici iz SAD, EU, Koreje, Tajvana i sa dalekog Istoka. Najviše pažnje su privukla dva najavljen predavanja nobelovca, Stenlija Vitingema (Stanley Wittingham) o ogromnom značaju i perspektivama litijum jonskih baterija, koje je održano *online*, dok je predavanje drugog Nobelovca Andrea Gejma

Autor za korespodenciju: Dragan Uskoković, Predsednik Društva za istraživanje materijala Srbije, nstitut tehničkih nauka, Srpske akademija nauka i umetnosti, Beograd, Srbija

E-mail: uskok@itn.sanu.ac.rs

CC BY NC ND

(Andre Geim) o novinama kod ugljeničnih struktura, odloženo za iduću godinu, zbog naglo pogoršane epidemiološke situacije, neposredno uoči termina njegovog predavanja.

Pozdravna reč Predsednika Društva za istraživanje materijala Srbije
Welcoming speech by the President of the Serbian Materials Research Association

Nakon pet dobitnika Velike Nagrade našeg Društva za trajan i izvanredan doprinos nauci o materijalima, koji su bili iz zemalja bivše Jugoslavije, proslogodišnji dobitnik je profesor Robert Sinkler (Robert Sinclair), sa Stenford univerziteta, prvi nakon internacionalizacije nagrade i omogućavanja da je dobiju svi članovi Društva nezavisno od toga gde žive i stvaraju. Robert Sinkler je dao značajan doprinos proučavanju interakcija na atomskom nivou direktnim posmatranjem visokorezolucionim metodama elektronske mikroskopije. Kao dugogodišnji Predsednik Međunarodnog savetodavnog komiteta, prisustvovao je praktično svim YUCOMAT konferencijama poslednjih godina i u velikoj meri pomogao stvaranju jedne visoko intelektualne atmosfere. S obzirom da je prošlogodišnja Konferencija bila odložena, a ove godine je bio sprečen, Bob je poslao svoje predavanje koje smo ovo godine videli u Virtuelnoj sesiji, a diploma i plaketa će mu biti predata na sledećoj konferenciji 2022. godine.

Dobitnik ovogodišnje Nagrade za trajan i izvanredan doprinos nauci o materijalima je Profesor Juri Gogoci, direktor Instituta za Nanotehnologije Dreksel univerziteta iz Filadelfije, za ogroman doprinos u oblasti neoksidnih materijala sa specijalnim naglaskom na MAXene familiju dvodimenzionalnih metalnih karbida i karbonitrida i dugogodišnju uspešnu saradnju sa članovima Društva za istraživanje materijala i Međunarodnog instituta za nauku o sinterovanju. Juri je savršeno povezao svoje obrazovanje koje je stekao u bivšem Sovjetskom Savezu u Kijevu sa nekoliko posledoktorskih usavršavanja u Nemačkoj, Japanu i Norveškoj i definitivno se stacionirao u SAD i smatra se jednim od najvrednijih "naučnih transfera" sa istoka u SAD. Odluka za oba dobitnika nalazi se u Programu i knjizi izvoda radova (https://www.mrs-serbia.org.rs/index.php/book-of-abstracts-2021).

Jedna od vrlo značajnih aktivnosti našeg Društva od samog početka je nagrađivanje mladih istraživača učesnika Konferencije za najbolja ostvarenja. Od ove godine Društvo za istraživanje materijala Singapura, kao jedno od

najaktivnijih društava iz naše oblasti, koje je u sledećih pet godina sedište Kancelarije Unije društava za istraživanje materijala (IUMRS), pridružilo nam se u obezbeđivanju finansijskog dela ovih nagrada. Drugi dan Konferencije je bio posvećen takmičenju za najbolju oralnu i poster prezentaciju. Ujutro se u Svečanoj sali dvadesetak mladih ljudi takmičilo za najbolje usmeno izlaganje, a popodne drugih dvadeset, za najbolje poster izlaganje, od kojih je po pet izabrano za najbolje prezentovane radove (https://www.mrs-serbia.org.rs/index.php/yucomat-2021-awards). Njihova imena su saopštena poslednjeg dana na Zatvaranju Konferencije, a diploma i finansijski deo nagrade, biće im uručeni na Otvaranju 23. YUCOMAT konferencije, 29. avgusta 2022. godine.

Prof. Gogoci prima Nagradu od prof. Uskokovića / Prof. Gogotsi receives the Award from prof. Uskoković

Ovo je deseta YUCOMAT Konferencija koja je organizovana u hotelu Hunguest Sun Resort. U hotelu čije je ranije ime bilo Nuklear Centar, jer je pripadao Nuklearnoj komisiji bivše Jugoslavije, od 1969. godine organizovane su poznate Svetske Konferencije o sinterovanju, gde su kao i sada dolazili ugledni naučnici sa zapada i istoka, jer je u vreme "gvozdene zavese" naša zemlja bila jedino mesto gde su se mogli susresti. Više informacija o ovim Konferencijama je dostupno na web stranici www.iiss-sci.org.

Ovaj deo Herceg Novog zove se TOPLA i ovde su se obrazovali i stvarali neki od najumnijhi ljudi sa ovih prostora: naš poznati pesnik i državnik Vladika Petar II Petrović Njegoš je sticao osnovno obrazovanje u jednoj maloj kućici pored Crkve Svetog Đordja i Spasa, nedaleko od hotela, dok je neposredno sa druge strane jedini naš Nobelovac Ivo Andrić jedno vreme stanovao i stvarao. Naši domaćini iz hotela čuvaju i neguju uspomene na njih i to vreme, pre svega kroz naše Konferencije koje se ovde tradicionalno održavaju više od pedeset godina i koje oni tradicionalno podržavaju. Brojni su primeri njihovog krajnje dobronamernog odnosa i događaja za pamćenje u njihovoj organizaciji. To je svakako tradicionalni koktel koji se održavao prvog dana otvaranja konferencije tokom svih prethodnih godina, koji je ove godine, zbog trenutne epidemiološke situacije, izostao.

CC BY NC ND

Ovogodišnja YUCOMAT Konferencija je prošla u najboljem redu, uz poštovanje svih epidemioloških mera koje su propisane i nadamo se da će ostati u lepom sećanju svih učesnika, jer su se svi zdravi i zadovoljni vratili svojim domovima. Izuzetno je značajno što se Konferencija održala i pored svih teškoća, kako sa stanovišta njenog kontinuiteta, ali i zato što je zahvaljujući ovogodišnjem kvalitetnom Programu, veliki broj plenarnih predavača koji nije bio u mogućnosti da učestvuje u radu ovogodišnje Konferencije, potvrdio svoj dolazak na sledeći 23. YUCOMAT (29. avgust – 2. septembar 2022, Herceg Novi). Lista plenarnih predavača koji su potvrdili svoj dolazak nalazi se na internet strani: https://www.mrs-serbia.org.rs/index.php/confirmed-plenary-speakers-2022 .

YUCOMAT 2021: Designed to build bridges between science and society and develop a new generation of world-class researchers

CONFERENCE REPORT

Dragan Uskoković

Institute of Technical Sciences of Serbian Academy of Sciences and Arts, Belgrade, Serbia

Despite all the uncertainties and difficult epidemiological situation, the 22nd Annual YUCOMAT Conference of the Materials Research Society (MRS) Serbia was held in Herceg Novi, from August 30 to September 3, which included Plenary lectures and Virtual offline presentations of the most eminent scientists from around the world, led by M. Stanley Whittingham winner of the 2019 Nobel Prize in Chemistry for lithium-ion batteries and Andre K. Geim, winner of the Nobel Prize for 2010 in Physics for graphene. Not smaller interest has provoked the lectures of last year's and this year's winners of the MRS Award for Lasting and Outstanding Contribution in the field of new materials and nanotechnologies, Robert Sinclair and Yury Gogotsi.

Keywords: life sciences; materials science; instrumentation and methods.

Available on-line at the Journal web address: http://www.ache.org.rs/HI/

BOOK AND EVENT REVIEW

UDC: 005.745:006.82

Hem. Ind. **75 (5)** 000-000 (2021)

Not a single prior YUCOMAT Conference has been organized with as much uncertainties as this one. Some remember the Third YUCOMAT Conference held right after the NATO bombing of Serbia and Montenegro, which lasted from the end of March 1999 until mid-June that same year. That Conference was held with a single foreign participant – Giovanni Battiston, National Research Council (CNR), Padua, Italy, who said back then, "I promised that I would come and now I am here", and it was not clear to any of us how he managed to come despite the lack of diplomatic relations with all NATO countries. Last year was the first one to have a YUCOMAT Conference cancelled, not long before the scheduled beginning, at the point when it was clear that the risk for the participants would be too large.

As we reached the 100th abstract submission during June and July this year, we decided that the Conference should be organized, hoping that the positive epidemiological situation would continue throughout the summer and that the measures will be respected. A number of plenary lecturers had to cancel their lectures and postpone them for the next year (YUCOMAT, August 29 – September 2, 2022), considering the travel limitations in many countries.

There were still about 15 plenary lecturers in the Program, some of whom sent their presentations, presented in the Virtual Offline Session on the MRS webpage, and 3 Invited Plenary Speakers have presented their lectures in person: Yury Gogotsi, Ruslan Valiev and Arben Merkoci. Out of 100 authors who presented their research orally and as poster presentations, the majority were from Serbia, around 30 %, followed by participants from Poland, Czech Republic, Slovenia and Russia, accounting for about 40 % in total, whereas from other countries there were up to 3-4 participants. In addition to these presentations, twenty-two oral and poster virtual lectures were also shown. The coronavirus has done its fair share and as a result we had a very different structure of participants compared to earlier years, when they were predominantly from USA, EU, Korea, Taiwan and the Far East. The lectures of two Nobel laureates attracted the most attention. The talk of Stanley Wittingham on the great importance and perspectives of lithium-ion batteries was held as a Virtual Offline Presentation, while the lecture of the other Nobel laureate Andre Geim on innovations in carbon structures was postponed to the next year due to the rapidly worsening epidemiological situation, immediately before the date of his lecture.

After five winners of the Big Award of our Society for the lasting and outstanding contribution to materials science who originated from the region of former Yugoslavia, the last year's winner was Robert Sinclair, Charles M. Piggot Professor at the School of Engineering, Stanford University and the first to win this award after its internationalization and opening to all our members. Robert Sinclair gave a significant contribution to the study of interactions at the atomic

Corresponding author: Dragan Uskoković, President of MRS Serbia, Institute of Technical Sciences of SASA, Belgrade
E-mail: uskok@itn.sanu.ac.rs

CC BY NC ND

level in materials by direct observation by high-resolution electron microscopy methods. As a long-term President of the International Advisory Board and a participant at all recent YUCOMAT Conferences, Robert Sinclair gave a significant contribution to our Society and greatly helped to create a highly intellectual atmosphere. Since the last year's Conference was not held and Bob could not attend this year's conference, he sent his talk, which was presented in the Virtual Offline Session. The Award certificate and the medal will be given to him next year.

Posterska sesija / Poster session

This year's winner of the Award is Prof. Yury Gogotsi**,** director of the Drexel Nanotechnology Institute, for his contribution to the field of nonoxide materials with the special emphasis on MAXene family of 2D metal carbides and carbonitrides and a long-term successful cooperation with our country through MRS-Serbia and the International Institute for the Science of Sintering. Yury perfectly connected his education acquired in the former Soviet Union in Kiev,

with several postdoctoral research studies in Germany, Japan and Norway, and he definitely stationed in the USA. It is considered one of the most valuable "scientific transfers" from the East to the United States. The decision for both winners can be found in the Program and the Book of Abstracts (https://www.mrs-serbia.org.rs/index.php/book-of-abstracts-2021).

One of the very important activities of our Society from the start is rewarding the best young researchers at the Conference. As of this year, the MRS – Singapore, as one of the most active societies in this field in the world, which will be also the headquarters of the International Union of MRS (IUMRS) in the next 5 years, has joined us in the financial segment of this award. Second day of the Conference was dedicated to this activity and 20 young scientists competed for the best oral presentation, whereas in the afternoon 20 participants competed for the best poster presentation. In both cases, 5 best presenters were selected and their names were announced at the Conference Closing, whereas the certificates and the financial rewards will be provided at the opening of the next YUCOMAT Conference, August 29, 2022 (https://www.mrs-serbia.org.rs/index.php/yucomat-2021-awards).

This is the tenth YUCOMAT Conference to be held in the Hunguest Sun Resort Hotel. At this very same location, which used to be the Nuclear Center belonging to the Nuclear Commission of former Yugoslavia, starting from 1969, the World Round Table Conferences of Sintering were held, in which, just like today, world-renowned scientists from both West and East used to congregate. In the Iron Curtain era, in fact, it was the only place where such a meeting was possible, www.iiss-sci.org. This part of Herceg-Novi is called Topla in which some of the most renowned intellectuals from this region have stayed. Our famous poet and statesman, Petar II Petrović Njegoš, for example, was educated in a little house near the Church of Saint George, not far from the hotel, whereas directly on the opposite side, the Nobel Laureate in literature, Ivo Andric, used to live and work. Our hosts at the Hunguest Hotel maintain the memory of those great figures and those times by helping us to organize conferences, which have been traditionally held here for more than fifty years and which are traditionally supported. There are numerous examples of their extreme hospitality and organization of memorable events, one of them certainly being the cocktail party traditionally held on the first conference day but this year missing, due to the current epidemiological situation.

Dobitnici nagrada za najbolja usmena i posterske saopštenja / Winners of the award for the best oral and poster presentations

This year's YUCOMAT Conference went well, respecting all appropriate epidemiological measures and we hope that it will be worth remembering because all participants stayed healthy and safely returned to their homes.

Successful completion of the Conference in significant both from the point of view of maintaining the Conference continuity, and for confirmation of a considerable number of plenary speakers, who were not able to participate in YUCOMAT this year, to join the next YUCOMAT 2022 (August 29 - September 2, 2022, Herceg Novi). The first list of confirmed plenary speakers can be found at the MRS website: https://www.mrs-serbia.org.rs/index.php/confirmed-plenary-speakers-2022.

CC BY NC ND